# Photoelectron Spectroscopy of Undercoordinated Atoms on Various Morphologic Surfaces


**Nie Yanguang**

**School of Electrical and Electronic Engineering**

**2012**

# ACKNOWLEDGEMENTS

This thesis involves extensive collaborations and a lot of helps from so many respectable people. It gives me an opportunity to show my gratitude to all people who had done contributions to this thesis.

First and foremost, I would like to express my deep gratitude to my research supervisor, Dr. Sun ChangQing. He gave me an opportunity to continue my high degree pursuing in such interesting research field. With his encouragement, guidance and invaluable suggestion, I immersed into the project gradually. His understanding coupling with his research and teaching experience have immensely contributed to my enlargement in knowledge and ability in science. This thesis could not be completed without his guidance. I am very grateful to his extreme patience to my PhD research which is the strongest encouragement for me to finish the study in NTU. The research experience under Prof.Sun will go with my next steps and absolutely gives me the direction of research life.

I would also like to express my deep gratitude to my co-supervisor Dr. Pan Jisheng. In my research, Dr.Pan gives me a strong support not only the experimental facilities, but also the project discussion and the assistance in solving difficulties faced in experiments. In addition, the kind help in normal life from Dr.Pan enables me to go into my project quickly.

I also want to thank to Dr. Chai Jianwei, Dr. Zhangzheng, Dr. Tao Junguang for XPS training and TEM analysis. Special thanks also to Dr Li Xiaocheng for providing important instruction in sample preparation.

Furthermore, I want to express my warmest gratitude to my colleagues: Dr. Wang Yan always discusses with me for some experimental problems. Thanks to Dr. Zhangxi and Dr Ma Shouzhi for assistance in my research.

A special thank to my family. My parents give so many advices from their life experience. My wife gives me giant encouragements in life and continuous love. Their support is the most critical factor to complete my PhD study and this thesis.

# SUMMARY

It is the intent of this work to investigate the behavior of the local bonds and electrons associated with under-coordinated atoms at surface, terrace edge, adatoms, vacancies and interface, and their response to the environment and applied stimuli. Although the chemistry and physics of materials at these specific sites have been intensively investigated for more than half a century, the laws governing the performance of the under-coordinated atoms remain as yet unestablished.

The recently developed bond order length strength (BOLS) correlation proposed that the interaction between the under-coordinated atoms at the site of single crystal surface, the curved surface of nanoparticles, terrace edges, adatoms and vacancies dominate the abnormal performance of those substances. The bond length between under-coordinated atoms contracts spontaneously and bond energy is enhanced consequently. The bond modification causes the localization and densification of charge and energy and hence the impact on the Hamiltonian.

With the aid of the BOLS correlation and the tight binding (TB) approximation, this thesis developed a new method named atomistic photoelectron spectroscopy distillation (APSD), which has enabled us to solve the most significant and outstanding challenge by zooming in the bonds and electrons within the atomic patches surrounding the under- and hetero-coordinated atoms. With help of new method APSD, the thesis extended the BOLS correlation on the description of Polarization state occurring in systems with under-coordinated atoms. We have conducted X-ray photoelectron spectroscopy measurements on Ni, Cu and Pt metal nanoparticles deposited on different substrates and the atomic vacancies on graphite

surface. We have also re-analyzed the available spectral data systematically from published literatures with the perspective of bond and non-bond formation, dissociation relaxation and vibration and the associated energetic and dynamics of electrons in the repopulation, localization, densification and polarization.

Theoretical analysis has enabled the determination of the length and strength of the representative bond and the energy levels of an isolated atom and the bulk shift of the binding energy(BE), the local binding energy density, atomic cohesive energy within the atomic patches with the following new understanding:

(i) The classification of the Pt adatoms and the Cu/Pd interface serving as excellent acceptor-type catalysts while the Rh adatoms as donor-type by means of re-analyzing the data published in previous literatures;

(ii) The demonstration of crystal-orientation and atomic-layer-resolved BE shift of *fcc*(Pd, Rh, Pt), *bcc*(W), *hcp*(Be, Ru, Re) surfaces and carbon allotropes(graphene, graphite, diamond) based on well measured data given by other researchers;

(iii) The determination of the edge-discriminative generation of graphitic Dirac-Fermi polarons from graphite surface with and without vacancies; and the size dependent BE shift of Ni, Pt, Cu nanoparticles.

Experimental and theoretical analysis confirm the perturbation to the Hamiltonian arising from the skin-depth local strain and potential well quantum trapping which are induced by the shorter and stronger bonds between under-coordinated atoms, and associated charge and energy polarization which are induced by the localized quantum entrapment.

*ACKNOWLEDGEMENTS* ..... *I*

*SUMMARY* ..... *III*

*LIST OF FIGURES* ..... *VIII*

*LIST OF TABLES* ..... *XIII*

*NOMENCLATURES* ..... *XIV*

*Chapter 1 Introduction* ..... *1*

**1.1 Overview** ..... **1**

**1.3 Objectives and Scopes** ..... **6**

**1.4 Major Achievements** ..... **7**

**1.5 Organization** ..... **8**

*Chapter 2 Principles* ..... *11*

**2.1 Introduction** ..... **11**

**2.2 Band Dispersion and BE Shift** ..... **12**

**2.3 BOLS: Coordination Number Imperfection** ..... **17**

**2.4 BOLS in Nanosolids** ..... **22**

**2.5 BOLS: Polarization** ..... **28**

**2.6 Introduction of X-Ray Photoelectron Spectroscopy** ..... **30**

**2.7 Conclusion** ..... **32**

*Chapter 3 Atomic Layer and Orientation Resolved Surface BE Shift* ..... *33*

**3.1 Introduction** ..... **33**

**3.2 *Fcc* structured Pd and Rh surfaces** ..... **34**

**3.3 *Bcc* structured W surfaces** ..... **45**

**3.4 Hcp structured Ru, Be and Re surfaces** ..... **50**

3.4.1 Be(0001), (11$\mathbf{2}$0), and (10$\mathbf{1}$0) surfaces ..... 50

3.4.2 Ru(0001) and (10$\mathbf{1}$0) Surfaces ..... 59

**3.5 Conclusion** ..... **61**

*Chapter 4 BE Evolution on Terrace Edge, Adatoms and Vacancies* ..... *65*

**4.1 Introduction** ..... **65**

**4.2 Terrace Edge on Re Surface** ..... **69**

4.2.1 Introduction ..... 69
4.2.2 Results and Discussions ..... 71
4.2.3 Conclusion ..... 78
**4.3 Terrace Edge on W Surface ..... 79**
4.3.1 Introduction ..... 79
4.3.2 Results and Discussions ..... 80
4.3.3 Conclusion ..... 82
**4.4 Pt and Rh Adatoms ..... 85**
4.4.1 Introduction ..... 85
4.4.2 Results and Discussion ..... 85
4.4.3 Conclusion ..... 91
**4.5 Vacancies on Graphite ..... 94**
4.5.1 Introduction ..... 94
4.5.2 Results and Discussions ..... 95
4.5.3 Conclusion ..... 97
***Chapter 5 Size Dependent BE Shift of Metal Nanoparticles ..... 101***
**5.1 Introduction ..... 101**
**5.2 Ni Nanoparticles. ..... 102**
5.2.1 Ni Nanoparticles on $SiO_2$/Si Substrate ..... 103
5.2.2 Ni Nanoparticles on $SrTiO_3$(100) Substrate ..... 112
**5.3 Pt Nanoparticles on $SiO_2$/Si Substrate ..... 125**
5.3.1 Substrate Preparation ..... 125
5.3.2 Results and Discussions ..... 127
5.3.3 Conclusion ..... 131
**5.4 Cu Nanoparticles on STO Substrates ..... 131**
5.4.1 Substrate Preparation ..... 131
5.4.2 Results and Discussions ..... 132
5.4.3 Conclusion ..... 137
**5.5 Conclusion ..... 137**
***Chapter 6 Impurities and Interfaces: Catalyst and Diffusion Barrier ..... 139***
**6.1 Introduction ..... 139**
**6.2 The Principle of Interface Quantum Entrapment ..... 140**
**6.3 Results and Discussions ..... 142**

**6.4 Conclusion** ..... **145**

***Chapter 7 Conclusions and Recommendation*** ..... ***148***

**7.1 Achievement** ..... **148**

**7.2 Limitations** ..... **150**

**7.3 Recommendations** ..... **151**

7.3.1 The Combination of STM and XPS Measurement. ..... 151

7.3.2 Performance of Under-coordinated System ..... 151

***List of Publications*** ..... ***152***

***References*** ..... ***154***

# LIST OF FIGURES

Figure 1 Evolution of a single energy level into the band structure when particle grows from a single atom to a bulk solid that contains $N_j$ atoms. Indicated is the work function W, band gap $E_g$, and bandwidth. The number of allowed sublevels in a certain band equals the number of atoms of the solid.…… ……13

Figure 2 Illustration of the BOLS correlation. Solid line in (a) corresponds to the bond contraction coefficient with literature data from Goldschmidt (circles),[34] Feibelman (square),[36] and Comashchi (down triangle).[44] The atomic cohesive energy with different *m* is also shown in (a). (b) Atomic CN imperfection modified pairing potential energy. …… ……20

Figure 3 Schematic illustration of undercoordination induced surface modification on the potential well. The potential well at undercoordinated site is perturbed in a ratio of $\delta_j$in which represents the localization and densification of potential well.……23

Figure 4 Electron polarization(P) induced by the Local quantum trapping (T) and densification of charge and energy. ……..…….29

Figure 5 The schematic description for the photoelectron emission process. ……31

Figure 6 Illustration of the XPS spectrum. $E_v(1)$ is the energy level of an isolated atom, which is the reference for the shifts of other components that follows these constraints: (1) there should be components representing the B, $S_2$, $S_1$ and $S_{defect}$; (2) the energy shift should be positive and the low-z components shift further; (3) the energy shift of each component is proportional to the magnitude of bond energy, which follows this relation: $\Delta E_v(\Delta_H): \Delta E_v(\infty) = E_i: E_b = c_i^{-m}$……...……...38

Figure 7 Decompositions of Pd $3d_{5/2}$ core level spectra for (a) (111), (b) (100) and (c) (110) surfaces with three decomposition Gaussian components $S_1$, $S_2$ and *B* with parameters given in Table 1.. The XPS spectra were collected with incident beam energy of 380 eV at normal emission……..43

Figure 8 Decompositions of Rh $3d_{5/2}$ core level spectra[59] for (a) (111), (b)(100), and (c)(110) with decomposition parameters given in Table 1. The XPS spectra were collected with incident beam energy of 380 eV at normal emission.……44

Figure 9 Decomposition of the XPS $4f_{7/2}$ spectra of (a) W(100),[71] (b) (110),[68] and (c) (111)[67] surfaces using the B, $S_2$ and $S_1$ components with the derived 4f level of an isolated W atom as $E_{4f}(0)$ = 28.910 ± 0.006 eV and its shift upon bulk formation, $\Delta E_{4f}(12)$ = 2.173 eV, both of which are intrinsic constants changing with neither the experimental conditions nor the crystal orientations……..49

Figure 10 The decomposed XPS spectra for the Be(0001), $(10\bar{2}0)$, and $(11\bar{2}0)$ surfaces The 1s core level of 106.416 ±0.004 eV and the B component at 111.11 eV should be identical for all the surfaces of the same material.……57

Figure 11 Comparison of the BOLS prediction with the derived CN(layer)-and orientation- resolved (a) bond strain and the relative change of atomic cohesive energy ($E_C$); (b) potential trap depth and, (c) the relative energy density.……58

Figure 12 The decomposed XPS spectra for (a) the Ru(0001)[89] and (b) Ru($10\bar{1}0$)[90-92] surfaces with derived information as summarized in Table 4. ……...……...63

Figure 13 Comparison of the BOLS prediction with the derived CN (layer and orientation) - resolved (a) BE; (b) the relative change of atomic cohesive energy ($E_C$); (c) the relative energy density.…….64

Figure 14 Illustration of the origin for the adatom- and surface-induced core level shift. (a) Atomic arrangement at a surface with irregularly grown adatoms, $A_1$ and $A_2$ with effective CN smaller than 4. $S_1$, $S_2$ and B represent the outmost, the second and the bulk components. P represents the polarization state. (b)**:**In addition to the main peaks of B, $S_2$, $S_1$, there should be A and P components representing the trapped and the polarized states of the under-coordinated adatoms. The energy shift should be positive and the lower-z component shifts further. However, the P states should move oppositely with respect to the A states.……..69

Figure 15 Schematic illustrations of the atomic configurations of the clean Re(0001) and Re($12\bar{3}1$) surface. The right panel shows the atomic kink edge of the ($12\bar{3}1$) with high fraction of undercoordinated atoms…..…….70

Figure 16 The decomposed XPS Re $4f_{5/2}$ spectra collected from the (a) Re(0001)[109] and the Re($12\bar{3}1$)[54] surfaces with (b) $0^0$ (along the surface normal) and (c) $75^0$ emission angles. The constant bulk component locates at 42.645 eV. The intensities of the surface ($S_1$ and $S_2$) components increase with the emission angle rendering that of the bulk component.…….……73

Figure 17 The APDS of (a) the entire Re 4f band of the Re($12\bar{3}1$) surface.[54] The similar structure of valleys and peaks confirm the consistency between $4f_{7/2}$ and $4f_{5/2}$ bands. The small feature at the upper edge of the $4f_{7/2}$ arises from the purified $5p_{3/2}$. (b) The APDS of the $4f_{5/2}$ band with the valley centered at 42.645 eV includes contribution from the B and the inner $S_4$ and $S_3$ sublayers; the extra gains at the bottom edge corresponds to the under-coordination induced local bond strain and quantum entrapment in the surface skin dominated by the outermost two atomic layers.……75

Figure 18 The decomposed XPS Re $4f_{7/2}$ spectra collected from the Re($12\bar{3}1$) surfaces (a) before and (b) after oxygen adsorption. (c) The APDS for the oxygen adsorbed Re($12\bar{3}1$)(red line) in comparison to the APDS for Re $4f_{7/2}$ kink states (black line). Extra gain is resolved due to oxygen chemisorption and the bulk component shifts further to deeper energies…..……....77

Figure 19 The surface atomic structures of the (100) vicinal (540) and (320) surfaces with edge atoms density. The edge density of (320) is 0.28 monolayer (ML) and the (540) is 0.16 ML.……79

Figure 20 From the normalized the (110), (540), and (320) XPS $4f_{7/2}$ spectra[68] (a) one can hardly discriminate the contribution of the edge atoms from those of the un-edged (110) surface; but (b) the PRS, or subtraction of the un-edged from the edged W(540) and (320) surfaces, can resolve the edge

states unambiguously with the P and P+T extra states and the B and the additional valley at the bottom edge. The resultant PRS almost satisfies the criterion of spectra area conservation.……84

Figure 21 The PRS for Rh adatoms with the inset of Pt adatoms[114] for comparison with Figure 20b. The spectral similarity of the Rh adatoms and W edge atoms suggests that W edge may perform the same to Rh adatoms as a donor-type catalyst..…… ..…….85

Figure 22 Comparison of the subtracted spectra for surfaces with varied coverage of adatoms by the spectra of clean surfaces of (a) Pt $4f_{7/2}$[108] and (b) Rh $3d_{5/2}$.[59] Indicated numbers are the effective atomic CNs for bulk (12), surface layers (4, 6), and adatoms (< 4). The spectral differences in (c) and (d) show clearly the presence of quantum trapping effect in both cases and (d) the dominance polarization effect in Rh, which differs Pt from Rh adatoms in catalytic reactions.…….....87

Figure 23 Decomposed XPS spectra of the (a) Pt(111) and (b) Rh(100) clean surfaces with five components each representing the polarized P, bulk B, surfaces $S_1$ and $S_2$, and the adatom A states from lower (larger absolute value) to higher BE. The decomposition parameters are listed in Table 6……..91

Figure 24 The raw XPS spectra collected from (a) defect-free HOPG surface at different emission angles and (b) the defect surface at 50° of different $Ar^+$ spray doses. (c) The purified XPS shows only the trapped ($T_S$) surface states evolving from z ~ 4 to z ~3.2 with emission angle increasing and (d) both the trapped ($T_D$) and polarized (P) states to the defects.…….…….99

Figure 25 Comparison of the purified XPS C 1s spectrum collected at 75° from the surface with ($9\times10^{14}$ $cm^{-2}$ dosed $Ar^+$ spray) and without defects. The valleys centered at 284.2and 284.4 eV correspond**,** respectively, to the removed obvious graphite bulk and surface-bulk information and the extra components are the energy states due to the surface skin, $T_S$(z ~ 3.1), within the outermost two atomic layers and sites surrounding vacancy defects, $T_D$(z ~ 2.2). G denotes the bulk graphite (z = 5.335). The P component at the upper edge arises from the screening and splitting of the crystal potential by the DFPs that originate from the polarization of the entrapped ($T_D$ in the bottom of the core band) core electrons.……..100

Figure 26 Si 2p core level of $SiO_2$/Si substrate.…….……...…….104

Figure 27 Schematic of Ni nanoparticles on oxide substrate in thermodynamic equilibrium…….....105

Figure 28 TEM observation of Ni nanoparticles deposited on $SiO_2$ substrate for deposition time of (a) 2 min and (c) 30 min. (b) and (d) are the corresponding nanoparticles size histogram. The circled boundary of nanoparticle in (a) is for viewing convenience..……108

Figure 29 (a) XPS Ni $2p_{3/2}$ profiles at different deposition time (b) peak fitting of $2p_{3/2}$ core level, the Shirley background subtraction is adopted..……..109

Figure 30 Consistency between the BOLS prediction (solid line) and the measured BE of Ni $2p_{3/2}$ (scattered data) of Ni nanoparticles. Inset is the least mean-root-square fitting of the BE of Ni $2p_{3/2}$ to the inverse of size: $E_v(K) = 853.26\pm0.02 + (1.71\pm0.07)/K$..……..……111

Figure 31 (a)the FWHM variation with deposition times ranging from 20 sec to 60 minutes.(b) The residual spectrum shows the effect of quantum trapping (T).……113

Figure 32 The XPS of Sr 3d BE of clean STO (100) surface.…… ……..……114

Figure 33 XPS Ni $2p_{3/2}$ (a) and (b) Ni 3p (b) spectra showing the BE shift as a function of Ni coverage deposited onto STO(100) surface. The inserts are the corresponding peak fitting. 'S' represents the satellite peak.…….117

Figure 34 BOLS algorithm reproduction of the relative BE shift of both the $2p_{3/2}$ and the $3p_{3/2}$ derives the values of: $E_{2p_{3/2}}(1)$ = 850.51 eV, $E_{2p_{3/2}}(\infty)$ =2.70 eV; $E_{3p_{3/2}}(1)$ = 62.16 eV, and $E_{3p_{3/2}}(\infty)$ =3.91 eV.……..119

Figure 35 The Auger kinetic energy, $E_K(L_3M_{23}M_{23})$ (denoted as arrowed) as function of Ni coverage deposited onto STO(100) surface…….……124

Figure 36 The Ni $3p_{3/2}$ BE shift in comparison to the "final state" effect of relaxation energy and the "initial state" effect.……...……125

Figure 37 The Si 2p peak of clean $SiO_2$/Si surface. Three components including SiO, Si and $SiO_2$ are observed.……126

Figure 38 TEM measurement of Pt deposited on $SiO_2$/Si substrate at different deposition time(a)0.5 hour, (b)1hour, (c)1.5 hour, (d)2 hour, (e)3 hour, (f)3.5 hour.……..…128

Figure 39 (a) The Pt 4f peak XPS measurement at different deposition time from 0.5hour to 3.5 hour. (b)The peak fitting of Pt 4f core level.……..……129

Figure 40 The comparison between the prediction of BOLS on the size dependent BE shift of $Pt4f_{7/2}$ core level and the experimental data. $\tau = 2, 3$ represent the 2D and 3D growth mode of Pt nanoparticles on $SiO_2$/Si substrates.……130

Fgure 41 The comparison of Sr 3d core level from STO(100) surface and (111) surface…….... 132

Figure 42 The BE evolution of Cu 2p3/2 peak on (a) STO(100), (b) STO(111) surfaces with different deposition time presented in figure……134

Figure 43 The valence band evolution of Cu nanoparticles on (a) STO(100), (b) STO(111) surfaces. The insert is the valence band of clean STO(100) and (111) surface.……..……135

Figure 44 The BOLS prediction on the Cu nanoparticles deposited on STO(100) and (111) surface.……..……136

Figure 45 Schematic illustration of (a) the QT model and (b) the QT-induced core-level shift, $\Delta E_v(I)$ and $\Delta E_v$ (B) from the energy level of an isolated atom, $E_v(1)$, $V_{atom}(r)$ is the intraatomic potential. $V_{cry}(r, B)$ and $V_{cry}(r, I)$ are interatomic potentials in the bulk and the interface region, respectively. $\gamma$ is

the enhance parameter. $\gamma$ >1 represents the compact and $\gamma$ <1 represents the dissociated interface. Annealing will increases the $\Delta E_v(I)$ intensity, rendering that of the $\Delta E_v(B)$, upon alloy formation…141

Figure 46 Thermally-driven spectral evolution of (a) Cu $2p_{3/2}$ and (b) Pd $3d_{5/2}$ BE upon annealing at 540 K and 940 K and their decompositions.……144

# LIST OF TABLES

Table 1 Decomposition parameters of the XPS $3d_{5/2}$ core level shift of Rh and Pd surfaces after the Tougaard background is subtracted. The three decomposition Gaussian components, denoted as $S_1$, $S_2$ and $B$, satisfy the BOLS expectation. ……..…42

Table 2 BOLS elucidated information regarding the atomic-layer ($S_1$, $S_2$) and crystal-orientation resolved effective CN ($z$), local strain ($C_z$-1), the relative BE density ($C_z^{-4}$) and atomic cohesive energy ($z_{ib}C_z^{-1}$) from the measured XPS W 4f SCLS. The $z_{ib} = z_i/z_b$ is the relative coordination number……..48

Table 3 Atomic-layer and crystal-orientation resolved effective CN(z), local strain (c(z)-1), relative BE density ($c(z)^{-4}$), and the relative atomic cohesive energy ($z_{ib}/c(z)$ with $z_{ib} = z/12$) determined from the measured XPS profiles of Be(0001), $(10\bar{1}0)$, and $(11\bar{2}0)$ surfaces under the established approach and the criteria……..…..56

Table 4 Summary of the BOLS elucidated information regarding the atomic-layer and crystal-orientation resolved effective CN ($z_i$), local strain ($c_i$-1), the ratio of BE density ($c_i^{-4}$) and atomic cohesive energy ($z_{ib}c_i^{-1}$) derived from the measured XPS profiles of Ru(0001)[89] and Ru$(10\bar{1}0)$[90-92]

62

Table 5 Crystal orientation and atomic layer resolved Re $4f_{5/2}$ shift with derived information of the effective CNs, local strain ($C_z$-1), relative BE density ($C_z^{-4}$), and the relative atomic cohesive energy ($z_{ib}/C_z$ with $z_{ib} = z/12$) of the Re(0001) and $(12\bar{3}1)$ surfaces……...…74

Table 6 Summary of decomposition parameters (BE-BE; W-width; I-intensity) for the Pt and Rh spectra and the BOLS derived effective CN(z), local strain ($c_z - 1$), the ratio of BE density ($c_z^{-4}$) and the ratio of atomic cohesive energy ($z/z_bc_i^{-1}$) for each surface and adatom component. $z_b = 12$…….….93

Table 7 The peak position for energy bands including Auger peak after peak fitting performed. The position with the highest intensity is recorded as VB peak position…….……124

Table 8 The size dispersion of the Pt nanoparticles deposited on $SiO_2$/Si substrate at different deposition time and corresponded BE of $Pt4f_{7/2}$……136

Table 9 The BE shift of $2p_{3/2}$ for Cu on STO(100) and (111) substrates with different film thickness.136

Table 10 XPS measured intensity (I) evolution of Pd $3d_{5/2}$ and Cu $2p_{3/2}$ BE (BE) at the Cu(2nm)-Pd(10 nm) interface as a function of annealing temperature, T……...……147

Table 11 Summary of the relative depths γ and the interface energy shift ΔE(I) for the Pd $3d_{5/2}$ and Cu $2p_{3/2}$ BEs……..147

# NOMENCLATURES

| | |
|---|---|
| AES | Auger Electron Spectroscopy |
| AFM | Atomic Force Microscopy |
| AP | Auger Parameter |
| APSD | Atomistic Photoelectron Spectroscopy Distillation |
| BCC | Body Centered Cubic |
| BOLS | Bond Order Length Strength |
| BE | Binding Energy |
| CN | Coordination Number |
| DFT | Density Functional Theory |
| FCC | Face Centered Cubic |
| HOPG | Highly Oriented Pyrolytic Graphite |
| HCP | Hexagonal Close-Packed |
| LEED | Low Energy Electron Diffraction |
| 1D | One Dimension |
| ML | Monolayer |
| nm | nanometer |
| STO | $SrTiO_3$ |
| STM/S | Scanning Tunneling Microscopy/Spectroscopy |
| TEM | Transmission Electron Microscopy |
| UHV | Ultra High Vacuum |
| XPS | X-ray Photoelectron Spectroscopy |
| XRD | X-ray Diffraction |
| VB | Valence Band |
| DFPs | Dirac-Fermi Polarons |

# Chapter 1 Introduction

## 1.1 Overview

The under-coordinated atoms at the sites of surface, terrace edges, adatoms, atomic vacancies and nanosolids[1] govern the unusual properties of a materials in catalytic reactivity,[2, 3] crystal growth,[4] adsorption,[5] decomposition,[6] doping,[7] interface formation,[8, 9] wetability,[10] thermal stability,[11] etc. Although the chemistry and physics of materials associated with atomic undercoordination have been extensively investigated for decades, the laws governing the performance of such local bonds and electrons remain unestablished.[12-14] Collection and purification of such local, atomistic zone selective, and quantitative information having been increasingly demanded but it remains as yet the "dead corner" of the community. Thus, the elucidation of the electronic structure and the electronic binding energy (BE) of such under-coordinated systems is of great importance.

As a type of under-coordinated atoms, surface atoms show strong abnormality in contrast to that in bulk interior. As a consequence, surface BE shift has been observed in many materials using X-ray photoelectron spectroscopy (XPS) measurements. In principle, the well-known chemical shift due to charge transportation in a reaction and relaxed atomic layers induced by under-coordinated surface atoms at a surface region can split the core level of a specimen into a few

components. However, the assignment for the components induced by surface relaxation is quite confusing, due to the lack of guidelines for determining which peak arises from the surface and which one is from the bulk. The resultant peak is often located in between the components and the exact position of the resultant peak varies with experimental conditions, which is perhaps why the documented values for the core level energy of a specimen vary from source to source and hard to gain clear band map.

When a solid reduces its size down to nanometer scale to be as a nanosolid with much more under-coordinated atoms, the entire core level features both the main peak and the satellites move simultaneously towards higher BE and the amounts of shift depend on both the original core level position and the particle shape and size. This has been confirmed with XPS on the size-dependence of the main core level peaks in many nanoparticles. For example, the BE of Au $4f_{7/2}$ peak shifts from 84.9 eV to 84.0 eV when the diameter of Au nanoparticles synthesized by micellar method[15] increases from 0.8 nm to 2.9 nm. The Au nanoparticles deposited on substrate of $SiO_2$/Si, alumina and highly oriented pyrolytic Graphite (HOPG), exhibit similar BE scaling effect. For silicon nanoparticles, the BE of Si 2p shifts around +0.9 eV as the diameter decreases from 2.1 to 1.4 nm.[16] However, Fundamental understanding in the mechanism according to the size dependent BE shift in nanosolids has been still lagging far behind the experimental observations.

Similar BE shift has also been observed in many other under-coordinated

systems including terrace edge, adatoms, vacancies and interface of alloy.[17-24] However, the origin of the BE shift which corresponds to the nature of bonds and electrons annexed under-coordinated atoms has been under debates with following possible mechanisms:

(i) Thermo-chemical model: according to surface of Tb(0001)[25] single crystal, the 4f BE shift is defined as the difference in cohesive energy that is needed to remove a core electron either from a surface atom or bulk atom. It is calculated by Born-Haber cycle consisting of the evaporation of a metal atom with valence Z, the excitation of a 4f electron to unoccupied 5d orbital in a free atom to the condensation of the excited free atom, the dissolution of this condensed phase with zero concentration in metal Z. Summing up the different energy involved, the heat of formation of a Z+1 impurity atom in Z metal is obtained as

$$E_B = E_{fd} + E_{coh}^{z} - E_{coh}^{z+1} + E_{imp} \tag{1}$$

where $E_{fd}$ denotes the *f-d* excitation energy, $E_{coh}^{z}$ and $E_{coh}^{z+1}$ are the cohesive energies for valence states Z and Z+1, respectively. $E_{imp}$ is the heat of solution of a dilute Z+1 impurity in the matrix of the Z metal. Finally, combined with the relation between coordination number N and BE shift, surface BE shift can be presented as:

$$\delta_N = E_B^N - E_B^{Bulk} = \left(1 - \sqrt{\frac{N}{12}}\right)(E_{coh}^Z - E_{coh}^{Z+1} + E_{imp}) \quad (2)$$

This model has been generally accepted and a negative or mixed surface shift is often derived by this model.

(ii) Enhanced Bond ionization: Borgohain[26] gained the conclusion that the lattice parameter of nanoparticles contracts compared bulk counterpart based on the X-ray diffraction(XRD) observation. It suggested that an oxygen atom bonds more strongly to the Cu atoms in nanoparticles than that in huge bulk and shift the BE to high value.

(iii) Dipole effect: Dieter Schmeißer[27] ascribed dipole effect with two items to the BE shift of metal oxide nanoparticles: The first item represents a structural contribution to the interface dipole and depends on the oxide thickness and quality. The second involves the inhomogeneous charge distribution in such colloidal-like systems which vary with the size variation of nanoparticles.

(iv) Unit charge effect: Wertheim et al.[28, 29] reported that not only the BE would shift towards higher absolute value but also the Fermi edge dropped deeper at the same time as the sizes of Au and Sn nanoparticles decrease. According to the Fermi edge, the non-neutralization state in valence band induces this deeper shift during the time scale for the photoemission, and excess unite positive charge is left in nanoparticles' surface after relaxation of electron transition to core level

from valence band. Finally, it contributes a strong coulomb effect on the BE of every energy level following $e^2/R$ fashion, where $R$ denotes the diameter of nanoparticles.

(v) Initial and final state effect: in this theoretical model, the size dependent BE shift of nanoparticles was attributed to electronic configuration changes, chemical shift and relaxation shift. The electronic configuration change is due to charge redistribution of electron among different electron orbital such as *s*, *p*, and *d* bands.[30] The chemical shift is induced by variation of the chemical environment before an electron is emitted from the atom. These two contributions of electronic configuration changes and chemical shift are known as "initial State" effect, describing the core level variation before the photoelectron emission. In and after that an electron is emitted, a relaxation proceeds to dilute the impact during this photoelectron emission. The relaxation is extrinsic and is regarded as "final State" Effect. In this model, only the "initial state" effect demonstrates the "real" information from the intrinsic variation for BE shift in specimen, and "final state" effect is introduced by the XPS measurement. Thus how to identify the proportions for every item is the key point and need to be addressed clearly. However, it is very hard to gain the accurate difference between the initial and final state effect even using traditional method of Auger parameter $\alpha$.

Briefly, results show that under-coordinated systems share common yet unclear origin in splitting and shifting the core level to higher BE. However, definition of the

components is quite confusing and the origin for the surface, size and other under-coordinated systems induced core level shift is highly disputed. Therefore, consistent understanding of the effect in under-coordinated systems on the core level shift is therefore highly desirable.

## 1.3 Objectives and Scopes

Since the electronic structures of under-coordinated systems determine their abnormal performance in physical and chemical dynamics and potential industrial applications, it is very important to study and predict the behavior of those systems. Recently, the bond order length strength (BOLS) correlation has been proposed to fill the gap between the traditional continuum medium theory and quantum mechanics on predicting the behavior of under-coordinated systems. A series of analytical processes which combine the BOLS correlation, tight binding approximation and XPS measurements on the evolution of BE shift of under-coordinated systems have been performed and new method on XPS data decomposition to gain the atomic zone selective information of bonds and electrons has been discussed. Based on the accomplishments, the main objectives of this project are:

1) To synthesize various metal nanoparticles on different substrates using e-beam evaporator in ultra high vacuum (UHV).

2) To measure the morphology of nanoparticles on different substrates using transmission electron microscopy (TEM) and atomic force microscopy(AFM).

3) To investigate the BE shift of core levels and VB of nanoparticles.

4) To develop a set of analytical solution to predict the size dependent BE shift of nanoparticles and the catalytic properties.

5) To extend the applications of previous BOLS correlation to the surface strain, local atomic potential modification, local electron polarization, and related coordination number (CN) dependent BE shift of single crystal surface, terrace edge, adatoms and vacancies.

6) To gain the atomic origin for the size, surface layer(orientation), terrace edge, adatoms and vacancies dependent BE shift and the associated modifications in physical and chemical property.

## 1.4 Major Achievements

In this thesis, a thorough investigation on the BE shift of under-coordinated systems including single crystal surface, nanoparticles, terrace edge, adatoms and vacancies has been performed. The major achievements of the thesis are listed below:

1) Ni, Cu and Pt nanoparticles deposited on different substrates of $SiO_2$/Si and $SrTiO_3$(STO) have been successfully synthesized using e-beam evaporator.
2) XPS measurements on the Ni, Cu and Pt nanoparticles have been performed and the Auger electron spectroscopy (AES) was also adopted to investigate the Auger electrons of the specimens.
3) TEM and AFM measurement of the metal nanoparticles.

4) The surface atomic layer or surface orientation dependent BE shift has been deducted by re-analyzing data from published literatures for single crystal surface of W, Re, Be, Ru, Pt and Rh. A new method named atomistic photoelectron spectroscopy distillation (APSD) technique has been proposed to deal with atomic zone selective BE shift of under-coordinated systems.
5) The XPS measurements on the vacancies formed on the HOPG substrates by $Ar^+$ ion sputtering have been performed and the morphology of sample was observed using AFM.
6) Adatoms of Pt and Rh induced BE shift has been investigated using XPS measurement.
7) The origin of BE shift of under-coordinated systems has been discussed systematically using the combination of APSD method and BOLS correlation based on accurate XPS measurements.

## 1.5 Organization

This thesis mainly focuses on the BE shift of under-coordinated systems including single crystal surfaces, nanoparticles, terrace edges, adatoms, vacancies and interface of alloy. BOLS correlation is used to explore the origin for the BE shift of these systems and APSD method is used to gain the fine electronic structures. The organization of this thesis is as follows:

Chapter 1 gives a brief overview for the current research interest and the existing challenge of the divergence between experiment observations and theoretical predictions. The detailed introduction for BE shift of under-coordinated systems is given.

Chapter 2 presents theory considerations of the often-overlooked effect of surface bonds modification on the behaviors of under-coordinated systems. Following recently developed BOLS correlation, local quantum trapping induced by the atomic undercoordination and associated electronic and charge polarization have been discussed in principle and detailed mathematical expressions are developed in this chapter.

Chapter 3-6 focus on the size, surface atomic layer or surface orientation, terrace edge, adatom, vacancies and alloy interface dependent BE shift. Ni, Cu and Pt nanoparticles on $SiO_2$/Si and STO substrates are synthesized using electron beam evaporator deposition in ultrahigh vacuum(UHV) chamber and the XPS is adopted to measure the BE evolution. The XPS measurement on HOPG vacancies is performed. The surface atomic layer or surface orientation dependent BE shift of single crystal Ru, Pt, Pd, Re, Be and W are studied using existing published data. The adatoms of Pt and Rh induced BE shift is also investigated. The origin of BE shift in different specimens are studied based on the BOLS correlation and the importance of atomic undercoordination is demonstrated.

Chapter 7 summaries the work carried out in this thesis. The conclusion for

the origin of BE shift in under-coordinated systems is given. The recommendations of future research are also presented in this chapter.

# Chapter 2 Principles

## 2.1 Introduction

Since the bonds and electrons annexed the under-coordinated atoms in many systems including the flat surface, terrace edge, adatoms, defect vcacancies and nanosolids show abnormal behavior with respect to that in macro-bulk with perfect coordination, the physical quantities in those systems are no longer constant and could be tuned in a controllable way. For example, in the size transition, the under-coordinated atoms dominates the performance of nanosolids (nanowire, nanoparticles) gradually because of the increasing surface to volume ratio. As a result, they shows interesting property modifications such as band gap enlargement, positive BE shift, melting point depression, etc, which provide novel potential application in modern industry. However, how to predict the behavior of those under-coordinated systems and create a method to fine tune their properties are still lagging. Thus, the study on the electronic structure of under-coordinated systems is of great importance. Recent developed bond order length strength (BOLS) correlation has given a new path to understanding the unusual behavior of bonds and electrons in under-coordinated systems based on the consideration of bond breaking and local atomic potential modification. In this chapter, combining the tight binding approximation, the energy evolution of band and electrons annexed under-coordinated atoms is deduced and the intrinsic mechanism for BE shift in under-coordinated systems is discussed.

## 2.2 Band Dispersion and BE Shift

In one atom, electrons are trapped in atomic potential well $V_{atom}(\boldsymbol{r})$, and move around the central ion core in a standing wave form. Until now it is still hard to gain the accurate deduction for wave function of electrons from Schrödinger equation except for the hydrogen atom which only has one surrounding electron. For an isolated atom, under the assumption of the free electron gas in one dimensional potential well $V_{atom}(\boldsymbol{r})$, the corresponding wave function and eigen energy are[31]:

$$\begin{cases} \emptyset_n(\boldsymbol{r}) \propto sin(2\pi r/\lambda_n); \\ E_n = \dfrac{\hbar^2}{2m}(\dfrac{n\pi}{2d})^2; \end{cases} \qquad \frac{1}{2}n\lambda_n = 2d_0, n = 1,2,3,\ldots \tag{3}$$

Wavefunction $\emptyset_n(\boldsymbol{r})$ of the electrons in one dimension is a solution of the Schrödinger equation $H\emptyset_n(\boldsymbol{r}) = E_n\emptyset_n(\boldsymbol{r})$. $n$ is the quantum number for different energy level and $m$ is the electron mass. The energy separation between two adjacent levels depends on the subtraction of $(n+1)^2 - n^2 = 2n + 1$. As another atom closes to the original one, a binary system is formed. The interaction between the two atoms results an inter-atomic potential and discrete energy level splits into two sublevels as shown in Figure 1. The separation between the two adjacent sublevels is determined by the binary potential well; meanwhile, the interaction shifts the center of the two levels down. As the volume increases gradually, the coulomb interaction between the atom cores and the electrons splits the energy the electrons

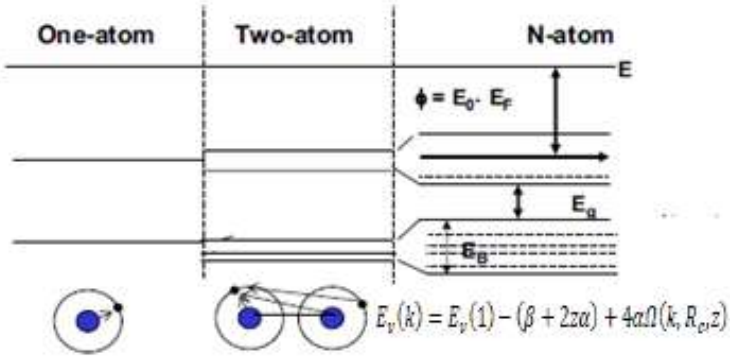


Figure 1 Evolution of a single energy level into the band structure when particle grows from a single atom to a bulk solid that contains $N_j$ atoms. Indicated is the work function W, band gap $E_g$, and bandwidth. The number of allowed sublevels in a certain band equals the number of atoms of the solid.

Splits the electrons splits the energy levels, spreading them into bands, accompanying with the periodic atom arrangement. F.Bloch proposed the wavefunction of the electrons in periodic potential well must be of a special form:

$$\varphi_{\boldsymbol{k}}(\boldsymbol{r}) = u_{\boldsymbol{k}}(\boldsymbol{r})\exp\,(i\boldsymbol{k}\cdot\boldsymbol{r}) \tag{4}$$

Where $u_k(\boldsymbol{r})$ has the period of the crystal lattice in form of $u_{\boldsymbol{k}}(\boldsymbol{r}) = u_{\boldsymbol{k}}(\boldsymbol{r}+\mathbf{T})$ with translation operator **T**. To solve the corresponding Schrödinger equation, adopting tight binding approximation, the electrons in the solid with periodic lattice are mainly affected by intra atomic potential $V_{atom}(\boldsymbol{r})$. The Hamilton of crystal is written as:

$$\widehat{\boldsymbol{H}} = \widehat{\boldsymbol{H}}_0 + \widehat{\boldsymbol{H}}' = -\frac{\hbar^2\boldsymbol{\nabla}^2}{2m} + V_{atom}(\boldsymbol{r}) + V_{crys}(\boldsymbol{r}+R_C) \tag{5}$$

Where $\widehat{\boldsymbol{H}}' = V_{crys}(\boldsymbol{r}+R_C)$ demonstrates the interaction between electrons of one atom and all other atoms in periodic structure. $R_C$ is the periodic lattice constant,

Under this approximation, each state of given quantum number of the free atom is spread in the crystal into a band of energy, and the orbital of electrons in crystal are the linear orbital combination of electron in every free atom. Suppose that the ground state of an electron moving in the potential $V_{atom}(\boldsymbol{r})$ of an isolated atom is $\emptyset_{\boldsymbol{k}}(\boldsymbol{r})$,

$$\left[-\frac{\hbar^2\boldsymbol{\nabla}^2}{2m}+V_{atom}(\boldsymbol{r})\right]\emptyset_{\boldsymbol{k}}(\boldsymbol{r})=E(1)\emptyset_{\boldsymbol{k}}(\boldsymbol{r}) \tag{6}$$

Where $E(1)$ is energy level of the electron in an isolated atom. We obtain an approximate wavefunction $\varphi_{\boldsymbol{k}}(\boldsymbol{r})$ for one electron in whole crystal with N atoms:

$$\varphi_{\boldsymbol{k}}(\boldsymbol{r})=\sum_j C_{\boldsymbol{k}j}\,\emptyset_{\boldsymbol{k}}(\boldsymbol{r}-\boldsymbol{r_j}) \tag{7}$$

Under periodic potential, $\varphi_{\boldsymbol{k}}(\boldsymbol{r})$ must be of the Bloch form. If $C_{\boldsymbol{k}j}=N^{-1/2}\exp(i\boldsymbol{k}\cdot\boldsymbol{r_j})$, it gives:

$$\varphi_{\boldsymbol{k}}(\boldsymbol{r})=N^{-1/2}\sum_j^N \exp(i\boldsymbol{k}\cdot\boldsymbol{r_j})\emptyset_{\boldsymbol{k}}(\boldsymbol{r}-\boldsymbol{r_j}) \tag{8}$$

Considering a translation **T** connecting two lattice points:

$$\begin{aligned}\varphi_{\boldsymbol{k}}(\boldsymbol{r}+\boldsymbol{T}) &= N^{-\frac{1}{2}}\sum_j \exp\left(i\boldsymbol{k}\cdot\boldsymbol{r_j}\right)\emptyset_{\boldsymbol{k}}\left(\boldsymbol{r}+\boldsymbol{T}-\boldsymbol{r_j}\right)\\ &= \exp(i\boldsymbol{k}\cdot\boldsymbol{T})\,N^{-\frac{1}{2}}\sum_j \exp\left(i\boldsymbol{k}\cdot(\boldsymbol{r_j}-\boldsymbol{T})\right)\emptyset_{\boldsymbol{k}}\left(\boldsymbol{r}-(\boldsymbol{r_j}-\boldsymbol{T})\right)\\ &= \exp(i\boldsymbol{k}\cdot\boldsymbol{T})\emptyset_{\boldsymbol{k}}(\boldsymbol{r})\end{aligned} \tag{9}$$

The energy of electrons could be calculated following Schrödinger equation:

$$E(\boldsymbol{k}) = \langle \boldsymbol{k} | \widehat{\boldsymbol{H}} | \boldsymbol{k} \rangle = \frac{1}{N} \sum_j \sum_{j'} \exp\left(i\boldsymbol{k} \cdot (\boldsymbol{r}_j - \boldsymbol{r}_{j'})\right) \langle \emptyset_k(\boldsymbol{r} - \boldsymbol{r}_{j'}) | \widehat{\boldsymbol{H}} | \emptyset_{\boldsymbol{k}}(\boldsymbol{r} - \boldsymbol{r}_j) \rangle \tag{10}$$

Where the double summation over $j$ and $j'$ extends over all the atoms in the lattice. For each particular choice of $j'$ the sum over $j$ yields the same result, and since $j'$ can take N different values, one obtains N equal terms, which leads:

$$E(\boldsymbol{k}) = \sum_{j=-N/2}^{(N-1)/2} \exp\left(i\boldsymbol{k} \cdot \boldsymbol{r}_j\right) \langle \emptyset_k(\boldsymbol{r}) | \widehat{\boldsymbol{H}} | \emptyset_{\boldsymbol{k}}(\boldsymbol{r} - \boldsymbol{r}_j) \rangle \tag{11}$$

if we have arbitrarily put $\boldsymbol{r}_j = 0$ $(j = 0)$. $E(\boldsymbol{k})$ is written in form of:

$$E(\boldsymbol{k}) = \langle \emptyset_k(\boldsymbol{r}) | \widehat{\boldsymbol{H}} | \emptyset_{\boldsymbol{k}}(\boldsymbol{r}) \rangle + \sum_{j \neq 0} \exp\left(i\boldsymbol{k} \cdot \boldsymbol{r}_j\right) \langle \emptyset_k(\boldsymbol{r}) | \widehat{\boldsymbol{H}} | \emptyset_{\boldsymbol{k}}(\boldsymbol{r} - \boldsymbol{r}_j) \rangle \tag{12}$$

In tight binding approximation, the potential vector in Hamilton of crystal is divided into the atomic crystal potential $V_{atom}(\boldsymbol{r})$ and potential well $V_{crys}(\boldsymbol{r} + R_C)$. $V_{crys}(\boldsymbol{r} + R_C)$ could be written as:

$$V_{crys}(\boldsymbol{r} + R_C) = \sum_{j \neq 0} \boldsymbol{v}(\boldsymbol{r} - \boldsymbol{r}_j) \tag{13}$$

In this condition, $E(\boldsymbol{k})$ is:

$$E(\boldsymbol{k}) = \left\langle \emptyset_k(\boldsymbol{r}) \middle| -\frac{\hbar^2 \boldsymbol{\nabla}^2}{2m} + V_{atom}(\boldsymbol{r}) \middle| \emptyset_{\boldsymbol{k}}(\boldsymbol{r}) \right\rangle + \left\langle \emptyset_k(\boldsymbol{r}) \middle| V_{crys}(\boldsymbol{r} + R_C) \middle| \emptyset_{\boldsymbol{k}}(\boldsymbol{r}) \right\rangle$$
$$+ \left\langle \emptyset_k(\boldsymbol{r}) \middle| -\frac{\hbar^2 \boldsymbol{\nabla}^2}{2m} + V_{atom}(\boldsymbol{r}) \middle| \emptyset_{\boldsymbol{k}}(\boldsymbol{r} - \boldsymbol{r}_j) \right\rangle$$
$$+ \left\langle \emptyset_k(\boldsymbol{r}) \middle| V_{crys}(\boldsymbol{r} + R_C) \middle| \emptyset_{\boldsymbol{k}}(\boldsymbol{r} - \boldsymbol{r}_j) \right\rangle$$
$$= E_v(1) - (\beta + 2\alpha) + 4\alpha\Omega(k, R_c, z)$$

(14)

Where:

$$\begin{cases} E_v(1) = \left\langle \emptyset_k(\boldsymbol{r}) \middle| -\frac{\hbar^2 \boldsymbol{\nabla}^2}{2m} + V_{atom}(\boldsymbol{r}) \middle| \emptyset_k(\boldsymbol{r}) \right\rangle \\ \beta = -\left\langle \emptyset_k(\boldsymbol{r}) \middle| V_{crys}(r + R_C) \middle| \emptyset_k(\boldsymbol{r}) \right\rangle \\ \alpha = \sum_{j=CN} \left\langle \emptyset_k(\boldsymbol{r} \middle| V_{crys}(r + R_C) \middle| \emptyset_{\boldsymbol{k}}(\boldsymbol{r} - R_c \right\rangle \\ \Omega(k, R_C, z) = \sum_z sin^2\left(\frac{kR_C}{2}\right) \end{cases}$$

(15)

The variable $\alpha$ and $\beta$ represent the overlap and exchange integration upon the crystal potential $V_{crys}(r + R_C)$. The width of energy band equals $4\alpha\Omega(k, R_c, z)$. It could be observed directly that the energy level evolution is dominated by the interaction and exchange integration $\beta$ and $\alpha$ under crystal potential $V_{crys}(r + R_C)$, and $4\alpha\Omega(k, R_c, z)$ represents the band spreading width. Thus, according to the tight binding approximation, the difference between the energy for electron in an islaoted atom and perfect single crystal is defined as the bulk shift following:

$$\Delta E_v(\infty) = E_v(k) - E_v(1) = -(\beta + 2\alpha) + 4\alpha\Omega(k, R_c, z)$$

(16)

From the XPS spectrum which could detect binding energy of electrons in different structure, since maximal width of the bulk component is (0.1-1.0 eV level), one can estimate that the $\alpha$ is in $<10^{-(1\sim2)}$ eV order.[32] The $\beta$ is in the $10^0$ eVs level. Therefore, the BE shift is dominated by $\beta$ and proportional to the crystal potential $V_{crys}(r + R_C)$. Any modification to the crystal potential $V_{crys}(r + R_C)$ will take effect on the coefficient $\beta$, which could shift the energy level to high or low value depending on the external impact.

From this expression for the energy band evolusion indicated above, any external impact on the potential well ($V_{atom}(\boldsymbol{r}) + V_{crys}(r + R_C)$) will shift the position of energy level. In many materials and structure systems, since they are not in state with perfect atomic arrangement, the energy level of electrons in those substances will be definitely different from that in an isolated atom or perfect single crystal and depends on the modification of potential well.

# 2.3 BOLS: Coordination Number Imperfection

The atomic coordination number (CN) on flat surface is less than that in the bulk interior because of the lattice periodicity termination, which is defined as CN imperfection. Another example of CN imperfection is nanosolids. Not only the increased volume of surface atoms but also certain enlarged surface curvature causes

a much stronger CN imperfection in nanosolids than that on flat surface. The variation on the atomic CN plays a critical role in the performance of materials.

Pauling[33] and Goldschmidt[34] had indicated that, if the CN of an atom is reduced, the ionic and the metallic radius of the atom would shrink spontaneously. The CN imperfection shortens the bonds between the under-coordinated atoms, disregarding the nature of the specific chemical bond[35] or the structural phase.[35] The diameter of an under-coordinated atom would shrink spontaneously by 3%, 4%, 12% as its CN is reduced from standard value 12 to 8, 6, 4, respectively. Feibelman[36] has noted a 30% length contraction of the dimer bond (CN=2) of Ti and Zr, regardless of structural phase of the substance. Similar CN imperfection induced bond contraction has been observed in nanosolids.[37-43] For example, Comaschi[44] observed 0.14%, 0.24%, 0.31%, and 1.01% of bond contraction in Au nanoparticles, which corresponds to CN = 11.8, 11, 10.5 and 9, respectively. The bond contraction for the palladium nanoparticles deposited on the $\gamma$-$Al_2O_3$ substrate has been confirmed to be 5% as its diameter decreases to 1.5 nm.[45] Similar results that a 3.5% bond contraction in palladium nanoparticles on polymer matrix have been reported by Lamber et al.[39] as the size of particle is 2 nm. We use the CN=12 as the standard criteria to correspond the bulk state, the premise of Goldsmidt-Pauling-Feibelman bond contraction from the subject of the BOLS correlation can be expressed as:

$$c_i(z_i) = \frac{d_i}{d_0} = 2/(1 + exp\left[\frac{12 - z_i}{8z_i}\right]) \quad (bond\ contraction)$$

(17)

The subscript $i$ and $b$ denote an atom in the $i$th atomic layer and perfect bulk, respectively. $z_i$ is the atomic CN for the atom in $i$th layers The coefficient $c_i(z_i)$ represents the ratio of bond contraction of at $i$th surface layer for the atomic CN=$z_i$, compared with the atomic bond length $d_0$ in bulk. Figure 2 (a) shows the comparison of the CN induced bond contraction between the experimental data and that proposed in BOLS correlation. The prediction for the bond contraction has been well estimated by experimental results. The bond contraction which represents the enhanced atomic interaction modifies the local potential well surrounding the under-coordinated atom. Figure Figure 2(b) schematically demonstrates the potential well modification as a function of the atomic bond length by adopting the pairing atomic potential, $u(r)$. Traditional Lennard-Jones potential expression of $u(r)$ is:

$$u(r) = 4\varepsilon[\left(\frac{\sigma}{r}\right)^{12} - \left(\frac{\sigma}{r}\right)^{6}]$$

(18)

Where $\varepsilon$ is the depth of potential well and $\sigma$ is the finite atomic distance at equilibrium point. $r = r_0$ is the equilibrium distance between two atoms. The variation of potential well $u(r)$ is decided by the atomic distance $r$ as described in Figure 2(b). There are several characteristic energies in Figure 2(b): $T_{m,i}$ represents the local melting point, which is proportional to the atomic cohesive energy, $z_iE_i(0)$, per atom; The separation $\eta_{2i}$ between $E = 0$ and $E_i(T_{m,i})$, is $1/z_i$ fold energy that is required for atomization of an

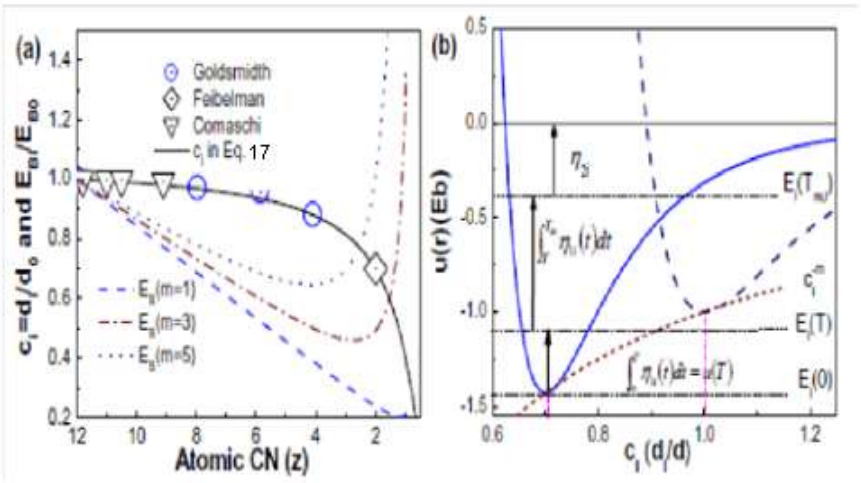


Figure 2 Illustration of the BOLS correlation. Solid line in (a) corresponds to the bond contraction coefficient with literature data from Goldschmidt (circles)[34], Feibelman (square)[36], and Comashchi (down triangle)[44]. The atomic cohesive energy with different *m* is also shown in (a). (b) Atomic CN imperfection modified pairing potential energy.

atom in molten state. The separation between $E_i(0)$ and the $E_i(T)$ ($=\int_0^T \eta_{1i}(t)\ dt$) is the thermal vibration energy or specific internal energy, representing the energy required to break pairing bond in thermal or mechanical path. The separation between $E_i(T_{m,i})$ and $E_i(T)$ ($=\int_T^{T_{m,i}} \eta_{1i}(t)\ dt$) corresponds to the energy for melting. Thus $\eta_{1i}$ demonstrates the specific heat per bond. From Figure 2(b) with decreasing the bond length, the crystal potential well will increase following the times of $c_i^{-m}$. The variable *m* represents the bond nature of substance and has been optimized by many material systems: for metal, *m*=1[46-50]; for elementary semiconductor and insulator, the value of *m* is always more than 1. It has been estimated *m* = 4.88 and 2.56 for silicon[51] and carbon allotropies,[16] respectively. For compounds, the value of *m* should be determined by fitting a quantity varying with the change of both sample size and composition.[52] The enhanced crystal potential induced by the bond

contraction confirms that near the under-coordinated site a local quantum trapping (T state) is formed. As a result, a additional potential perturbation is created and will

influence the Hamilton vector. According to the conclusion from the tight binding approximation and the undercoordination induced potential perturbation, the Hamilton for an electron surrounding under-coordinated atoms is changed as:

$$\begin{cases} \widehat{H} = \widehat{H}_0 + \widehat{H}' = -\dfrac{\hbar^2\nabla^2}{2m} + V_{atom}(r) + V_{crys}(r + R_C)(1 + \Delta_H) \\ \Delta_H = c_i^{-m} - 1 \end{cases} \tag{19}$$

Where $\Delta_H$ demonstrates the perturbation of undercoordination induced local quantum trapping. Because the energy level of electrons is decided by the Hamiltonian, Following the Eq.(14), the band dispersion in Eq.19 evolves as:

$$E_v(k) = E_v(1) + \Delta E_v(\infty)(1 + \Delta_H) \tag{20}$$

or,

$$\begin{cases} \dfrac{E_v(k) - E_v(1)}{E_v(\infty) - E_v(1)} = (1 + \Delta_H) \\ \Delta_H = c_i^{-m} - 1 \end{cases} \tag{21}$$

From this equation, we could gain that the greater the bond contraction, the stronger BE shift.

Except for the modified energy level of electrons, the related parameters to characterizing the bond nature are also been changed following as:

$$\begin{cases} E_i = c_i^{-m} E_b & (single\ bond\ energy) \\ E_{B,i} = z_i E_i & (cohesive\ energy) \\ E_d(z_i) = c_i^{-m+3} E_d & (bond\ energy\ density) \end{cases} \tag{22}$$

$E_i$ and $E_b$ represent the single bond energy of *i*th atomic layer and perfect bulk. The spontaneous bond contraction surrounding the under-coordinated atoms makes the bond energy to be modified from $E_b$ to $E_i$ with times of $c_i^{-m}$. As show in Eq.22, if the bond contraction coefficient $c_i$ is smaller than 1, the single bond energy will be enhanced and the bond energy density $E_d(z_i)$ is also increased since the volume of real space is decreased. The cohesive energy $E_{B,i}$ per atom for the under-coordinated atom at *i*th surface layers is defined as the sum of all surrounding bonds, its variation depends on not only the single bond energy $E_i$ but also the atomic CN=$z_i$ as shown in the expression.

# 2.4 BOLS in Nanosolids

BOLS correlation demonstrates the relation between the bond contraction and the CN imperfection. The perturbation $\Delta_H$ to Hamiltonian of electrons induced by the crystal potential modification decides the energy level shift. In nanosolids, the CN imperfection turns out at the surface region and atomic CN in interior is still same as

that in perfect bulk, which has been estimated by experiments[40, 53] and molecular dynamics calculation.[42]

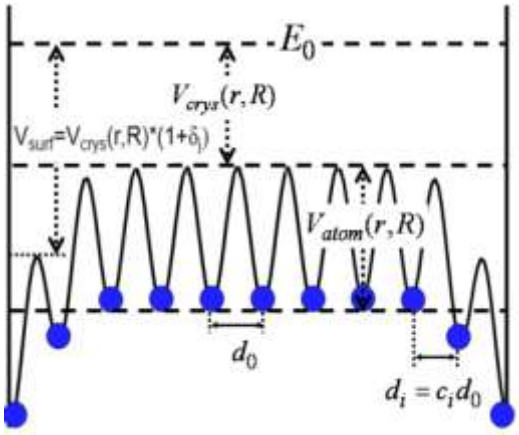


Figure 3 Schematic illustration of undercoordination induced surface modification on the potential well. The potential well at under-coordinated site is perturbed in a ratio of $\delta_j$in which represents the localization and densification of potential well.

Figure 3 shows the typical potential well modification of a nanoparticle. The potential well involves two components of intra-atomic trapping potential $V_{atom}(r,R)$ and inter-atomic trapping potential $V_{crys}(r,R)$. The $V_{atom}(r,R)$ is defined to confine the electrons surrounding the nuclei and the $V_{crys}(r,R)$ represents the interaction between atoms. As the CN imperfection at surface region induces atomic bond contraction, the $V_{crys}(r,R)$ becomes deeper than that in the inner core. Thus, the local potential well height at such region is increased, as well the energy densification by the bond energy enhancement. The local potential well enhancement provides a perturbation $\Delta_H$ to the Hamiltonian of a certain electrons bonded to the under-coordinated surface atoms following Eq.19. Considering an assembly composed *n* particles with mean size of $K_j$. There are $N_j$ atoms in every particle. The

total crystal potential well, $V_{crys}(r,n,N_j)$:

$$V_{crys}(r,n,N_j)=\sum_{n}\sum_{l\neq i}\sum_{i}v(r_{li})=\frac{n}{2}\left[N_j\sum_{i=1}v(r_{li})+\sum_{i=1}V(K_{nj})\right]$$

$$\cong\frac{n}{2}\left[{N_j}^2v(d_0)+nV(K_{nj})\right]$$

(23)

Where $V_{crys}(r,n,N_j)$ sums all the $n*N_j$ atoms in the assembly with $n$ nanoparticles. $r_{li}$ is a certain fold of the nearest atomic spacing $d_0$. $V(K_{nj})$ is the interaction between $n$ nanoparticles. Generally, the distance between those nanoparticles is very large and the inter-nanoparticles interaction is weak enough to be negligible. As the local potential modification in format of $d_0$ to $d_i$, there is:

$$V_{crys}(r,n,N_j)=\frac{nN_j}{2}\left[N_iv(d_i)+(N_j-N_i)v(d_0)+\frac{n}{N_j}V(K_{nj})\right]$$

$$=\frac{n{N_j}^2v(d_0)}{2}\left[\frac{N_iv(d_i)}{N_jv(d_0)}+\left(1-\frac{N_i}{N_j}\right)+\frac{n}{{N_j}^2v(d_0)}V(K_{nj})\right]$$

$$=V_{crys}(d_0,n,N_j)\left[1+\gamma_{ij}\left(\frac{v(d_i)}{v(d_0)}-1\right)+\frac{n}{{N_j}^2v(d_0)}V(K_{nj})\right]$$

$$\cong V_{crys}(d_0,n,N_j)\left[1+\gamma_{ij}(\frac{v(d_i)}{v(d_0)}-1)\right]$$

(24)

And

$$\frac{\Delta V_{crys}(d_i,N_j)}{V_{crys}(d_0,\infty)}=\frac{V_{crys}(d_i,N_j)-V_{crys}(d_0,\infty)}{V_{crys}(d_0,\infty)}=\sum\gamma_{ij}(\frac{v(d_i)}{v(d_0)}-1)$$

(25)

Where $V_{crys}(d_0, n, N_j)$ is the crystal potential of bulk solid without under-coordinated atoms. The crystal potential $v(d_i)$ for every under-coordinated atom relates to the perturbation $\Delta_H$ as shown in Eq.25. The weighting factor, $\gamma_{ij}$, represents the geometrical contributions from dimension ($K$) and dimensionality ($\tau$), which describes the contribution from the affected volume to the entire specimen. Atoms in no more than 3 outermost surface layers suffer the CN imperfection and that in interior core has perfect coordination, which has been confirmed by the experimental observations.[37-43] For example, a combination of STM/S measurements and density functional theory (DFT) calculations has revealed that the mean lattice constant of Co nano-islands deposited on copper substrates contracts by 6% from the bulk value of 0.251 nm at center to 0.236 nm at the edge of the nano-islands. Using electron cohesive diffraction, Huang et al.[53] confirmed that the Au-Au bond contraction happens only to the outermost two atomic layer spacing of a gold nanosolids in a radial way, yet, the Au-Au bond in the core interior of the particle remains its bulk value. Thus, there is:

$$\frac{\Delta V_{crys}(d_i, N_j)}{V_{crys}(d_0, \infty)} = \sum_{j\leq 3} \gamma_{ij}\left(\frac{v(d_i)}{v(d_0)} - 1\right) = \sum_{j\leq 3} \gamma_{ij}\left(\frac{\Delta v(d_i)}{v(d_0)}\right) = \sum_{j\leq 3} \gamma_{ij}(c_i^{-m} - 1) \tag{26}$$

For nanosolids of thin plate, nanowire and nanoparticles, $\gamma_{ij}$ is calculated as:

$$\gamma_{ij} = \begin{Bmatrix} \dfrac{S \times d_i}{S \times t} = \dfrac{c_i}{K} & thin\ plate \\ \dfrac{L \times d_i \times 2\pi r}{L \times \pi r^2} = \dfrac{2c_i}{K} & nanowire \\ \dfrac{4\pi r^2 \times d_i}{\frac{4}{3}\pi r^3} = \dfrac{3c_i}{K} & nanoparticle \end{Bmatrix}$$

(27)

Where *S*, *L*, and *r* represent the surface area, length and radius of thin plate, nanowire(rod) and nanoparticles, respectively. *t* is the thickness of thin plates. K is the dimensionless form to describe the size of nanosolids, for thin plates, $K = t/ d_0$; for nanowire(rod) and nanoparticles, $K = r/ d_0$. As the *K* is the dimensionless size, from above equation, $\gamma_{ij}$ could be described in a uniform expression:

$$\gamma_{ij} = \frac{\tau c_i}{K} \quad \begin{cases} \tau = 1, & thin\ plate \\ \tau = 2, & nanowire \\ \tau = 3 & nanoparticle \end{cases}$$

(28)

The perturbation covers the weighted sum of contribution from three outermost 3 surface layers of nanosolids in format of ($c_i^{-m}$-1) as shown in above equations. Consequently, the entire potential well for nanosolids evolves:

$$\begin{cases} V(\Delta_H) = V_{atom}(r) + V_{crys}(r + R_C)(1 + \Delta_H) \\ \Delta_H = \sum_{j \le 3} \gamma_{ij}(c_i^{-m} - 1) \end{cases}$$

(29)

Thus, the energy level for certain nanosolids is:

$$\begin{cases} E_v(k) = E_v(1) + \Delta E_v(\infty) = E_v(1) + \Delta E_v(\infty)(1 + \Delta_H) \\ \Delta_H = \sum_{j \le 3} \gamma_{ij} (c_i^{-m} - 1) \end{cases}$$

(30)

The evolution of energy level of nanosolids and the bulk shift $\Delta E_v(\infty)$ could be represented as:

$$\frac{\Delta E_v(K_j)}{\Delta E_v(\infty)} = \frac{E_v(K_j) - E_v(1)}{E_v(\infty) - E_v(1)} = \Delta_H = \sum_{j \le 3} \gamma_{ij} (c_i^{-m} - 1)$$

(31)

In conclusion, in BOLS correlation, CN imperfection induced local crystal potential modification ($\Delta_H$) changes the crystal potential well and energy level to be:

$$\begin{cases} V(\Delta_H) = V_{atom}(r) + V_{crys}(r + R_C)(1 + \Delta_H) \\ E_v(\Delta_H) = E_v(1) + [E_v(\infty) - E_v(1)](1 + \Delta_H) \\ E_v(\Delta_H) = E_v(\infty) + [E_v(\infty) - E_v(1)]\Delta_H \end{cases}$$

(32)

And $\Delta_H$ could be presented following Eq.31:

$$\Delta_H = \begin{cases} \Delta_i(S_i) = \dfrac{E_i - E_b}{E_b} = c_i^{-m} - 1 & undercoordinated\ atom \\ \Delta_j(K_j) = \sum_{i \le 3} \gamma_{ij}\, \Delta_i(S_i) & nanosolids \end{cases}$$

(33)

Such modification of $\Delta_H$ to the Hamiltonian of entire specimen relates directly to the energy level under different extent:

$$\begin{cases} \dfrac{E_v(\Delta_{H'}) - E_v(1)}{E_v(\Delta_H) - E_v(1)} = \dfrac{(1+\Delta_{H'})}{(1+\Delta_H)} \\ \dfrac{E_v(\Delta_{H'}) - E_v(\infty)}{E_v(\Delta_H) - E_v(\infty)} = \dfrac{\Delta_{H'}}{\Delta_H} \end{cases} \qquad (H' \neq H)$$

(34)

As a XPS profile is given, one can calculate the energy level of isolated atom by decomposing spectrum to every single surface layers and bulk components or comparing different size of specimen with accurate size measurement. Thus, there is

$$E_v(1) = \frac{(1+\Delta_{H'})E_v(\Delta_H) - (1+\Delta_H)E_v(\Delta_{H'})}{\Delta_{H'} - \Delta_H}$$

(35)

As the $\Delta E_v(\infty) = E_v(\infty) - E_v(1)$, the above equation evolves:

$$E_v(1) = E_v(\infty) - \frac{E_v(\Delta_H) - E_v(\infty)}{\Delta_H}$$

(36)

It should be noted if there are $l$ (>2) components after XPS spectrum decomposition, the $\Delta E_v(\infty)$ and $E_v(1)$ can be taken the average of the $C_l^2 = \frac{l!}{[(l-2)!2!]}$ possible combinations with a standard derivation $\sigma$ as both $E_v(1)$ and $\Delta E_v(\infty)$ are independent of particle dimension or surface relaxation.

# 2.5 BOLS: Polarization

According to the BOLS scheme, bonds between under-coordinated atoms are shorter and stronger. Local quantum trapping and densification of charge and energy perturb the interatomic potential. On the other hand, polarization of the electrons at the

upper-edge of energy band by the locally, densely, and entrapped core electrons also provide perturbation to the energy level through screening and splitting the crystal potential. Figure 4 gives a schematic description for the electron state at the upper band arising from the nonbond electrons polarization: As the bond length decreases from $d_0$ to $d_i$ because of the CN imperfection, the local quantum trapping(T) induced by the crystal potential modification shifts the energy level of bonding band towards deeper position, accompanying with the space volume densification as shown in Figure 4. The entrapped core charge polarizes the unpaired dangling-bond electrons to higher position, which in turn screen and split the potential and then generate the P component in the upper edge of the core band. Thus, the modification in the crystal potential presents in two types of perturbation:

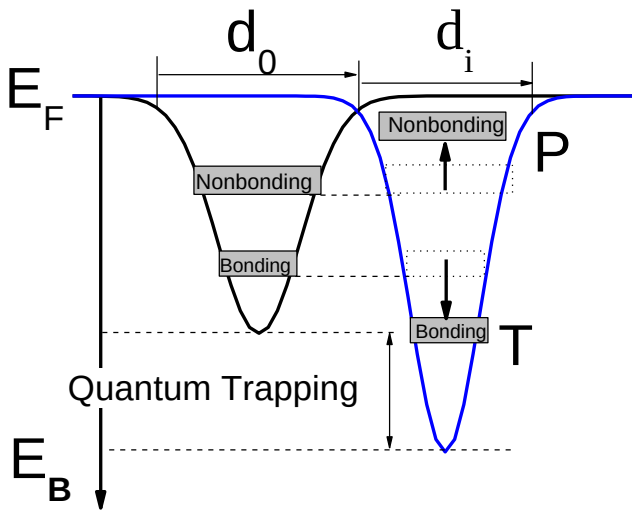


Figure 4 Electron polarization(P) induced by the Local quantum trapping (T) and densification of charge and energy.

$$\begin{cases} T = \begin{cases} c_i^{-m} \\ \sum_{i\leq 3} \gamma_{ij}\,\Delta_i(S_i) \end{cases} & (trapping) \\ p = \dfrac{[E_v(p) - E_v(0)]}{[E_v(\infty) - E_v(0)]} & (Polarization) \end{cases}$$

(37)

$E_v(p)$ represents the peak energy of the polarization component. $E_z$ and $E_o$ represent the bond energy for CN = z and bulk, respectively. The $p$ is the coefficient of polarization to be determined from the XPS measurement. Thus, correlation between the XPS components follows the criterion,

$$\frac{E_v(x) - E_v(0)}{E_v(\infty) - E_v(0)} = \begin{cases} c_i^{-m} & (Entrapment) \\ p & (polarization) \end{cases}$$

(38)

The x represents z or $p$. If the polarization-entrapment coupling effect is apparent, the term $c_i^{-m}$ is then replaced by $pc_i^{-m}$, the trapped states will be moved up from the otherwise low-z position to energy closing to the bulk component.

# 2.6 Introduction of X-Ray Photoelectron Spectroscopy

X-ray photoelectron spectroscopy (XPS) is a quantitative spectroscopic technique that measures the elemental composition, empirical formula, chemical state and electronic state of the elements that exist within a material. XPS was developed in the mid 1960s by K. Siegbahn and his research group. The phenomenon is based on the photoelectric effect outlined by Einstein in 1905. XPS spectra are obtained by irradiating a material with a beam of X-rays while simultaneously measuring the kinetic energy and number

of electrons that escape from the top 1 to 10 nm of the material being analyzed as described in Figure 5. The basic equation describe such dynamic process is: $E(K) = h\upsilon - E(B) - \phi$, where $h\upsilon$ is the photo energy of incident X-ray and $E(K)$, $E(B)$ and $\phi$ are the kinetic energy of detected photoelectron, binding energy of electrons at certain orbital and workfunction of samples, respectively. Generally, Al $K_\alpha$ (1486.6 eV) or Mg $K_\alpha$ (1253.6 eV) are often the photon energies of choice. XPS measurement could give much information the electronic structure of matter from which they were excited by monitoring the Momentum and energy of the photoelectrons. Except for providing the chemical state of corresponding element in materials, it also could perform depth profiling be remove atoms layer by layer and

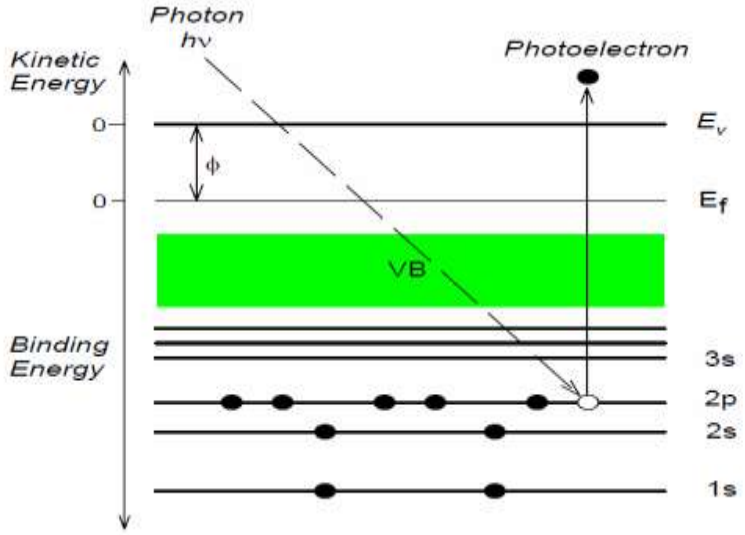


Figure 5 The schematic description for the photoelectron emission process.

the quantitative analysis for the atomic ratio of elements. A new way to get more insight into the sample is to measure a number of spectra at different measuring angles. Variation of the emission angle causes changes in the effective information

depth of analysis: at glancing incidence (small angles) only the upper layers of the sample are examined; at high measuring angles deeper layers are detected. This a easy way to detect the depth-resolved electron structure of sample without any destruction.

## 2.7 Conclusion

In this chapter, we introduced a new theoretical model of the BOLS correlation on the BE shift of under-coordinated systems. The main core of BOLS correlation was described that CN imperfection induced local quantum trapping and related energy and charge polarization takes effect on the Hamiltonian of specimen and consequently determines the energy level evolution.

# Chapter 3 Atomic Layer and Orientation Resolved Surface BE Shift

## 3.1 Introduction

Surface BE shift in core level and VB has been observed in many materials and was studied extensively. For example, a surface BE shift of 0.17 eV towards higher BE than the bulk for the 4f peak of atomically rough Re(12$\bar{3}$1) surface was observed by Chan et al. using synchrotron radiation measurement,[54] with different photon energies and emission angles. For *bcc* metal W and Ta, it has been reported that obvious surface BE shift was observed for the (100), (110) and (111) surface.[55, 56] A positive surface BE shift on three facets of Ta is gained and inverse order assignment for that on W surface. The origin of surface BE shift has been discussed broadly, contradictory conclusions always were gained since the analysis to the BE shift was always based on the single specimen or experiment. The core level, being a superposition of the intra-atomic trapping and the interatomic binding (crystal potential) contributions, of values for different elements can be determined easily by XPS, but the discrimination of the two identities from intra- or inter atomic interaction is infrequent and indirect due to the lacking of suitable guidelines from the perspective of the intrinsic Hamiltonian perturbation. One often takes the bulk component as the reference with zero energy shift as the determination of the actual bulk shift from the energy level of an isolated atom is hardly possible. Such a

zero-bulk-shift assumption annihilates plenty of useful information such as the energy level of an isolated atom and its bulk shift that is non zero according to energy band theory.

The BOLS correlation mechanism[57] indicates that the remaining bonds of an under-coordinated atom contract and strengthen spontaneously, leading to the formation of a local strain and quantum trapping, and also the densification of charge and energy at local sites around the original atomic defects, adatoms, surfaces, grain boundaries, dislocations, terrace edges, dimers, atomic chains, atomic sheets, hollow tubes, or skin depth of nanostructures and nanocavities. With this physical picture of atomic CN imperfection as the basis, the BOLS can account for the size-induced BE shifts, band gap expansion, solid-liquid transition, and surface and nanostructure mechanical strength.

In this chapter, several surfaces of single crystal metal have been adopted to study the surface BE shift. Combining the BOLS correlation and XPS measurements, the origin of surface BE shift is discussed.

## 3.2 *Fcc* structured Pd and Rh surfaces

Using high-resolution XPS, Anderson et al.[58] measured systematically the orientation-resolved $3d_{5/2}$ spectra of the (111), (110) and (100) surfaces of Pd and Rh at a photon energy of 390 eV. Using *ab initio* calculations based on the final-initial states model, they suggested that the surface induces negative shifts that vary from

0.25 to 0.60 eV, depending on the orientations and materials. Baraldi et al.[59] recently measured the Rh surface BE shift at photon energy of 380 eV and with polar emission angles varying from 20° to 50° with respect to the surface normal. Results showed that the smaller polarization angle from the Rh(111) surface derives a relatively higher intensity of the high-energy bulk component, being consistent with the observations.[25, 60-63]

In chapter 2, according to the surface BE shift, we have the relation:

$$\begin{cases} E_v(\Delta_H) = E_v(1) + [E_v(\infty) - E_v(1)](1 + \Delta_H) \\ E_v(\Delta_H) = E_v(\infty) + [E_v(\infty) - E_v(1)]\Delta_H \\ Bulk = B = \infty \end{cases}$$

Where the

$$\Delta_H = \Delta_i(S_i) = \frac{E_i - E_b}{E_b} = c_i^{-m} - 1$$

Using those equations, the BE of an isolated atoms has been gained as:

$$E_v(1) = \frac{(1 + \Delta_{H'})E_v(\Delta_H) - (1 + \Delta_H)E_v(\Delta_{H'})}{\Delta_{H'} - \Delta_H}$$

and its bulk shift $\Delta E_v(\infty)$ and the effective CNs of the first layer at different orientations through analyzing the measurements of surface core-level shift.

As followed BOLS correlation, the contracted length of a bond of an under-coordinated surface atom in the *i*th layer, $d_i$, is related to the length of a bond in the bulk solid of the same material, $d_0$, by the bond contraction coefficient, $c_i$. This parameter is dependent on the coordination of the atom, $z_i$ for all kinds of chemical bonds. The $z_1$ ($i$ = 1) should vary slightly with crystal orientation but the confirmation

has been impossible up to now. Intuitively, one often takes $z_1$= 6 for an *fcc* structure but available data favors the effective $z_1$ value of 4 (with $c_i$ ~12%) or around.[57, 61, 62] Also, the magnitude of a remaining bond's BE of an under-coordinated surface atom ($E_i$) increases as the bonds contract spontaneously, and is equal to the "$c_i^{-m}$" multiple of the energy of a single bond in a bulk sample ($E_b$). The parameter *m*, which is not freely adjustable, characterizes the nature of a bond in a solid, or otherwise deciphered as the parameter relating the bond energy to its length. For pure metal, the m has been optimized as one.[57]

Figure 6 illustrates the BOLS-derived BE shift of surface component layers. $E_v(1)$ is the energy level of an isolated atom, from which the BE shifts. $S_1$($z_1 \cong 4$) and $S_2$ ($z_2 = z_1$+2) correspond to the top and the second atomic layer and *B* the bulk components. $S_{defect}$ (z < 4) represents the adatoms or edge atoms with even lower atomic CNs. The intensities of the components are subject to the fraction of the specifically z-coordinated atoms and the energy values of the peaks satisfy the criterion: $\Delta E_v(\Delta_H) : \Delta E_v(\infty) = E_i : E_b = c_i^{-m}$. For a surface, the peak energies of the components may fluctuate slightly with varying experimental conditions such as temperature, crystal orientation, and incident radiation beam angle.[64]

From the above discussions, we can establish the rules for decomposing the spectrum of surface core-level shift:

1. There should be components representing the *B*, $S_2$, $S_1$ and $S_{defect}$.

2. The energy shift should be positive and the low-z component shifts further.
3. The energy shift of each component is proportional to the magnitude of bond energy, which follow this relationship: $\Delta E_v(\Delta_H):\Delta E_v(\infty)=E_i:E_b=c_i^{-m}$.
4. The resultant intensity of the components is constrained by the measured spectral intensity. The width and intensity of each component in the initial decomposition[58, 59] for the particular Rh and Pd examples were taken as references for fine tuning under constraint.
5. The neighboring Rh($5s^1 4d^8$) and Pd($4d^{10}$) noble metals in the Periodic table share the same *fcc* structure; the effective CNs of the Rh and Pd surfaces of the same orientation should be identical. This adds another constraint for atomic CN refinement.
6. If a total of $l$ components are involved in decomposing a set of XPS spectra from the different orientations of the same specimen, the $E_v(1)$ should take the mean value of $N=C_l^2=\frac{l!}{[l-2]!2!]}$ possible combinations with a standard deviation $\sigma$. The minimal standard deviation serves as a criterion for the accuracy of spectral decomposition.

With the above constraints, we are able to determine the atomic-layer and crystal-orientation resolved effective CN, local strain, quantum trap depth, the 3d energy level of an isolated Pd and Rh atom and their bulk shift, as well as the ratio of BE density and the atomic cohesive energy, which are beyond the scope of available methods. However, the combination of BOLS and tight binding theory is unable to

determine the absolute intensity and width of each component as they are more dependent on experimental conditions.

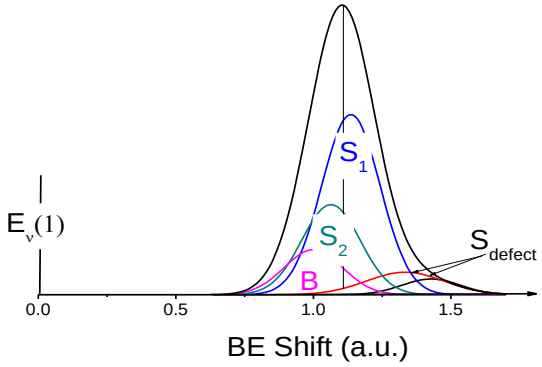


Figure 6 Illustration of the XPS spectrum. $E_v(1)$ is the energy level of an isolated atom, which is the reference for the shifts of other components that follows these constraints: (1) there should be components representing the B, $S_2$, $S_1$ and $S_{defect}$; (2) the energy shift should be positive and the low-z components shift further; (3) the energy shift of each component is proportional to the magnitude of bond energy, which follows this relation: $\Delta E_v(\Delta_H) : \Delta E_v(\infty) = E_i : E_b = c_i^{-m}$.

Figure 7 and Figure 8 showed the measured $3d_{5/2}$ spectra from the (111), (100) and (110) planes of clean Pd and Rh surfaces[58] [59] and the decomposition spectra in the mode of Gaussian based on BOLS correlation. The Pd $3d_{5/2}$ spectra demonstrate one major peak that is symmetrical after background subtraction. However, the Rh $3d_{5/2}$ spectra exhibit two major peaks. The asymmetry at the lower energy end may correspond to the presence of defects in comparison to those of Pd. The XPS spectral pattern difference between Pd and Rh may arise from the electronic configurations Pd ($4d^{10}5s^0$) and Rh ($4d^85s^1$). In order to do decomposition, all the spectra were normalized by their corresponding intensity maximum. According to the constraints given, each spectrum was decomposed with three components,

representing the B, $S_2$, and $S_1$ components from higher to lower BE. The decomposition was conducted by choosing $z_1 = 4$ and $z_2 = 6$ and $z_3 = 12$ for the (100) surface as reference standard and allowing slight deviation of the (111) and (100) surfaces for the best fit. For each element, the B energy and $E_{3d}(1)$ remain unchanged for all the surfaces. The optimal component energies and the decomposition parameters of the XPS $3d_{5/2}$ BE shift of Rh and Pd surfaces after the subtraction background are summarized in Table 1. The three decomposition Gaussian components, denoted as $S_1$, $S_2$ and $B$, satisfy the BOLS expectation. The refinement of the orientation-resolved effective coordination numbers arises from the atomic density of each face. Results show the slight anisotropy of lattice strain in the three orientations.

From the decomposition, we obtained the $E_v(1)$ and $\Delta E_v(i)$ values. It is general that the intensity of the B component is higher than other components in the same spectrum and that the intensity of B component is the highest in the (111) surface of the same material under the same experimental environment. It has been derived that the BE for an isolated Rh atom is 302.50 eV and for Pd atom it is 330.63 eV with their respective bulk shifts of 3.95 and 3.99 eV. The refinement leads to the effective atomic CNs of the top (100), (110), and (111) atomic layers as 4.00, 3.66, and 4.04. Results indicate that BE of electrons in the top layer is the highest in general compared to electrons in the inner layers, which agrees with what discovered by Matsui et al.[40] from Ni surface. Among the three surfaces, the electronic BE of the

(110) surface is higher than the (100) and (111) surfaces because of their difference in the effective CNs.

The derived Pd $\Delta E_{3d_{5/2}}(\infty)$ value of 3.99 eV also agrees with the value of 3.98 eV derived from the reproduction of the size dependence of the Pd $3d_{5/2}$ BE shift, which evidences that the both surface and nanosolids induced positive BE shift arise from the coordinated quantum trapping. The calculations lead to the coordination-resolved BE shift ($\nu = 3d_{5/2}$) for Rh and Pd:

$$E_v(i) = E_v(1) + \Delta E_v(\infty)c_z^{-1} = \begin{cases} 302.50 + 3.95c_z^{-1} \\ 330.63 + 3.99c_z^{-1} \end{cases}$$

Theses fundamental information should be useful to the understanding of the surface behavior of these surfaces such as their catalytic performance.

In conclusion, we could gain from the above discuss:

1. Extraction of quantitative information regarding the energy levels of an isolated atom and its bulk shift from the measure spectra. For the particular cases, the $3d_{5/2}$ energy levels of the isolated Rh(302.50 eV) and Pd(330.63 eV) atoms and their respective bulk shifts (3.95 and 3.99 eV) have been determined. The values for Pd surfaces coincide well with what derived from the reproduction of size dependent BE shift.
2. Refinement of the effective atomic coordination numbers of the top *fcc*(100), (110), and (111) atomic layers as 4.00, 3.66, and 4.04 for both Pd and Rh, which is expected hold globally true for other fcc structures.

3. It is further confirmed that bonds between under-coordinated atoms become shorter and stronger, which induces local strain and the skin-depth charge and energy quantum trapping and hence derives the global positive energy shifts that will happen to other situations where under-coordinated atoms dominate.

Table 1 Decomposition parameters of the XPS $3d_{5/2}$ core level shift of Rh and Pd surfaces after the Tougaard background is subtracted. The three decomposition Gaussian components, denoted as $S_1$, $S_2$ and $B$, satisfy the BOLS expectation.

| Refs [58, 59] | $S_1$ | | $S_2$ | | $B$ | | $z_1$ | $1\text{-}c_i$ | $z_2$ | $1\text{-}c_2$ |
|---|---|---|---|---|---|---|---|---|---|---|
| | BE | I | BE | I | BE | I | | | | |
| Pd(111） | 335.18 | 0.27 | 334.88 | 0.30 | | 0.60 | 4.03 | 0.123 | 6.06 | 0.061 |
| （100） | 335.24 | 0.34 | 334.94 | 0.41 | 334.62 | 0.55 | 4 | 0.124 | 6 | 0.062 |
| （110） | 335.28 | 0.35 | 334.98 | 0.45 | | 0.50 | 3.65 | 0.142 | 5.15 | 0.083 |
| Rh(111) | 307.08 | 0.57 | 306.79 | 0.08 | | 0.84 | 4.05 | 0.122 | 6.03 | 0.062 |
| (100) | 307.15 | 0.91 | 306.85 | 0.10 | 306.53 | 0.65 | 4 | 0.124 | 6 | 0.062 |
| (110) | 307.18 | 0.77 | 306.89 | 0.25 | | 0.40 | 3.67 | 0.141 | 5.13 | 0.084 |

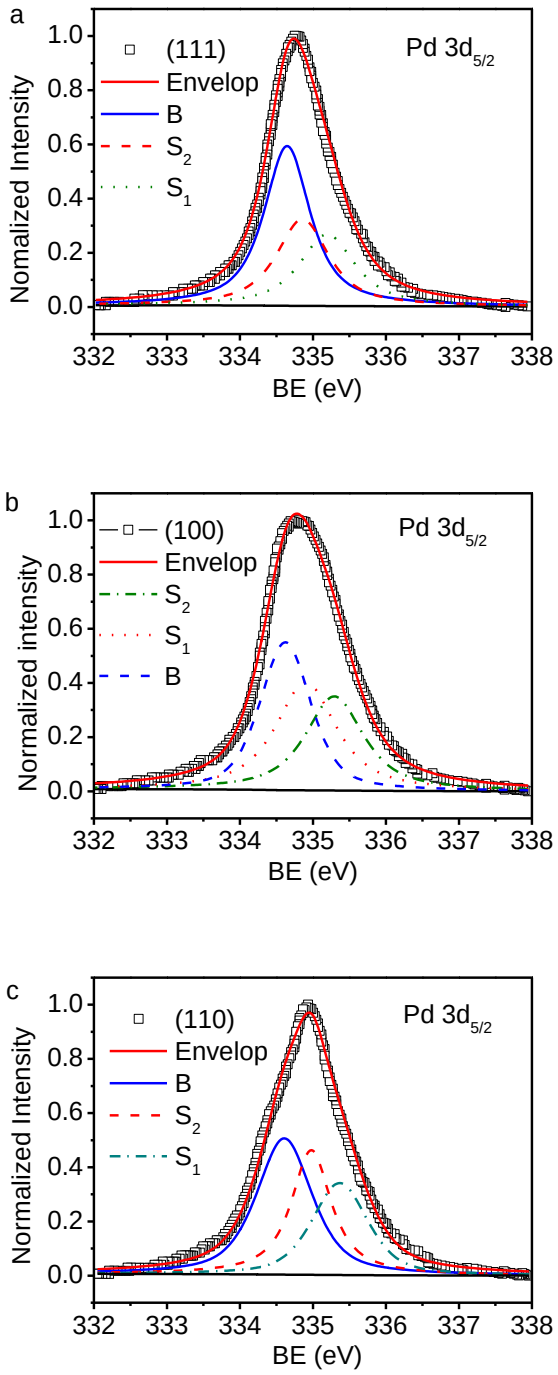


Figure 7 Decompositions of Pd $3d_{5/2}$ core level spectra for (a) (111), (b) (100) and (c) (110) surfaces with three decomposition Gaussian components $S_1$, $S_2$ and $B$ with parameters given in Table 1. The XPS spectra were collected with incident beam energy of 380 eV at normal emission.

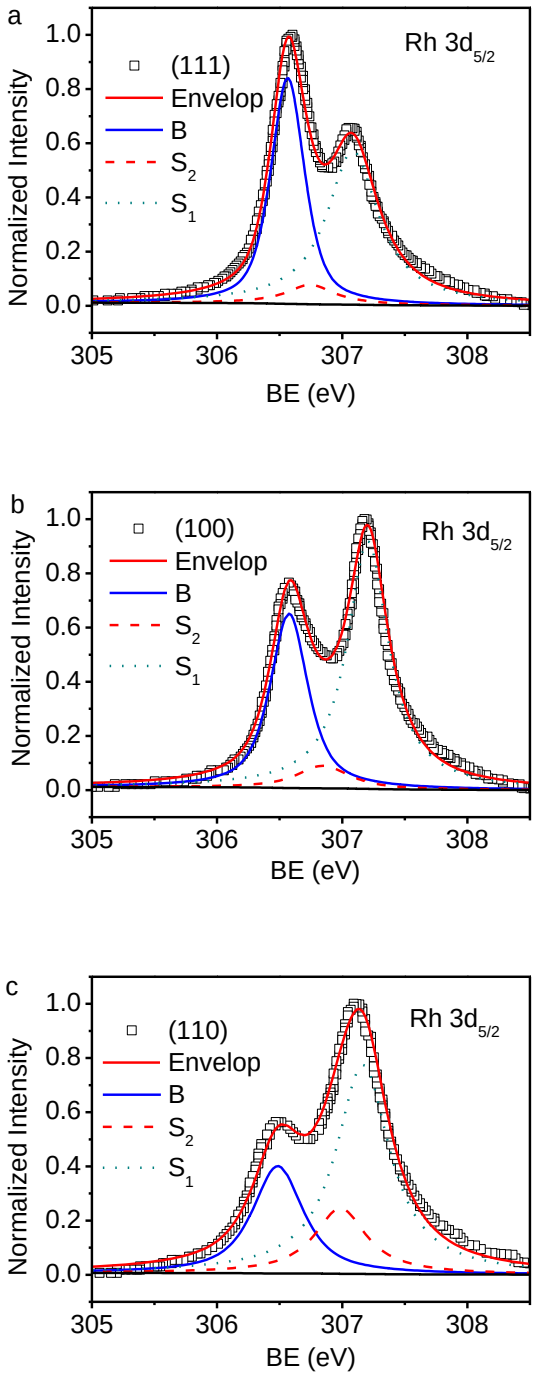


Figure 8 Decompositions of Rh $3d_{5/2}$ core level spectra[59] for (a) (111), (b)(100), and (c)(110) with decomposition parameters given in Table 1. The XPS spectra were collected with incident beam energy of 380 eV at normal emission.

## 3.3 *Bcc* structured W surfaces

The SCLS of W(100), (110), and (111) surfaces[22, 65-67] and their (320) and (540) vicinal[68, 69] have been well measured using different techniques such as the synchrotron and XPS with unfortunately discrepancy on the assignment of the direction of the energy shifts and the energy of the bulk component.[22, 67, 68, 70] A negative shift was assigned with the bulk component at 31.4 eV and the surface component at 31.1 eV. Much more information regarding the interatomic BE and the effect of undercoordination is supposed to be given by the sophisticated measurements.

The XPS measurements for *bcc* metal W(100), (110) and (111) surfaces have been performed as shown in reference.[67, 70, 71] Based on accurate experimental data and BOLS correlation, we re-decompose the XPS spectra of three well-faceted surfaces with respect to the reported best fits[72] using three components, the bulk, B, the second and the first surface layer, $S_2$ and $S_1$. Experimental conditions such as the incident beam energy and the emission angle may change the spectral appearance because of the different inelastic mean free path of photoelectrons due to different kinetic energy and different surface thickness of sample for variation of take-off angles. A spectrum collected at larger emission angles or with lower incident beam energy collect information dominated by the shallow surface, otherwise more bulk information. Varying measurement conditions can never change the intrinsic properties of the surfaces such as the atomic coordination numbers of the surface and

sub-surfaces that are the key factors use herewith. The order of the B, $S_2$, and $S_1$ components and the separation between them follow the constraint given in Eq.21 and 22. The decomposed z-resolved components of the W(100), W(110), and W(111) $4f_{7/2}$ spectra in Figure 9 show that the atomic CN reduction leads to the positive CLS. The CNs of the $S_1$ and the $S_2$ components across the three surfaces vary slightly because of the anisotropy of crystal structure and atomic density. Decomposition of the three surfaces aims to enhance the accuracy in determining the $E_{4f_{7/2}}(1)$ and the $\Delta E_{4f_{7/2}}(\infty)$ by minimizing the standard deviation value of σ. Form the BOLS-TB enabled decomposition, we derived the following information: (i) the W 4f energy level of $E_{4f_{7/2}}(1) = 28.910 \pm 0.006$ eV for an isolated W atom and its bulk shift of $\Delta E_{4f_{7/2}}(\infty) = 2.173$ eV; (ii) an analytical expression for the *z*-resolved CLS: $E_{4f_{7/2}}(z) = 28.910 \pm 0.006 + 2.173$ eV for the under-coordinated edge and adatoms, detailed information for spectra decomposition is listed in Table 2.

As the detectable quantities can be directly connected to the binding identities such as bond nature, order, length, and strength,[73] we are able to predict coordination dependence of the relative BE density, $E_d(z) = E_i(z)/d_i^3$, and the relative cohesive energy per atom, $E_c(z) = z_i E_i(z)$, in each atomic layers,[74, 75]

$$\begin{cases} \dfrac{E_d(z)}{E_d(\infty)} = c_i(z)^{-4} \\ \dfrac{E_c(z)}{E_c(\infty)} = z_{ib} c_i(z)^{-1} \end{cases}$$

With $z_{ib}$ = z/12. The BE density and the atomic cohesive energy are related to the local elastic modulus [74] and the local melting point [75] at the specific atomic site, respectively. the effective atomic CN of the sublayers of different orientations and their derivatives on the local bond strain, local bond energy, the ratio of BE density and the atomic cohesive energy to the respective bulk values, as summarized in Table 2. More details regarding the interdependence of various physical and chemical properties have formed the subjects of recent thematic reports.[57, 73]

In conclusion, the BOLS-TB enabled XPS decomposition of the W(100), (110) ,and (111) surfaces has led to quantitative information about the 4f energy level of an isolated W atom as 28.910 eV and its bulk shift of 2.173 eV. The positive core-level shift originates from the stronger and shorter bonds between under-coordinated atoms, which follow the prediction of Goldschmidt-Pauling rule of bond contraction and the theory of BOLS correlation. The spectra decomposition provides profound information about the effective atomic CN, local bond strain, bond energy, BE density and the atomic cohesive energy in the surface skin up to two atomic layers of different orientations.

Table 2 BOLS elucidated information regarding the atomic-layer ($S_1$, $S_2$) and crystal-orientation resolved effective CN ($z$), local strain ($C_z$-1), the relative BE density ($C_z^{-4}$) and atomic cohesive energy ($z_{ib}C_z^{-1}$) from the measured XPS W 4f SCLS. The $z_{ib} = z_i/z_b$ is the relative coordination number.

| | i | $E_{4f}$(i) (eV) | z | $c_z$-1 (%) | E-density $[C_z^{-4}]$ | $\Delta E_C(i)/E_C(B)$ $[z_{ib}C_z^{-1}-1]$(%) |
|---|---|---|---|---|---|---|
| W | B | 31.083 | 12 | 0 | 1 | 0 |
| W(100)[71] | $S_2$ | 31.283 | 5.161 | -8.26 | 1.41 | -53.12 |
| | $S_1$ | 31.398 | 3.970 | -12.57 | 1.71 | -62.16 |
| W(110)[68] | $S_2$ | 31.240 | 5.829 | -6.61 | 1.31 | -47.99 |
| | $S_1$ | 31.402 | 3.942 | -12.71 | 1.72 | -62.36 |
| W(111)[67] | $S_2$ | 31.275 | 5.270 | -7.96 | 1.39 | -52.28 |
| | $S_1$ | 31.370 | 4.195 | -11.58 | 1.64 | -60.46 |

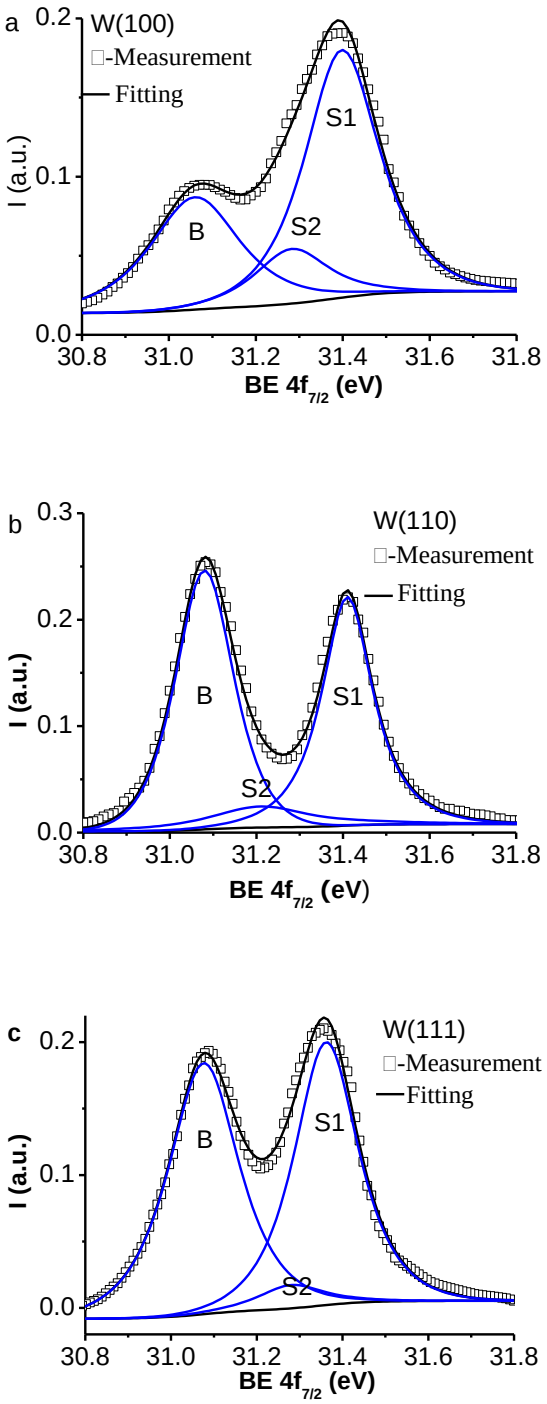


Figure 9 Decomposition of the XPS $4f_{7/2}$ spectra of (a) W(100),[71] (b) (110),[68] and (c) (111)[67] surfaces using the B, $S_2$ and $S_1$ components with the derived 4f level of an isolated W atom as $E_{4f}(0)$ = 28.910 ±0.006 eV and its shift upon bulk formation, $\Delta E_{4f}(12)$ = 2.173 eV, both of which are intrinsic constants changing with neither the experimental conditions nor the crystal orientations.

# 3.4 Hcp structured Ru, Be and Re surfaces

## 3.4.1 Be(0001), (11$\bar{2}$0), and (10$\bar{1}$0) surfaces

The BE shift of 1s peak on the Be(0001), (11$\bar{2}$0), and (10$\bar{1}$0) surfaces has been intensively investigated experimentally using XPS and theoretically based on density functional premise and in terms of the "initial-final states" convention in past decades. [76-83] Using synchrotron radiation, Johansson et al.[77, 79, 83] measured the Be(0001) surface 1s BE shift and identified three distinct components of shifts with energies of -825±30($S_1$), -570±25($S_2$), and -265±20($S_3$) meV with respect to the low energy (large absolute value) component at 111.835(B) eV. For the Be(10$\bar{1}$0) surface, three components were identified to shift by -700($S_1$), -500($S_2$) and -220($S_3$) meV[77, 78, 80, 83] but two components would suffice for the (11$\bar{2}$0) surface. These CLS were assigned as negative shifts according to the "initial-final states" convention, i.e., the surface layers add states at energies higher (smaller absolute values) than the bulk component. This assignment is in contrast with the mixed shift proposed by Hofmann et al.[84] who suggested that the largest negative shift is caused by the second surface layer, instead. Disregarding the discrepancy regarding the number and the order of the surface components, Johansson et al.[77-79] reported that the intensities of the high-energy (surface) components increase with the incident beam energy from 123 to 165 eV. The intensities of the high-energy components also increases when the emission angle (between the photoelectron beam and the surface normal) was reduced

from 36° to 0°.[85] Higher beam energy or smaller emission angles means that the incident beam can penetrate deeper into the bulk and therefore collect more bulk information.[64] From this perspective, the higher energy component corresponds to the B component, instead.

In this section, using the combination of the tight binding approximation and BOLS correlation,[57] Based on previous literatures, we have re-analyzed the XPS spectra for Be(0001),[77, 79, 82] Be($10\bar{1}0$),[77, 80, 83] and Be($11\bar{2}0$)[78, 82] surfaces.[46, 47] We have been able to derive quantitative information from measurements regarding: (i) the energy level of an isolated Be atom and its bulk; (ii) the layer and orientation resolved local strain and quantum trap depression and, (iii) the relative BE density and the relative atomic cohesive energy at the surfaces.

Given an XPS profile with clearly identified $E_v(i)$ and $E_v(B)$ components of a surface ($i$ = 1, 2, …), one can calculate easily the atomic $E_v(1)$ and the bulk $\Delta E_v$ (B) with the relations derived from Eq.. If a total of $l$ components are used to decompose a set of XPS spectra from different surfaces of a specimen, the $E_v(1)$ should take the mean value of the $N = C_l^2 = \frac{l!}{(l-2)!2!}$ possible combinations with a standard deviation $\sigma$. The minimal standard deviation may serve as a criterion for the accuracy of spectral decomposition which involves the peak energies and the corresponding effective CNs. The intrinsic $E_v(1)$ and $\Delta E_v(\infty)$ values should not be affected by experimental conditions, chemical reactions, crystal size or orientation, or surface relaxation. However, crystal orientation may lead to a fluctuation of the

component peak energies and the number of the components because of the slight difference in the effective atomic CNs. Accuracy of the determination is subject strictly to the XPS data calibration.

Based on the criteria established in BOLS correlation, we fit the XPS spectra with respect to the energy shifts given by Johansson et al.[77, 79, 83, 85] for Be, as listed in Table 3. For Be(0001), the initial four components are sufficient. An addition of $S_1$ component in the lower end of the spectrum is needed to represent the under-coordinated Be atom in the outermost Be($10\bar{1}0$) layer.

We need to point out that the quantities of $E_v(1)$ and $\Delta E_v(\infty)$ are intrinsic constant values for a given material disregarding the orientations. Therefore, we can refer the energy shifts of all surface components to the $\Delta E_v(\infty)$ before knowing the $E_v(1)$. According to the tight binding and BOLS theory, the positive shift is preferred. The given energy shifts enable us to determine the effective atomic CN as the unique variable in the present exercise for each component and the $E_v(1)$ using Eq.21. It is emphasized that the effective CN is different from the apparent CN.[57] Incorporating the BOLS correlation mechanism into the measured surface relaxations,[61, 62] the effective CN for the fcc(001) outermost surface is four instead of six.

Figure 10 shows the XPS decomposition of the Be($10\bar{1}0$), (0001), and ($11\bar{2}0$) surfaces. The Intensities of the atomic-layer and crystal-orientation resolved components change also with the incident beam energy. Including the B component

that was counted only once, there are a total of $l$ = 12 components for the considered Be surfaces, as shown in Table 3. There will be a combination of $C_{12}^{2} = \frac{12!}{(12-2)!2!} = 66 = j$ values of $E_v(1)$. Using the least- root-mean-square approach, we can find the average of $< E_v(1) >= \sum_j E_v(1)/j$ and the standard deviation, $\sigma = \{\sum_j (E_v(1) - < E_v(1) >)^2/(j(j-1))\}^{1/2}$. A fine tuning of the CN values will minimize the $\sigma$ value and hence improve the accuracy of the effective CNs, the local strain, the BE density and the cohesive energy per discrete atom in differently oriented surface layers.

According to the decomposition criteria, the B component must exist in all the surfaces. The invisibility of the B component in Be(0001) surface spectrum indicates that the high-mass density of the low-index Be(0001) surface prevents the incident beam from penetrating into the bulk underneath four atomic layers. The fitting indicates that the Be surface skin is formed by at most four surface atomic layers because of the lower atomic cross section and the packing density. For Ni surface [40] and a 3.5 nm sized gold cluster,[53] the surface is only two interatomic spacing thick. The lacking of bulk information in the Be(0001) spectrum also indicates attenuation length of photoelectrons under the 135 eV x-ray beams limiting to the outermost three atomic layers.

The optimal $\sigma$ value is 0.0042~0.0040. The derived $E_{1s}(B = \infty)$ 106.416±0.004 eV and the bulk shift is $\Delta E_{1s}(B = \infty)$ = 4.694 eV with three decimal being suffice with respect to the measurement precision. The derived effective CNs,

the local strains, and the predicted trends of the local BE density and the atomic cohesive energy are given in Table 3. The derived bond contraction is in consistence with the recent findings[53] using a combination of the molecular dynamics calculations, Pauling's correlation, and the coherent electron diffraction revealed that the Au individual nanoparticles of 3.5 nm in diameter demonstrate inhomogeneous relaxations occurring at the outermost two atomic layers. The undercoordination-induced bond contraction involves large out-of-plane bond length contractions for the edge atoms (~0.02 nm, ~7%); a significant contraction (~0.013 nm, 4.5%) for (100) surface atoms; and a much smaller contraction (~0.005 nm, 2%) for atoms in the middle of the (111) facets. In the current system the maximal contraction is around 19%, a value between the theory prediction [86, 87] for Be($10\bar{1}0$) and the measurement of Au.[53]

The spectra decompositions here show that the positive core-level shift assignment is more proper than the assignment of negative or the mixed shift and hence the criteria established herewith is essentially true. The positive shift assignment allows us to derive the energy level of an isolated atom and its bulk shift. The derived fundamental factors are of great importance in determining the surface properties and surface processes.

Furthermore, the experimentally observed incident beam energy and emission angle trends [78, 79, 83, 85] evidence the assignment of surface positive CLS, as the higher incident beam energies or at smaller emission angles collect more information

from the bulk than from the surface.[64, 88] Speranza and Minati [88] reported that increasing the angle between the surface normal of graphite and the emission beam from 0 to 85°, the detected depth profile decreases from 8.7 to 0.8 nm.

In conclusion, we have systematically analyzed the Be 1s energy shift of Be (0001), $(10\bar{1}0)$, and $(11\bar{2}0)$ surfaces from the perspective of bond-potential-band correlation with elucidated information of: (i) the BE of an isolated Be atom; (ii) the bulk shift of Be 1s; (iii) the effective atomic CNs and the corresponding local strains, and, (iv) prediction of the trends of coordination resolved BE density and cohesive energy per discrete atom in the surface of skin depth. The developed approach enhances the power of the conventional XPS technique for more quantitative information regarding the surface process and properties. The concept of local strain and quantum trapping may be essential for understanding the bonding and electronic behavior in the surface and atomic defect sites.

Table 3 Atomic-layer and crystal-orientation resolved effective CN(z), local strain (c(z)-1), relative BE density ($c(z)^{-4}$), and the relative atomic cohesive energy ($z_{ib}/c(z)$ with $z_{ib} = z/12$) determined from the measured XPS profiles of Be(0001), $(10\bar{1}0)$, and $(11\bar{2}0)$ surfaces under the established approach and the criteria.

| | i | $E_{1s}$(i) (eV) | z | c(z)-1 (%) | $c(z)^{-4}$ | $z_{ib}/c(z)$ |
|---|---|---|---|---|---|---|
| Be | B(z=12) | 111.110 | 12 | 0.00 | 1.00 | 1.00 |
| $(10\bar{1}0)$ Refs [[77, 83]] | $S_4$ | 111.330 | 7.00 | -4.46 | 1.20 | 0.61 |
| | $S_3$ | 111.590 | 4.83 | -9.25 | 1.47 | 0.44 |
| | $S_2$ | 111.830 | 3.83 | -13.25 | 1.77 | 0.37 |
| | $S_1$ | 112.122 | 3.10 | -17.75 | 2.19 | 0.31 |
| (0001) Refs [[79, 85]] | $S_3$ | 111.370 | 6.53 | -5.23 | 1.24 | 0.57 |
| | $S_2$ | 111.680 | 4.39 | -10.79 | 1.58 | 0.41 |
| | $S_1$ | 111.945 | 3.50 | -15.06 | 1.92 | 0.34 |
| $(11\bar{2}0)$ Ref [[78]] | $S_4$ | 111.400 | 6.22 | -5.80 | 1.27 | 0.55 |
| | $S_3$ | 111.650 | 4.53 | -10.29 | 1.54 | 0.42 |
| | $S_2$ | 111.870 | 3.71 | -13.90 | 1.82 | 0.36 |
| | $S_1$ | 112.190 | 2.98 | -18.71 | 2.29 | 0.31 |

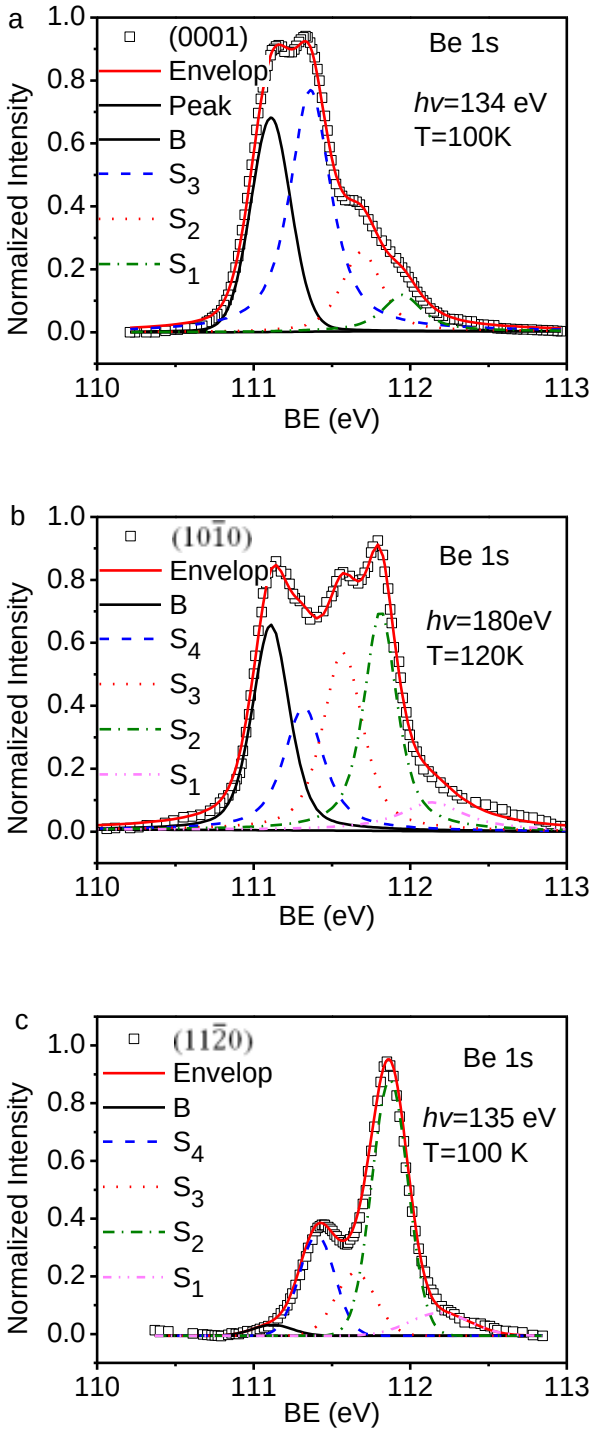


Figure 10 The decomposed XPS spectra for the Be(0001), (10$\bar{1}$0), and (11$\bar{2}$0) surfaces The 1s core level of 106.416 ±0.004 eV and the B component at 111.11 eV should be identical for all the surfaces of the same material.

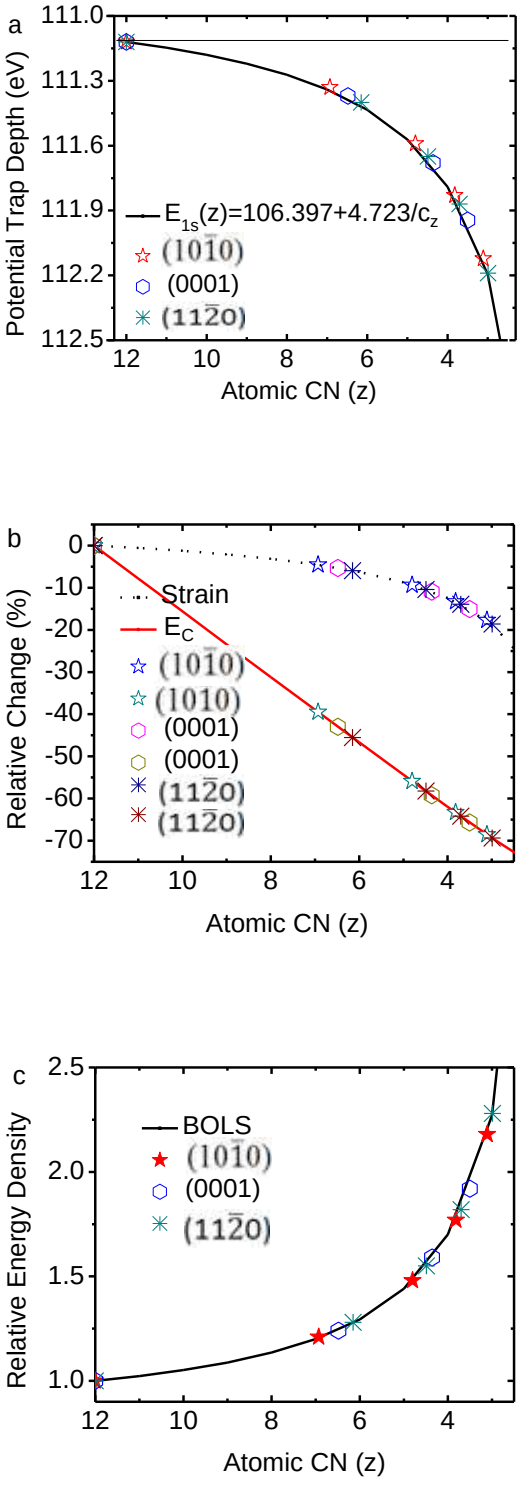


Figure 11 Comparison of the BOLS prediction with the derived CN(layer)-and orientation- resolved (a) bond strain and the relative change of atomic cohesive energy ($E_C$); (b) potential trap depth and, (c) the relative energy density.

### 3.4.2 Ru(0001) and (10$\bar{1}$0) Surfaces

The XPS spectra of Ru(0001) and Ru(10$\bar{1}$0) surface were collected by the same group of Lizzit[89] and Baraldi[90-92] using the super ESCA beamline of the ELETTRA synchrotron facility in Trieste, Italy. The experiments were carried out at 130~270 K and an emission angles of 40° with an incident beam energy of 352~400 eV. The verification of experimental conditions just affects the overall intensity of the convoluted spectrum but not the energy position or width of each component. They also decomposed the spectra. The number, peak width, and energy of components they optimized for each spectrum provide references for the current optimization and information extraction.

Based on the developed approaches, we decode the XPS spectra by using Gaussian components with the constraint of Eq.21 on the correlation between the component energies. The z values for the Ru surfaces are the initial input in optimization. In order to ensure the minimal value of $\sigma$, fine tuning of the z-values was performed in the spectrum decomposition. The optimal results are shown in Table 4. The presently optimized z values for all the sublayers are identical to those derived from the same *hcp* surfaces of Be(0001), (10$\bar{1}$0), and (11$\bar{2}$0).[48] The well-defined BE shifts of Be surfaces allowed such z-value optimization,[77-79, 85] which was used as references for the current iteration. The consistency of the effective CN for both the hcp Be and Ru surfaces amplify the reliability of this approach in determining the effective CN for the surface layers.

One needs to note that the $E_v(1)$ and $E_v(B=\infty)$ are intrinsic constants, which are identical for all the surfaces and subsurfaces of a given material disregarding their orientations. For simplicity, we refer the energy shift of all surface components to the $E_v(B)$ before knowing the $E_v(1)$ value. Including the B component, there are a total of $l$ = 8 components involved for the Ru(0001) and Ru(10$\bar{1}$0) surfaces, as shown in Figure 12. There is a combination of $C_8^2 = \frac{8!}{(8-2)!2!} = 28$ $E_{3d}(1)$ values. Using the least- mean- root-square approach, we found the average $< E_{3d}(1) >= \sum_{28} E_{3d}(1)/28$ = 275.883 eV with a standard deviation, $\sigma = \{\sum_{28}(E_v(1) - < E_v(1) >)^2/(28(28-1))\}^{1/2}$ =0.0018~0.002 eV. The bulk shift $\Delta E_{3d}(B=\infty)$ = 3.661 eV and the optimized $E_{3d}(\infty)$ = 2795.544±0.002 eV were thus obtained. The derived effective CNs, the local strains, and the predicted trends of the local BE density gain and the atomic cohesive energy remnant are summarized in Table 4, and plotted in Figure 13.

In conclusion, the current derivatives favor more the mechanism of surface interlayer relaxation[61, 62] than the "final-initial states" model; the latter considered no perturbation in that Hamiltonian that should dominate, instead. The photovoltaic effect and the excited final states may add artifacts to the XPS spectrum that could be removed by proper calibration in the measurement.[64] The CN-imperfection induced bond strain and bond energy gain act on the core electrons at the energy levels of an atom whether it is in the neutral initial or the ionized final state. Therefore, joining the effect of CN-imperfection into the 'initial-final states' model may make the modeling

more comprehensive. Nevertheless, the developed approach has enabled us to elucidate quantitative information of the core-level position of an isolated atom and its shift due to bulk formation, as well as the quantitative information regarding the atomic-layer and crystal-orientation resolved effective atomic CN, local strain, BE density, and atomic cohesive energy, which is beyond the scope of conventional approach using an XPS or other techniques.

## 3.5 Conclusion

In chapter 3, surface atomic layers or orientation induced BE shift have been investigated using the combination of BOLS correlation and XPS measurements. The well XPS decomposition of single crystal surface including *fcc* metal Pd and Rh, *bcc* metal W and *hcp* metal Be and Ru have confirmed the BOLS prediction that the undercordinated atoms on the surface region induce bond contraction and bond energy enhancement, consequently, the BE of electrons of under-coordinated atoms shifts to high value. The BE of an isolated corresponding atom and intrinsic bulk shift have been calculated, which gives a constant reference for the energy level evolution.

Table 4 Summary of the BOLS elucidated information regarding the atomic-layer and crystal-orientation resolved effective CN ($z_i$), local strain ($c_i$-1), the ratio of BE density ($c_i^{-4}$) and atomic cohesive energy ($z_{ib}c_i^{-1}$) derived from the measured XPS profiles of Ru(0001)[89] and Ru($10\bar{1}0$)[90-92].

| | i | $E_{1s}(i)-E_{1s}(B)$ (eV) | $E_{1s}(i)$ (eV) | z | $c_z$-1 (%) | E-density $[c_i^{-4}]$ | $\Delta E_C(i)/E_C(B)$ $(z_{ib}c_i^{-1}-1)(\%)$ |
|---|---|---|---|---|---|---|---|
| Ru | B | 0 | 279.544 | 12.00 | 0.00 | 1.00 | 0.00 |
| Ru($10\bar{1}0$) Refs [[90]] | $S_4$ | 0.175 | 279.719 | 6.93 | -4.57 | 1.21 | -39.48 |
| | $S_3$ | 0.377 | 279.921 | 4.80 | -9.35 | 1.48 | -55.88 |
| | $S_2$ | 0.561 | 280.105 | 3.82 | -13.30 | 1.77 | -63.28 |
| | $S_1$ | 0.785 | 280.329 | 3.11 | -17.68 | 2.18 | -68.52 |
| Ru(0001) Refs [[89]] | $S_3$ | 0.205 | 279.749 | 6.48 | -5.32 | 1.24 | -42.97 |
| | $S_2$ | 0.448 | 279.992 | 4.36 | -10.91 | 1.59 | -59.22 |
| | $S_1$ | 0.649 | 280.193 | 3.50 | -15.06 | 1.92 | -65.66 |

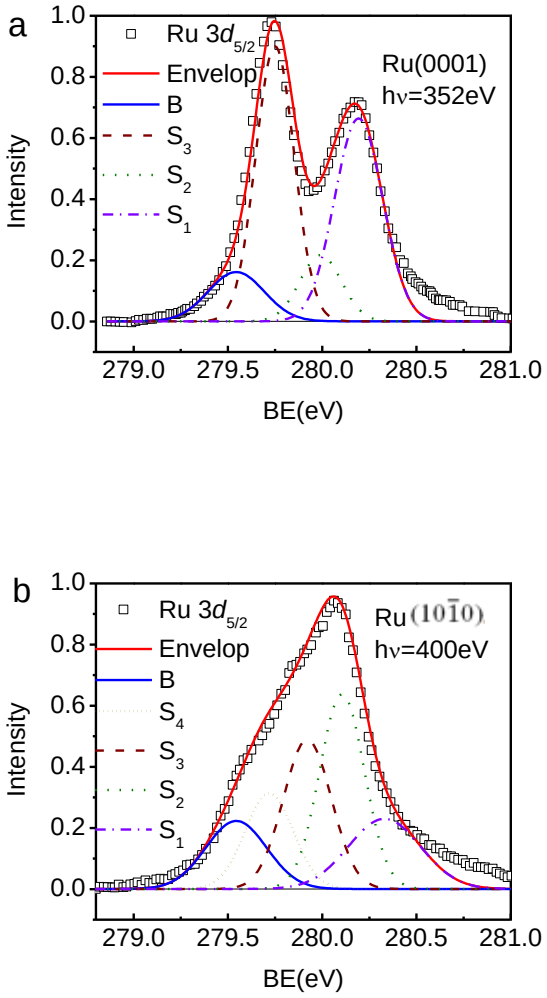


Figure 12 The decomposed XPS spectra for (a) the Ru(0001)[89] and (b) Ru(10$\bar{1}$0)[90-92] surfaces with derived information as summarized in Table 4.

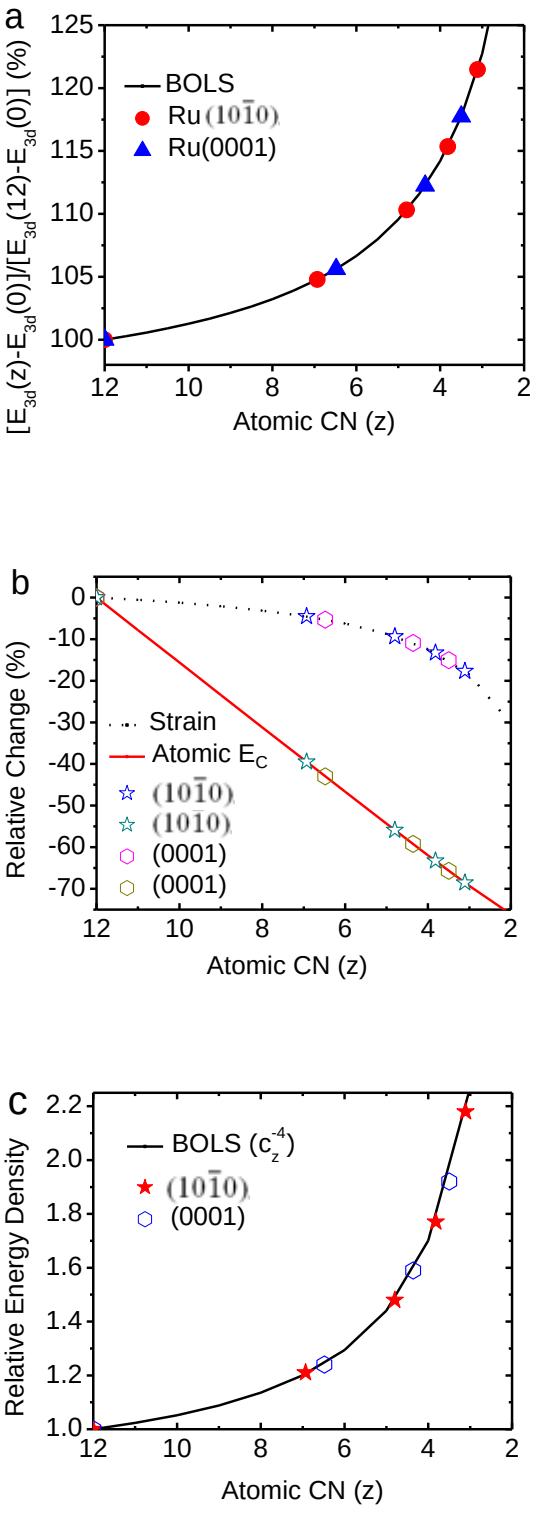


Figure 13 Comparison of the BOLS prediction with the derived CN (layer and orientation) - resolved (a) BE; (b) the relative change of atomic cohesive energy ($E_C$); (c) the relative energy density.

# Chapter 4 BE Evolution on Terrace Edge, Adatoms and Vacancies

## 4.1 Introduction

The primary role of terrace edge as in determining the surface chemical reactivity has been well-established as a result of surface science. For example, it has been found that[93] with the every third row of Au atoms adding to a fully Au covered $TiO_2$ surface could improve the efficiency of CO oxidation at room temperature by a factor of 50 compared with the otherwise fully Au covered surface. In the case of $N_2$ dissociation on Ru(0001) surface, the activation energy is 1.5 eV lower at steps than that on the flat surface, yielding at 500 K an desorption rate that is at least nine orders of magnitude higher on the terraces, as the dissociation is largely influenced by the presence of steps.[94] Similar results have been found for NO decomposition on Ru(0001),[95, 96] $H_2$ dissociation on Si(001),[97] and low-temperature nitridation of nano-patterned Fe surface.[98]

In addition, an adatom concentration of a few percent is sufficient to dominate the overall reaction rate in a catalytic process because the higher reaction rate or the lower activation energies of the under-coordinated atoms. For instances, the first methane dehydrogenation process is highly favorite at the Rh-adatom site on Rh(111) surface with respect to step or terrace sites;[99, 100] adatoms deposited on

oxides can activate the C–H bond scission,[101] the acetylene ciclomerization,[102] and the CO oxidation.[103]

Another relevant contribution determining the chemical reactivity is the surface strain induced by defect or interaction between overlayers and supports. Gsell et al.[104, 105] found preferential oxygen and carbon monoxide adsorption on the stretched regions obtained through subsurface argon implantation on Ru(0001). Wintterlin et al.[106] measured an enhanced NO dissociation probability at the local expanded areas of the Ru(0001) dislocations. In any case, the existence of strain, originated by surface defects or by the interaction with the support, seems to be a general feature of surface catalysts. Obviously, the ability of accepting or donating charge of a catalyst plays a key role in the process of catalytic reaction.[107] The electroaffinity is tunable by the cluster size or defect density through valence charge polarization or quantum trapping.[75] The stress is related to the quantum trapping through interatomic BE variation.

The extremely-high catalytic efficiency of under-coordinated atoms of terrace edge, adatoms and defects is indeed fascinating. For adatoms, the catalytic activity of gold was attributed entirely to the presence of neutral gold adatoms on the gold nanoparticles.[93] These adatoms differ from atoms on bulk gold in three ways that might enhance their catalytic activity:[93] (i) They have fewer nearest-neighbor atoms and *possibly* a special bonding geometry to other gold atoms that creates a more reactive orbital. (ii) They exhibit quantum size effects that *may* alter the

electronic band structure of gold nanoparticles. (iii) They *may* undergo electronic modification by interactions with the underlying oxide that cause partial electron donation to the gold cluster. Therefore, atomic-level understanding of the energetic behavior of electrons of low-dimensional systems is a very important issue in condensed matter science. However, the understanding of the local energetic behavior of electrons in systems with a large number of highly under-coordinated atoms has been still a great challenge.

The objective of this work is to show that incorporating the BOLS correlation[64] into the high-resolution XPS measurements[59, 108] has affirmed the BOLS predictions that the broken bonds induce local strain and charge and energy quantum trapping in addition to electron polarization in under-coordinated system of terrace edge, adatoms and vacancies. Both the trapped and polarized states can be identified by monitoring the evolution of the density-of-states in either the valence or the core band because charge polarization takes place in the valence band but the core charge will be screened. In this report, the electronic structure of terrace edge, adatoms and vacancies have been studied using the combination of XPS measurement and Atomistic photoelectron spectroscopy distillation (APSD) method.

The APSD method is described as follows: The measured XPS spectrum on the terrace edge, adatoms and defects vacancies on a flat surface can be decomposed into component with each component corresponding to a particular value of z, as illustrated in Figure 14. $S_1$, $S_2$, and B are three main peaks. If edge atoms, vacancies

or adatoms present, $A_1$ and $A_2$ will appear at the lower (large absolute value) end of the spectrum. The energy values of the components satisfy the criterion: $\frac{\Delta E_v(z)}{\Delta E_v(B=\infty)} = \frac{E_z}{E_b} = c_i^{-m}$. If polarization occurs, P component presents at the higher end of the spectrum (lower BE). The energy of the P peak satisfies, $\frac{\Delta E_v(P)}{\Delta E_v(B=\infty)} = \gamma < 1$, because of the screening effect of the polarization. The $\gamma$ is the strength ratio of bond energies. The intensities of the components are proportional to the fractions of the specifically z-coordinated atoms. Any core band should demonstrate the fingerprints of both the trapped and the polarized states, if both of T and P states exist, one can imagine what will happen if we subtract the XPS spectrum collected at the smallest emission angle from that collected from the same surface at larger emission angles. We can also differentiate the spectra collected before and after defect generation under the same experimental conditions upon background subtraction and spectral area normalization of both. The residual spectrum keeps only the skin information in the former and the defect in the latter within zones of one or two atomic diameter size. Considering the attenuation length and the take off angle adopted in XPS measurement, the difference spectrum represents only several atomic layers onsite or underneath of the surface, is called atomistic photoelectron spectroscopy distillation. Such a APSD process enables the purification of the desired surface and defect states as the APSD filters out the artifact background and bulk information.

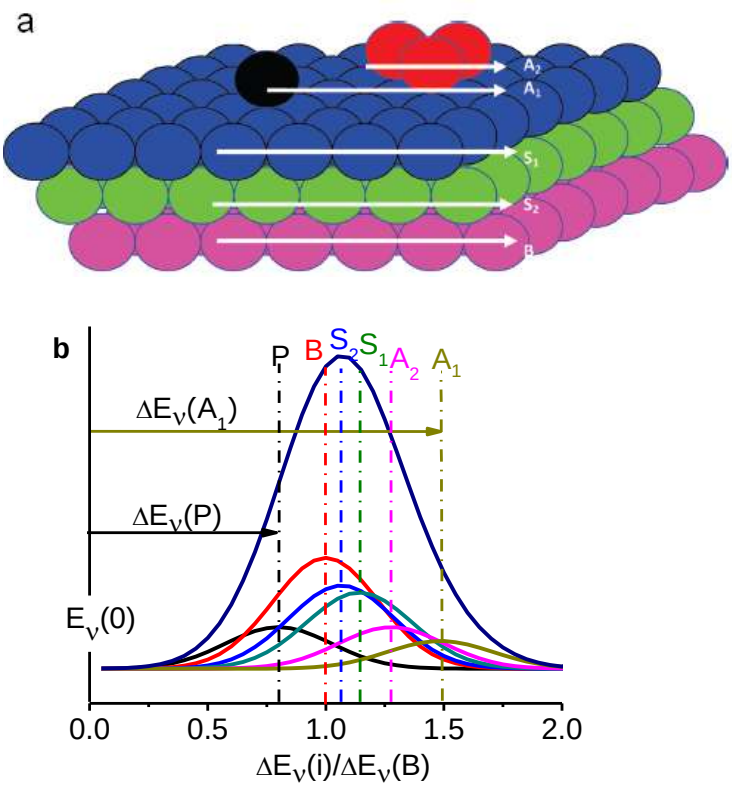


Figure 14 Illustration of the origin for the adatom- and surface-induced core level shift. (a) Atomic arrangement at a surface with irregularly grown adatoms, $A_1$ and $A_2$ with effective CN smaller than 4. $S_1$, $S_2$ and B represent the outmost, the second and the bulk components. P represents the polarization state. (b)**:**In addition to the main peaks of B, $S_2$, $S_1$, there should be A and P components representing the trapped and the polarized states of the under-coordinated adatoms. The energy shift should be positive and the lower-z component shifts further. However, the P states should move oppositely with respect to the A states.

# 4.2 Terrace Edge on Re Surface

## 4.2.1 Introduction

Figure 15 illustrates the atomic arrangement of the *hcp* Re(0001) and the $(12\bar{3}1)$ surfaces. In contrast to the smooth (0001) surface, the $(12\bar{3}1)$ surface is much rougher with high fraction of under-coordinated kink atoms. It is anticipated that these under-coordinated atoms will generate the entrapped states below the bulk component

in the core band. Thanks to the well-measured Re(0001) and (12$\bar{3}$1) surface $4f_{7/2}$ XPS with and without oxygen chemisorptions by Mårtensson et al.[109] and Chan et al.[54] using synchrotron radiation at different emission angles and incident beam energies.

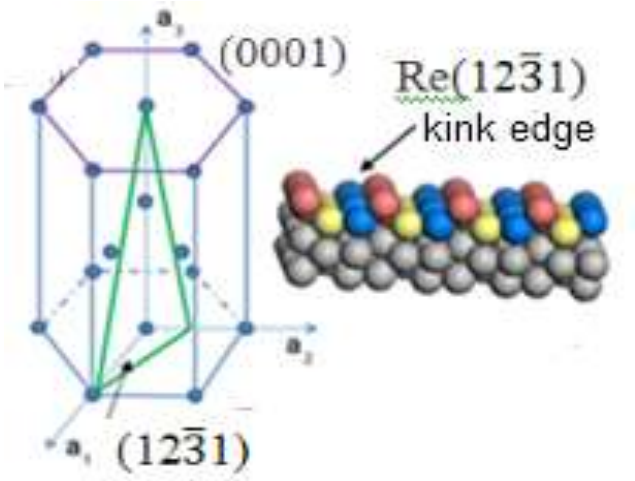


Figure 15 Schematic illustrations of the atomic configurations of the clean Re(0001) and Re(12$\bar{3}$1) surface. The right panel shows the atomic kink edge of the (12$\bar{3}$1) with high fraction of under-coordinated atoms.

From the above discussions in this chapter and introduction in chapter 2, we may establish the rules for decomposing the spectrum of the under-coordinated atom-induced BE shift:

1. In addition to the main peaks of B, $S_2$, $S_1$, there should be A and P components representing the trapped and the polarized states of the under-coordinated adatoms.
2. The energy shift should be positive and the lower-z component shifts further. However, the P states should move oppositely to the A states.

3. The energy shift of each component is proportional to the magnitude of bond energy, which follow this relationship: $\frac{\Delta E_v(z)}{\Delta E_v(B=\infty)} = \frac{E_z}{E_b} = c_i^{-m}(i = A, S_1, S_2)$.

## 4.2.2 Results and Discussions

Following the rule as mentioned, Figure 16 shows the decomposed XPS spectra for the Re (0001) and the Re($12\bar{3}1$) surfaces with the *z* values[46, 48] as input and the derived information as given in Table 5. The (0001) and the ($12\bar{3}1$) surfaces are decomposed into 3 and 4 components, respectively, which is consistent with those for the (0001) and ($11\bar{2}0$) surfaces of Be and Ru (*hcp*).[46, 48] As the intrinsic quantities, the $E_{4f5/2}(1)$ and the $E_{4f5/2}(B = \infty)$ remain constant disregarding the change in the emission angle or the crystal orientation. From the decomposition, it is noted that the undercoordination-induced BE shift is indeed positive and the lowest coordination component shifts most from that of an isolated Re atom. Therefore, choosing the bulk component as the reference point and assigning the shift as negative are improper, which prevents the tabulated information from being extracted.

Including the common B component ($z$ = 12), we have a total of $l$ = 8 components for the two surfaces. Hence, there will be a combination of $C_8^2 = \frac{8!}{(8-2)!2!} = 28 = j$ possible values of $E_v(1)$ derived from Eq.21. Giving rise to the mean $< E_v(1) >= \sum_j E_v(1)/j$ and the standard deviation, $\sigma = \left\{\sum_j (E_v(1) - < E_v(1) >)^2/(j(j-1))\right\}^{1/2}$. Increasing the *l* or the *j* values can ensure the accuracy of the $E_v(1)$ (minimize the standard deviation $\sigma$ value). A fine-tuning of the *z* value

for each component collectively can improve the accuracy of the effective *z* value in the differently oriented surface layers. The optimized *z* value of 2.836 for the outermost $(12\bar{3}1)$ surface layer is lower than the value of 3.506 for the (0001) surface.

Based on the given criteria, the decomposition of the three spectra has led to the z-dependent BE and more information listed in Table 5.

$$E_{\frac{4f5}{2}}(z) =< E_{\frac{4f5}{2}}(1) > \pm\sigma + \left[E_{\frac{4f5}{2}}(B) - E_{\frac{4f5}{2}}(1)\right]$$
$$= 40.015 \pm 0.004 + 2.629\, C_z^{-1}$$

Figure 17a shows the APSD of the Re $(12\bar{3}1)$ $4f_{5/2}$ and $4f_{7/2}$ bands gained by subtracting the spectrum collected at 0° from the one collected at 75° after background subtraction and spectral area normalization. The rule of spectral area conservation almost applies to the APSD, indicating that the background correction and spectral area normalization are quantitatively proper. Obvious valleys and peaks appear in the APSD, which can be assigned without any question to the bulk (B) and the under-coordinated kinks with the quantum entrapment (T). Applying Eq. 21, the T components are dominated by the outermost two atomic layers with the effective z values of 3.6($S_2$) and 2.8($S_1$), as indicated in Figure 17b. The small feature at the upper edge of the 4f7/2 band is contributed from the 5p3/2 band of the kinks.

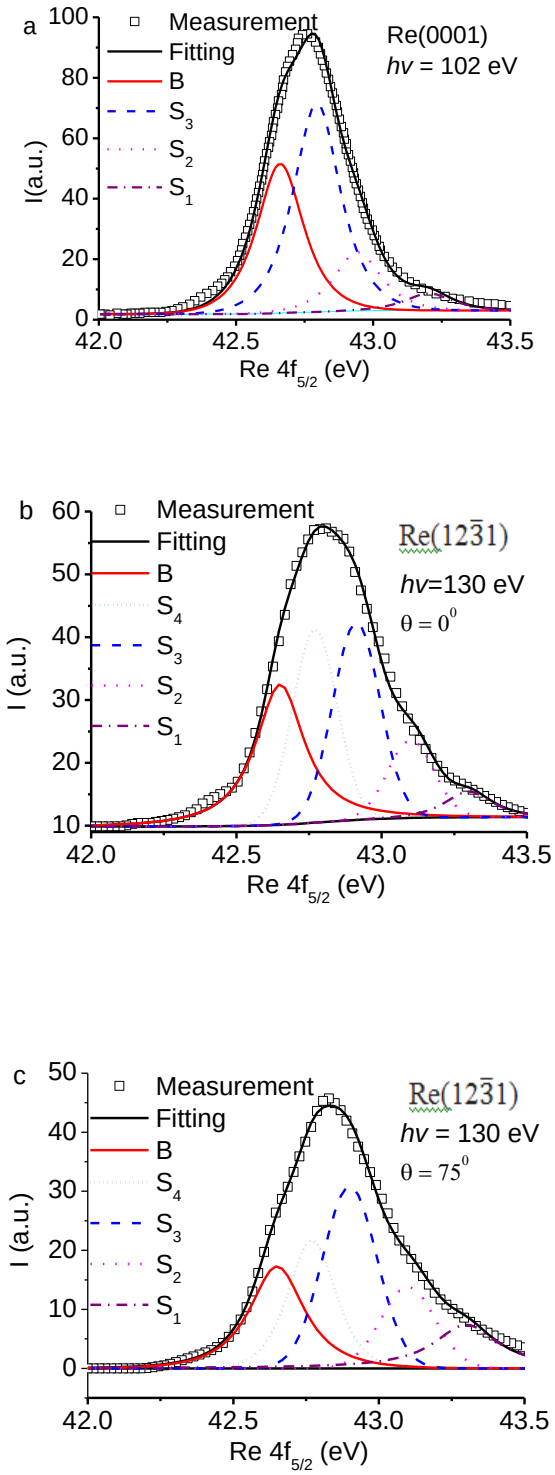


Figure 16 The decomposed XPS Re $4f_{5/2}$ spectra collected from the (a) Re(0001)[109] and the Re(12$\bar{3}$1) [54] surfaces with (b) $0^0$ (along the surface normal) and (c) $75^0$ emission angles. The constant bulk component locates at 42.645 eV. The intensities of the surface ($S_1$ and $S_2$) components increase with the emission angle rendering that of the bulk component.

Table 5 Crystal orientation and atomic layer resolved Re $4f_{5/2}$ shift with derived information of the effective CNs, local strain ($C_z$-1), relative BE density ($C_z^{-4}$), and the relative atomic cohesive energy ($z_{ib}/C_z$ with $z_{ib}$ = z/12) of the Re(0001) and (12$\bar{3}$1) surfaces.

| | *i* | $E_{4f5/2}$(z) | *z* | $C_z$-1 (%) | $C_z^{-4}$ | $z_{ib}/C_z$ | Refs |
|---|---|---|---|---|---|---|---|
| Re atom | 0 | 40.015 | 0 | - | - | - | - |
| Re(0001) | B | 42.645 | 12 | 0 | 1 | 1 | 42.77[110];42.60[109]; |
| | $S_3$ | 42.794 | 6.480 | -5.319 | 1.244 | 0.571 | 42.67[110] |
| | $S_2$ | 42.965 | 4.390 | -10.792 | 1.579 | 0.410 | - |
| | $S_1$ | 43.11 | 3.506 | -15.027 | 1.918 | 0.343 | - |
| Re(12$\bar{3}$1) | $S_4$ | 42.779 | 6.778 | -4.811 | 1.218 | 0.593 | 42.81[54]- |
| | $S_3$ | 42.910 | 4.878 | -9.100 | 1.464 | 0.447 | - |
| | $S_2$ | 42.100 | 3.552 | -14.756 | 1.894 | 0.347 | - |
| | $S_1$ | 43.305 | 2.836 | -19.930 | 2.433 | 0.295 | - |

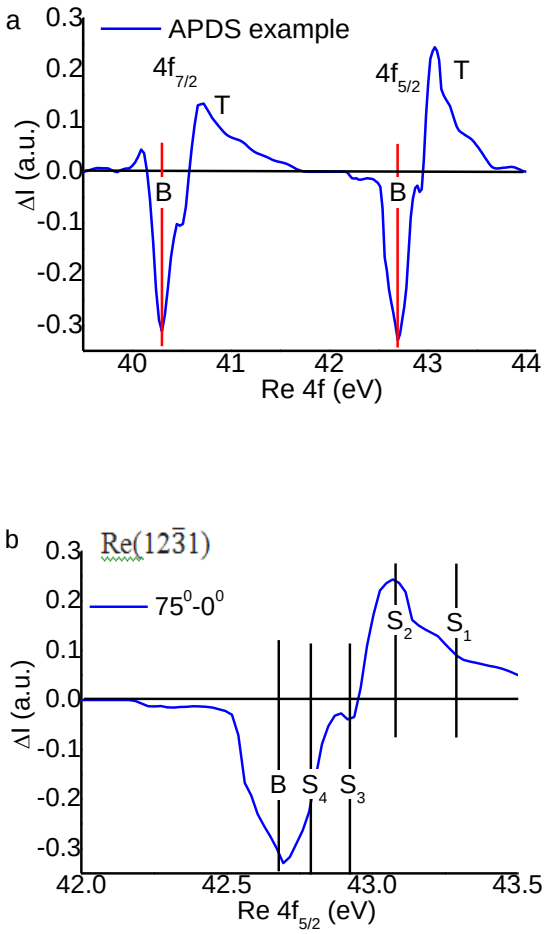


Figure 17 The APSD of (a) the entire Re 4f band of the Re(12$\bar{3}$1) surface.[54] The similar structure of valleys and peaks confirm the consistency between $4f_{7/2}$ and $4f_{5/2}$ bands. The small feature at the upper edge of the $4f_{7/2}$ arises from the purified $5p_{3/2}$. (b) The APSD of the $4f_{5/2}$ band with the valley centered at 42.645 eV includes contribution from the B and the inner $S_4$ and $S_3$ sublayers; the extra gains at the bottom edge corresponds to the under-coordination induced local bond strain and quantum entrapment in the surface skin dominated by the outermost two atomic layers.

Figure 17b shows the APSD of the specific $4f_{5/2}$ level. Two valleys centered at 42.65 eV and 42.91 eV are well resolved, corresponding unambiguously to the removed B and the $S_3$ components, indicating that the valley involves the B, the $S_4$ (centered at 42.778 eV) and the $S_3$ components. Therefore, the APSD presents only information limited to the outermost two atomic layers of the (12$\bar{3}$1) surface. Except

for the valleys, a broad peak at the bottom edge of the $4f_{5/2}$ band represents the gain of electronic energy with the $S_2$ and $S_1$ kinks being involved. The APSD could therefore separate the kinks from the mixture of bulk, the skin and the kink without needing any argument in the B and skin component assignment.

From the spectral bandwidth of the B valley, we can show that the overlap integral $\beta$ is negligible compared with the exchange integral $\alpha$ in the tight-binding approximation of the inner band, as mentioned in Eq.14. The width of a core band is $2z\beta$ and the shift of the band from that of an isolated atom is $\alpha + z\beta$. Based on the width of the B valley for both the $4f_{7/2}$ and the $4f_{5/2}$ bands of ~ 0.25 eV and the bulk shift of $\alpha + z\beta = 2.629$ eV, we have, $\beta/\alpha \approx 0.01/2.50 = 0.4\%$ only.

Figure 18a and b show the decomposed 4f7/2 band for the Re($12\bar{3}1$) surface with and without oxygen chemisorption.[54] Because of the lacking of the oxygen chemisorption spectral data for the $4f_{5/2}$ band, we turned to analyze the $4f_{7/2}$ band. A direct decomposition of the spectra for oxygen adsorbed Re$(12\bar{3}1)$ surface using the coordination wise does no longer hold because of the new bond formation between the adatom and the metal surface atoms. The O-Re bond formation will increase the crystal potential substantially in the adsorbed region, which will lower the surface states further to deeper energies, as shown in Figure 18b.[111, 112] The O-induced Re $4f_{7/2}$ positive shift is in line with what detected from oxygen chemisorbed surfaces,[113] in which the O 2p states shift positively by about 0.5 eV upon oxide

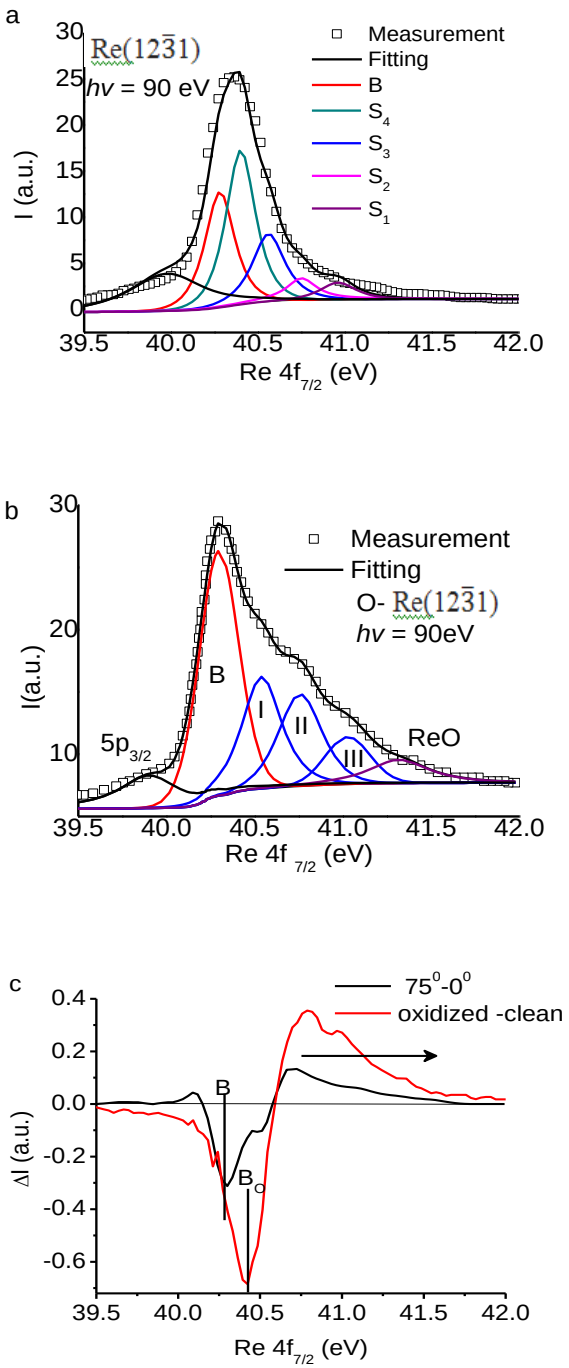


Figure 18 The decomposed XPS Re $4f_{7/2}$ spectra collected from the Re(12$\bar{3}$1) surfaces[54] (a) before and (b) after oxygen adsorption. (c) The APSD for the oxygen adsorbed Re(12$\bar{3}$1)(red line) in comparison to the APSD for Re $4f_{7/2}$ kink states (black line). Extra gain is resolved due to oxygen chemisorption and the bulk component shifts further to deeper energies.

formation. Figure c shows the APSD for the Re(12$\bar{3}$1) surface with and without oxygen adsorption. A valley $B_O$ centered at 40.40 eV is present, being different from

the B and the $S_4$ in the referenced APSD of the un-adsorbed surface. This difference indicates that the O-Re bond is much stronger and the synchrotron beam with 90 eV collects less information from the bulk and the $S_4$ region. The extra states extending to energy are even lower than the surface states of the clean surface. The APSD has thus enabled us to separate the chemisorbed surface states from the mixture and allowed us to estimate the depth of two atomic layers being involved in the adsorption of oxygen.

It has been demonstrated[113] that oxygen prefers the central position of a tetrahedron by interacting with two metal atoms through bonding and two through nonbonding lone pairs of electrons.

### 4.2.3 Conclusion

The XPS spectra for the Re(0001) and Re(12$\bar{3}$1) surfaces with and without oxygen chemisorptions have been analyzed under the guidelines of the BOLS-TB algorithm and the PRS approach. The Re $4f_{5/2}$ BE of $40.015 \pm 0.004$ eV for an isolated Re atom and its bulk shift of 2.629 eV and the layer and orientation resolved effective coordination numbers have been determined for the first time. The APSD revealed entrapped Re(12$\bar{3}$1) surface kink states presenting at the bottom edge of the Re 4f band, which evidences the undercoordination-induced global quantum entrapment in the surface skin and kinks. Applying the same PRS process to the Re(12$\bar{3}$1) surface before and after being chemisorbed with oxygen purified the oxygen chemisorption

states with even lower BE due to the stronger O-Re bonds formed at the surface with two atomic layers being involved.

# 4.3 Terrace Edge on W Surface

## 4.3.1 Introduction

It has been presented in chapter 3 that: The BOLS-TB enabled XPS decomposition of the W(100), (110) ,and (111) surfaces has led to quantitative information about the 4f energy level of an isolated W atom as 28.910 eV and its bulk shift of 2.173 eV. The derived CN-dependent SCLS follows: $E_{4f7/2} = 28.910 \pm 0.006 + 2.173c_z^{-1}$ . According to W terrace edge, Figure  shows the atomic arrangement of the (320) and (540) surfaces with considerable fraction of under-coordinated atoms compared with the flat (110) surface.

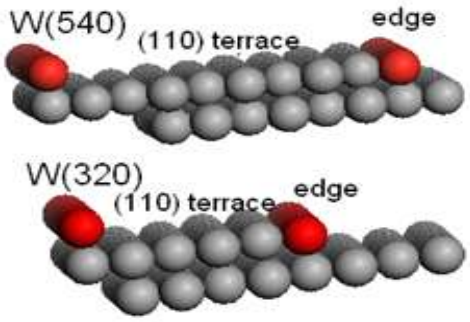


Figure 19 The surface atomic structures of the (100) vicinal (540) and (320) surfaces with edge atoms density. The edge density of (320) is 0.28 monolayer (ML) and the (540) is 0.16 ML.

## 4.3.2 Results and Discussions

From the original W4f spectra shown in Figure 20a for the (110), (320) and (540) surfaces collected under the same experimental conditions,[68] one can hardly discriminate the spectral feature one from another; the PRS process however makes a great difference, as shown in Figure 20b, proceeded by subtracting the spectrum collected from the un-edged (110) surface from the edged ones of the (540) and (320) surface upon the standard process of spectral normalization and background correction using the Shirley method. The correctness of the APSD outcome is justified by the criterion of spectral area conservation, which means that the spectral loss and gain should be identical. The normalization of the spectra is to minimize the artifacts due to scattering of the x-rays by the edge atoms. Unexpectedly, two extra components centered at 30.945 and 31.310 eV present and two valleys centered at 31.083 and 31.454 eV are generated. The emergence of these spectral features indicate that the electronic structure for the edge atoms is indeed different from those at the bulk interior or at the flat surface, but at this moment one can hardly tell why.

Based on the derived CN-dependent SCLS, $E_{4f7/2} = 28.910 \pm 0.006 + 2.173C_z^{-1}$ The B valley at 31.083 eV = 28.910+2.173 eV is unambiguously the bulk component that was defined in the APSD without needing artificial assignment. This finding clarifies the long confusion[66] regarding bulk component that was ever assumed at the bottom edge of the 4f band:

i) The additional T states below the bulk component is the entrapped states because of the undercoordination-induced bond strain and bond strength gain. The locally entrapped T states polarize the valence electrons that cannot be detected directly using XPS but it indeed happens to the Rh and Ag/Pd alloy as confirmed using the ultra-violet spectroscopy showing the consistency of charge polarization direction in all the bands of the same specimen.[72, 114]

ii) The P component at 30.945 eV results from the screening and splitting of the crystal potential by the polarized valence electrons. We can estimate the polarization coefficient with the known energies of the P and the B components, $p = [E_{4f7/2}(p) - E_{4f7/2}(0)] / [E_{4f7/2}(12) - E_{4f7/2}(0)] = (30.945\text{-}28.910)/2.173 = 93.6\ \%$, which means that the crystal potential has been partially screened and elevated by 6.4% of the bulk value.

iii) The otherwise T component turns to be T+P with an additional valley at the bottom edge of the core band because of the coupling effect of entrapment and polarization. The T component is supposed to add component at energy corresponding to $z < 4$, if the polarization is absent or it is sufficiently weak. The state loss (second valley) at 31.454 eV with an effective CN of 3.57 is supposed to be absent; the strong interaction between edge atoms should enhance the intensity of the states at lower-z positions instead if no polarization happens. However, as we discussed, the screening effect also applies to the trapped states, and therefore, this valley presents, and the T component becomes P+T. If the $C_3^{-1}$ is replaced

with $pC_3^{-1} = C_{3.75}^{-1}$, which means that the original edge states located at $z$ = 3 shift up to energy being equivalent to $z$ = 3.75.The edge bond is strengthened by [$E_{4f7/2}$(T+P)- $E_{4f7/2}$(0)] / [$E_{4f7/2}$(12)- $E_{4f7/2}$(0)] = (31.310-28.910)/2.173 = 1.104, or 10.4%, because of the joint effect of entrapment and polarization. It should be 1.104/$p$ =1.104/0.936 = 1.18 instead, if no polarization occurs.

The extra P and the P+T states in the APSD are due to the edge atoms only as the APSD has filtered out the background and bulk information. It has been confirmed that the valence and the core electrons of a specimen shift simultaneously in the same direction because of the screening effect to the core charge, such as the cases of AgPd and CuPd bimetallic alloy catalysts,[72] and the Pt and Rh adatoms. The APSD of W edges share the same attribute to those of Rh adatoms and AgPd alloy. The latter has been identified as donor-type catalysts compared to the Pt adatoms and CuPd alloy that are opposite, because of the respective dominance of polarization and entrapment effect. From the electronic structure wise, we can suggestthat W edges should perform the same to Rh and Ag/Pd as n-type catalysts though experimental confirmation is needed. Nevertheless, the APSD can help us to search for new catalysts and identify the catalytic nature of existing catalysts.

## 4.3.3 Conclusion

The combination of BOLS correlation and XPS measurement provides profound information about the effective atomic CN, local bond strain, bond energy, binding energy density and the atomic cohesive energy in the surface skin up to two atomic

layers of different orientations. A further APSD processing revealed extra features of the bulk valley, polarization and the joint effect of entrapment and polarization and their physical indications, which confirm the positive core-level shift and clarify the long confusion in the bulk component assignment. Results evidence the BOLS expectation of the edge states as resulting from the undercoordination-induced local bond contraction and the associated quantum entrapment and densification of core electrons and the polarization of the otherwise conducting electrons of W edge atoms by the entrapped core charge. Most strikingly, being similar to the spectral features of Rh adatoms and Ag/Pd alloy, W edge is suggested to serve as a donor-type catalyst. As demonstrated, the APSD should provide a powerful tool for one to purify information from atomic-scaled zones surrounding under-coordinated atoms regarding the local bond and energetic behavior of electrons, which is helpful for us to search for new catalysts.

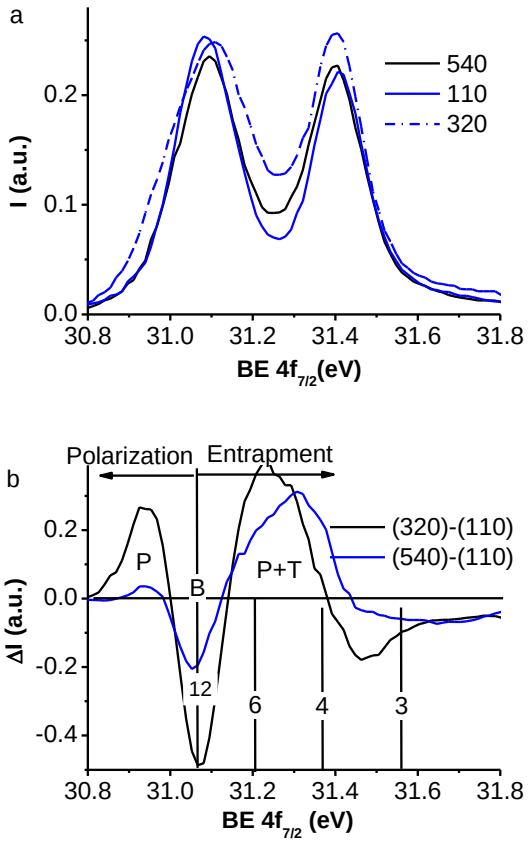


Figure 20 From the normalized the (110), (540), and (320) XPS $4f_{7/2}$ spectra [68] (a) one can hardly discriminate the contribution of the edge atoms from those of the un-edged (110) surface; but (b) the PRS, or subtraction of the un-edged from the edged W(540) and (320) surfaces, can resolve the edge states unambiguously with the P and P+T extra states and the B and the additional valley at the bottom edge. The resultant PRS almost satisfies the criterion of spectra area conservation.

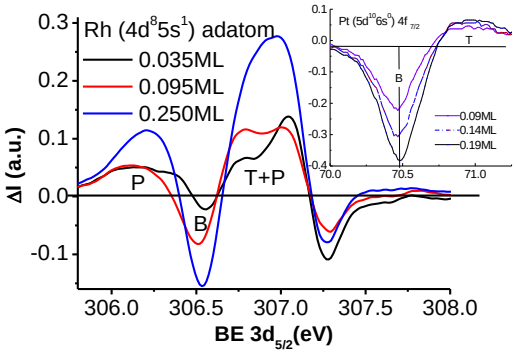


Figure 21 The PRS for Rh adatoms with the inset of Pt adatoms[114] for comparison with Figure 20b. The spectral similarity of the Rh adatoms and W edge atoms suggests that W edge may perform the same to Rh adatoms as a donor-type catalyst.

# 4.4 Pt and Rh Adatoms

## 4.4.1 Introduction

Adatoms adsorbed on certain single crystal surface attracts more interests especially in the study of catalyst. Compared with nanoparticles, adatoms has mucl less atomic CN than that of surface atoms on nanoparticles. In addition, the interaction between the adatoms and the substrates always plays important role in the performance of as adsorbed adatoms, in this section, the homogeneous adatoms on Pt and Rh single crystal surface has been investigated using XPS measurement, and APSD method was also adopted to study the interesting properties of adatoms.

## 4.4.2 Results and Discussion

Thanks to the well-measured sets of XPS data from Pt[108] and Rh[59] surfaces with adatoms that make the current verification of the BOLS expectations possible. Using

high-resolution XPS, Baraldi et al.[59] examined the adatom effect up to 1/4 ML on the $3d_{5/2}$ spectra of Rh(110) and Rh(111) surfaces at photon energy of 380 eV with polar emission angles varying from 20 to 50° with respect to the surface normal. Results showed that the smaller polarization angle from the Rh(111) surface derives a relatively higher intensity of the high-energy bulk component; at the given polar angle and beam energy, the intensity of the low-energy surface peak increases with the coverage of the adatoms compared with other peaks at higher bulk BE of Rh(100). These observations demonstrate the sequence of positive shift. Bianchettin et al.[108] also examined the adatom effect up to 0.19 ML on the Pt $4f_{7/2}$ and decomposed the spectra using two peaks, one is at 71.0 eV and the other around 70.5 eV. The intensity of the 71.0 peak increases with the coverage of adatom compared to that of the 70.5 eV peak, being consistent with that observed from Rh surfaces.

In order to compare the spectral intensity evolution upon adatoms deposition, we need to find the spectral intensity difference between the spectra collected from specimens with different amount (ML coverage) adatoms and the spectrum from the ideally clean surface as a standard. Before doing so, we need to normalize all the spectra using the commonly maximum intensity as reference. For Pt $4f_{7/2}$, the maximum is at 70.52 eV; for Rh $3d_{5/2}$, it is at 307.13 eV. Normalization of all the compared spectra in one set using the highest intensity at certain energy of all the spectra will ensure the full information to be properly analyzed, including the charge

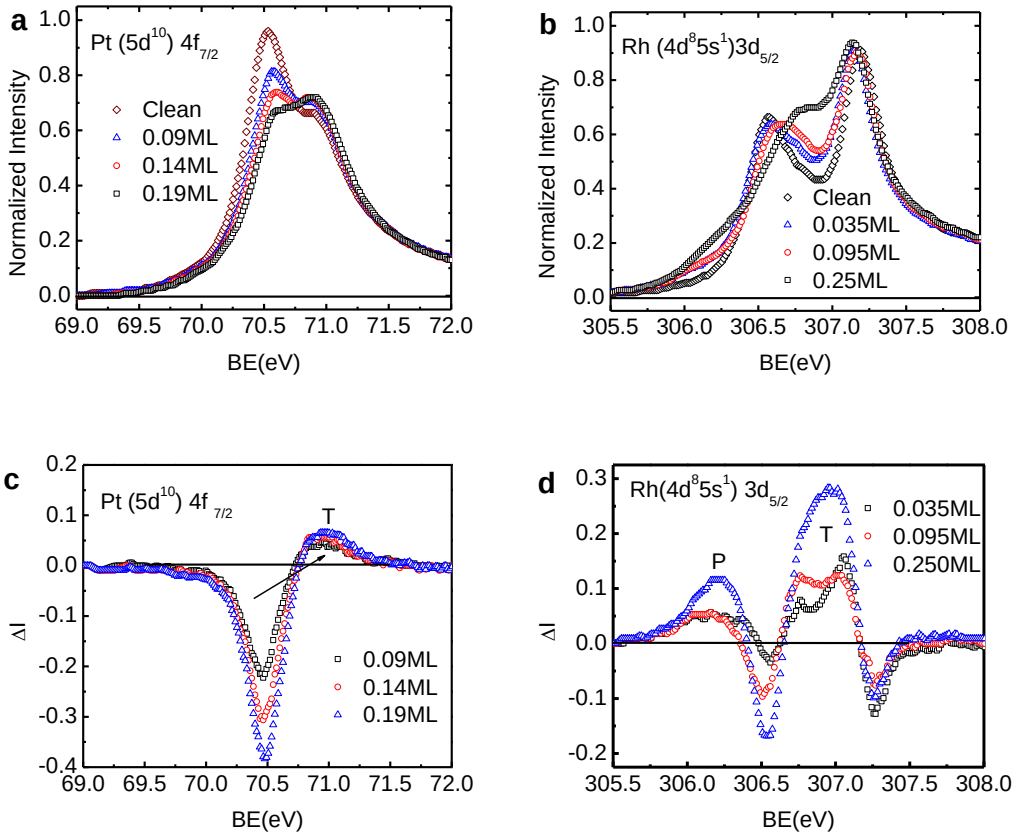


Figure 22 Comparison of the subtracted spectra for surfaces with varied coverage of adatoms by the spectra of clean surfaces of (a) Pt $4f_{7/2}$ [108] and (b) Rh $3d_{5/2}$. [59] Indicated numbers are the effective atomic CNs for bulk (12), surface layers (4, 6), and adatoms (< 4). The spectral differences in (c) and (d) show clearly the presence of quantum trapping effect in both cases and (d) the dominance polarization effect in Rh, which differs Pt from Rh adatoms in catalytic reactions.

polarization and trapping. Figure 22a and b compares the normalized spectra that were collected from Rh and Pt surfaces with different coverage of adatoms. The overlapping of the spectra can hardly show the details clearly regarding the spectral evolution upon homo-adsorption of the surfaces.

In order to view closely the spectral difference, we subtracted the normalized spectrum of the clean surface from those with adatoms to gain the APSD. The APSD are compared in Figure 22c and d. As expected, no polarized features present at all for

Pt specimen. However, the Rh profiles are more complicated. In additional to the trapped states at energies of z =4 and 6, the original trapped states at z = 3 disappear with an addition of the polarized P states centered at 306.2 eV, above the bulk component. It is seen that the extent of trapping and polarization increases with the adatom coverage up to 0.25 ML. Further deposition may reduce the extent though experimental evidence is lacking from the available database.

The APSD between Pt and Rh coincides exceedingly well with the BOLS expectation that only the otherwise conductive half-filled s-electron Rh($4d^8 5s^1$) can be polarized and locked as monopoles to the adatoms, making no contribution to the conductivity. These polarized s-electrons are suggested to be responsible for the magnetism of the small clusters as well.[57, 115] It has been confirmed that the valence and the core electrons of a specimen shift simultaneously in the same direction because the screening effect to the core charge, such as the cases of AgPd and CuPd bimetallic alloy catalysts.[49, 116] AgPd was identified as a donor and CuPd as an acceptor because of the respective polarization and trapping effect.

There are two possible reasons for the loss of the initially trapped surface charge at z = 3: (i) the electrons of adatoms are fully polarized, moving from z = 3 energy to the P states; (ii) the number of the initially z = 3 adatoms is reduced upon deposition of adatoms, which means that the initial flat surface is not so flat but with many edges and steps. Compared with the XPS Pd $3d_{5/2}$ profiles, the XPS $3d_{5/2}$ spectra of Rh surfaces demonstrate asymmetric features.[58, 59] The tails at the lower

energy end indicates the presence of surface defects trapped states. From the analysis, it is understandable now why there is no such P states in the Pt($5d^{10}6s^{0}$) $4f_{7/2}$ spectra because of the unoccupied 6s-orbit.

According to the constraints given, the spectra from clean surface of each Pt and Rh specimen was decomposed with five components, representing the P, B, $S_2$, $S_1$ and A from higher to lower BE, as shown in Figure 23. The decomposition was conducted by choosing $z_1 = 4$ and $z_3 = 12$ for the (100) surface as reference and allowing other components to be optimized in the best fit. For each element, the B energy and $E_v(1)$ remain unchanged for all the surfaces. The optimal component energies and the decomposition parameters are summarized in Table 6. The derived local strain ($c_z$-1) and the effective CNs for the other components are also given.

From the decomposition, we obtained the $E_v(1)$ and $\Delta E_v(B=\infty)$ values. Using a least roof-mean-square method,[64] we can obtain the standard deviation. It has been derived that the BE for an isolated Rh atom is 302.1467±0.0003 eV with the bulk shift of 4.3653 eV and that the BE for an isolated Pt atom is 67.2086±0.0003 eV with the bulk shift of 3.2814 eV. The refinement leads to the effective atomic CNs of the top (100) and (111) atomic layers as 4.00 and 4.25.

The calculations lead to the coordination-resolved BE shift for Rh $3d_{5/2}$ and Pt $4f_{7/2}$:

$$E_v(z) = E_v(1) + \Delta E_v(B=\infty)C_z^{-1} = \begin{cases} 302.1647 \pm 0.0003 + 4.3653C_z^{-1} \\ 67.2086 \pm 0.0003 + 3.2814C_z^{-1} \end{cases}$$

with an addition of the polarized states to the Rh adatoms. Theoretical reproduction of the size dependence of the Pt $3d_{5/2}$ spectra has led to the bulk shift of 2.99±0.31 eV and the $E_{3d}(1)$ = 67.67 eV. The difference may arise from the accuracy of particle size determination. Theses fundamental information should be useful to the understanding of the catalytic behavior of these under-coordinated atoms.

Besides the effective atomic CN and the local strain ($c_z$-1), decomposition of the XPS spectra allows us to derive information regarding the ratio of BE density ($c_z^{-4}$), and the ratio of atomic cohesive energy ($z/z_b c_i^{-1}$) for each surface and adatom component,[57] as listed in Table 6. These quantities are of fundamental importance to the understanding of the surface properties and the processes of surface reaction and nucleation. For instance, the BE density determines uniquely the elastic modulus[74] and the atomic cohesive energy dominates the critical temperature of phase transition.[73]

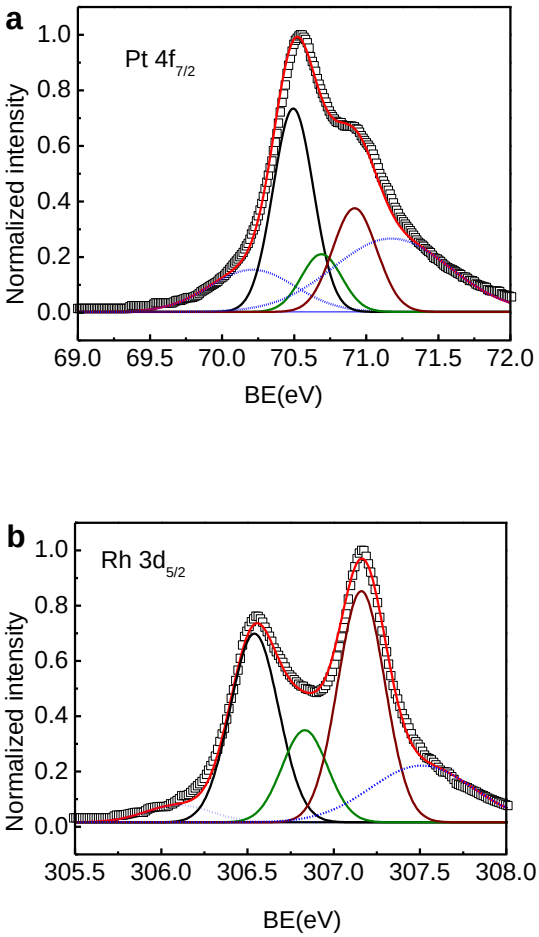


Figure 23 Decomposed XPS spectra of the (a) Pt(111) and (b) Rh(100) clean surfaces with five components each representing the polarized P, bulk B, surfaces $S_1$ and $S_2$, and the adatom A states from lower (larger absolute value) to higher BE. The decomposition parameters are listed in Table 6.

## 4.4.3 Conclusion

We have analyzed the homo-adatom XPS spectra of Pt $4f_{7/2}$ and Rh $3d_{5/2}$ based on the recently developed BOLS theory and Algorithm with derived quantitative information and improved understanding of the catalytic behavior of the under-coordinated atoms: The expectations of broken-bond-induced local strain and quantum trapping and the associated polarization of nonbonding electrons have been confirmed; The spectral

difference provides a powerful tool for identifying the evolution of electrons upon coordination change; The five-component spectral decomposition allows us to extract quantitative information about the energy levels of an isolated atom and to establish the coordination-resolved BE of each component and the corresponding local lattice strain; Approaches and findings may extend to other under-coordinated systems such as atomic defects and nanostructures; Most importantly, the Rh adatom has been identified as a donor and Pt adatom as an acceptor in the catalytic reactions because the XPS-detected respective polarization and quantum trapping effect; Besides the effective atomic CN and the local strain, decomposition of the XPS spectra allows us to derive information regarding the ratio of BE density and the ratio of atomic cohesive energy for each surface and adatom component, which are of fundamental importance to the understanding of the surface properties and the processes of surface reaction and nucleation.

Table 6 Summary of decomposition parameters (BE-BE; W-width; I-intensity) for the Pt and Rh spectra and the BOLS derived effective CN(z), local strain ($c_z - 1$), the ratio of BE density ($c_z^{-4}$) and the ratio of atomic cohesive energy ($z/z_b c_i^{-1}$) for each surface and adatom component. $z_b = 12$.

| | | P | B | $S_2$ | $S_1$ | A |
|---|---|---|---|---|---|---|
| Pt(111) $4f_{7/2}$ | BE | 70.21 | 70.49 | 70.69 | 70.91 | 71.18 |
| | W | 0.70 | 0.33 | 0.33 | 0.36 | 0.95 |
| | I | 0.15 | 0.73 | 0.21 | 0.37 | 0.26 |
| | z | _ | 12 | 6.25 | 4.25 | 3.15 |
| | $c_z$-1 | _ | 0 | -0.05 | -0.113 | -0.174 |
| | $c_z^{-4}$ | - | 1 | 1.27 | 1.62 | 2.15 |
| | $z/z_b c_z^{-1}$ | - | 1 | 0.55 | 0.40 | 0.32 |
| Rh(100) $3d_{5/2}$ | BE | 306.10 | 306.53 | 306.85 | 307.15 | 307.51 |
| | W | 0.45 | 0.33 | 0.31 | 0.32 | 0.70 |
| | I | 0.09 | 0.70 | 0.34 | 0.85 | 0.22 |
| | z | _ | 12 | 5.73 | 4.0 | 3.0 |
| | $c_z$-1 | _ | 0 | -0.068 | -0.124 | -0.183 |
| | $c_z^{-4}$ | - | 1 | 1.327 | 1.700 | 2.248 |
| | $z/z_b c_z^{-1}$ | - | 1 | 0.5129 | 0.381 | 0.308 |

# 4.5 Vacancies on Graphite

## 4.5.1 Introduction

As vehicles for the quantum spin Hall-effect in topological insulators, graphitic Dirac-Fermi polarons (DFPs) associated with atomic undercoordination at the edges of graphene ribbons[12, 117, 118] and the vacancies[119-122]of a graphite surface are indeed fascinating. The DFPs demonstrate anomalies including the extremely low effective mass, extremely high group velocity, and non-zero spin, following the Dirac equation with a nearly linear dispersion crossing Fermi energy.[123-127] In order to identify the origin and consequence of the DFPs, information regarding the behavior of bonds and the energetically low-lying electrons surrounding the DFPs as "roots" is highly desired. However, such localized skin depth information is as yet by no means available. Scanning tunneling microscopy/spectroscopy (STM/S) collects information from the open side of a surface within the energy window of a few eVs surrounding Fermi energy. STM/S provides, however, limited knowledge of the bonds and electrons in zones and energies beneath what the STM/S can probe. In comparison, XPS collects statistic and volumetric information of electrons of several nanometers in depth[88] and energies in the valance band and below. It is possible to purify the bond and electronic information limited to the selected zones by a process of photoelectron residual spectroscopy.

## 4.5.2 Results and Discussions

In order to examine the proposed APSD for spectral information purification, we firstly collected the XPS data from the clean highly-oriented-pyrolytic-graphite (HOPG) surface using the *Sigma Probe* (*Thermal Scientific*) monochromatic Al $K_{\alpha}$(1486.6 eV) as the X-ray source with the emission angles from 25° to 75°. All spectra was recorded by constant pass energy mode with pass energy of 10 eV. The generation and concentration of the defect vacancy was realized and controlled by $Ar^{+}$ ions sputtering of 0.5 keV energy. The sputtering dose was controlled by the sample current and the duration of sputtering.

Figure 24 a and b shows respectively the XPS spectra collected (a) from the defect-free surface at different emission angles and (b) from the surface of different defect densities represented by the $Ar^{+}$ doses at 50°. However, the overall intensities of the raw spectra are relatively weaker for those collected at larger emission angles or from the roughened surfaces because of information mixture from different depth profile or spectra components.

In the APSD processing, we firstly corrected the spectra using the standard process of Shelly background correction before doing the spectral area normalization. The spectra collected from the defect-free surface at larger emission angles were then subtracted by the referential one collected from the freshly-cleaved surface at the least

(25°) available angle. For the surfaces with defects, we simply repeat the process at 50° without changing the emission angle.

Figure 24c and d show the evolution of the APSD for the defect-free surface (c) and surface with defect densities as represented by the dose of $Ar^+$ sputtering (d). The insets show the zones (in blue color) dominating the extra states in each case. The areas above and below the x-axis are, respectively, the gain and loss of the energy states under the given conditions. The walleyes at 284.2 eV in (c) and 284.4 in (d) correspond to the subtracted bulk and surface-bulk components.

For the defect-free surface, only one entrapped peak ($T_S$) is present at the bottom edge of the C 1s band, which shifts further to a lower binding energy corresponding to the evolution of the effective atomic CN from z ~ 4 to z ~ 3.2, as the emission angle increases from 35° to 75°. As defects are generated, the $T_S$ moves to energy even deeper and evolves into $T_D$. The $T_D$ is associated simultaneously with the emergence of both the DFPs at the Fermi energy[12, 117-122] and the P component at the upper edge of the C 1s band. As the defect density is increased, the intensity of the $T_D$ component grows and the P component moves up in both energy and intensity, which indicates that the extent of polarization increases with the density of defects. The presence and evolution of the $T_S$ to the $T_D$ component is referred to as a positive core level shift due to the surface- and defect-induced quantum entrapment making the C 1s band deeper when the atomic CN is decreased, which verify further Goldschmidt-Pauling's premise of bond contraction.

Figure 25 summarizes our findings of the APSD collected at 75° emission angle from surfaces with and without defects. The atomic CN for the graphite skin is ~3.1 and for the vacancy neighbors it is ~2.2. The energy ranges for both the $T_S$ and $T_D$ components correspond to the z values for atoms in the outermost two atomic layers. The P component is centered at 283.63 eV, 0.31 eV above that (283.94 eV) of the bulk diamond. Therefore, the polarization coefficient $p$ = (283.63-282.57)/(283.94-282.57) = 1.06/1.32= 0.80, which means that the DFPs screening raises the potential by 20% compared with that in diamond, while the vacancy trapping potential is $C_{z=2.5}^{-2.56}-1=0.97$ times deeper. According to the energy band theory,[128] the separation between the $T_S$ or the $T_D$ and the $E_{1s}(0)$ = 282.57 eV is proportional to the bond energy. The defect bond ($T_D$) are estimated to be (285.25-282.57)/(284.70-282.57) = 1.25 times stronger than bond at the surface ($T_S$), agreeing with the trend of energy requirement for the 2- and 3-coordinated graphene bond breaking.[12]

## 4.5.3 Conclusion

In summary, the APSD has enabled the first extraction and purification of bond and electronic information from a sheet of atomic-diameter-thick and hence clarified the physical "root' and consequence of the graphitic DFPs created at sites surrounding vacancy defects at graphite surface, which is the same as those at the edges of graphene because of the same STM/S attributes.[12, 117-122] It has been confirmed that the DFPs generate in the following processes: (i) the shorter and stronger bonds between under-coordinated atoms cause local densification and quantum entrapment of charge and energy that produces the entrapped component in the core band; (ii) the entrapped

core charge polarizes the unpaired dangling-bond electrons to produce the DFPs; and, (iii) the DFPs in turn screen and split the potential and then generate the P component in the upper edge of the core band. For the clean surface, no P component presents though the $T_S$ remains because of the lacking of the dangling bond electrons. The APSD is therefore demonstrated more revealing than using either of the STM/S or the XPS alone in purifying bond and electronic information limited to the atomic-diameter-thick covering sheet under the under-coordinated surface and defect atoms.

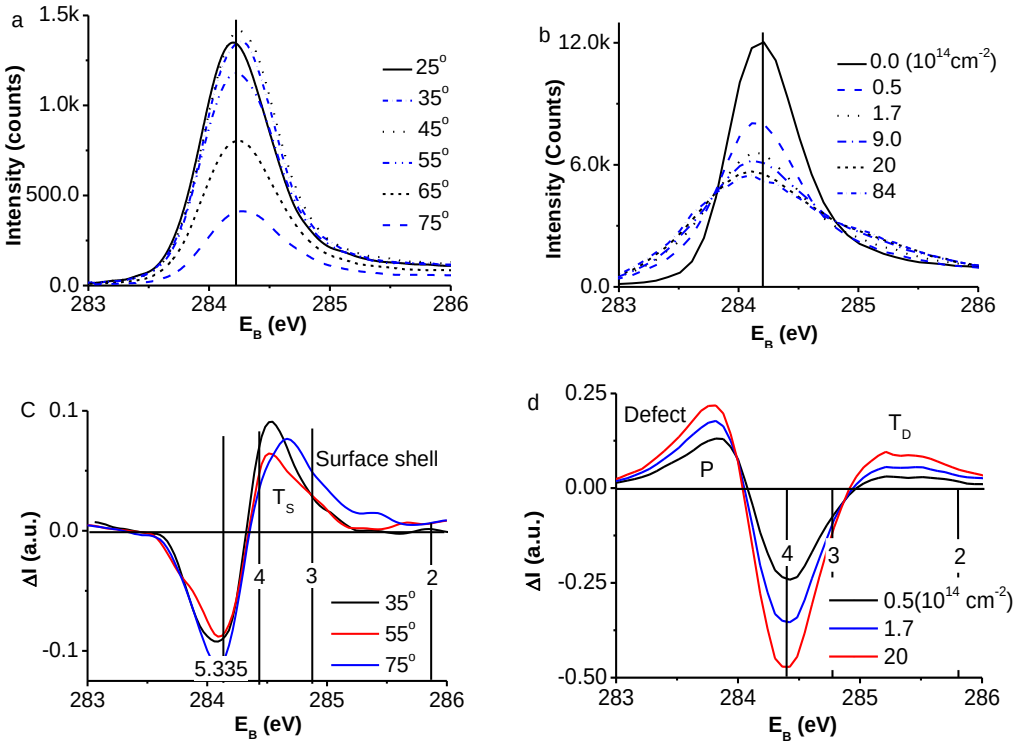


Figure 24 The raw XPS spectra collected from (a) defect-free HOPG surface at different emission angles and (b) the defect surface at 50° of different $Ar^+$ sputtering doses. (c) The purified XPS shows only the trapped ($T_S$) surface states evolving from z ~ 4 to z ~3.2 with emission angle increasing and (d) both the trapped ($T_D$) and polarized (P) states to the defects.

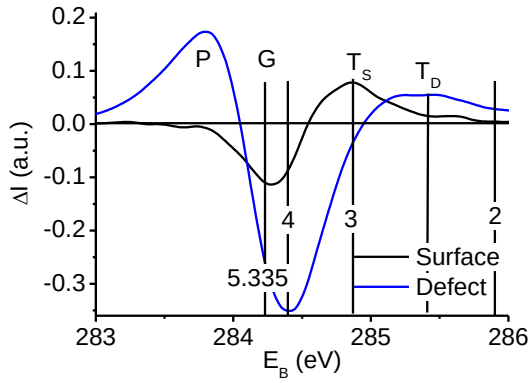


Figure 25 Comparison of the purified XPS C 1s spectrum collected at 75° from the surface with ($9\times10^{14}$ $cm^{-2}$ dosed $Ar^{+}$ sputtering) and without defects. The valleys centered at 284.2and 284.4 eV correspond**,** respectively, to the removed obvious graphite bulk and surface-bulk information and the extra components are the energy states due to the surface skin, $T_S(z \sim 3.1)$, within the outermost two atomic layers and sites surrounding vacancy defects, $T_D(z \sim 2.2)$. G denotes the bulk graphite (z = 5.335). The P component at the upper edge arises from the screening and splitting of the crystal potential by the DFPs that originate from the polarization of the entrapped ($T_D$ in the bottom of the core band) core electrons.

# Chapter 5 Size Dependent BE Shift of Metal Nanoparticles

## 5.1 Introduction

Metal nanoparticles have been attracted tremendous interests in recent years, owing to their intriguing properties in electronic structure[129, 130], mechanical strength[131], chemical and thermal stability[132], magnetism[133], and catalytic performance[134-136] and potential applications in devices and materials functionalization in nanoscale,[137]. The degree of the size freedom of metal nanoparticles has been indeed fascinating because the size reduction enables all the otherwise constant quantities such as atom bond length[42, 53], melting point[138], and band gap[139, 140], to be tunable, as well surface relaxation and related modification in surface morphology and electronic configuration[141-146]. It has been confirmed that the BE of metal nanoparticles shifts positively from as its size is decreased.[29, 30, 147, 148] The relation between the size variation and the BE shift has been discussed extensively for more than half a century and a series of theoretical calculations have also been performed. However, the mechanism to this phenomenon is still under debate. Amongst the available models as mentioned in chapter 2.5, the Coulomb effect[28, 29] of charged nanoparticles with one hole left after an electron being emitted out is suggested to be responsible for the corresponding BE shift. Whereas, the coulomb effect is unable to explain the fact that the BE values of

dissimilar core levels of the same specimen shift differently. Another model is the "initial and final state" effect,[30, 149] which defines the "initial state" effect as the shift induced by the electron configuration modification and chemical environment variation of nanoparticles before being excited by the incident X-ray. The "final state" effect means the relaxation arising from the process of photoelectron emission. Although this model has been widely used, quantitative information regarding which of the "initial state" or the "final state" is dominant cannot be extracted accurately from measurement. Thus, Universal laws governing the size dependent BE shift in nanoparticles should be established.[17, 37, 42, 150-157]

In chapter 2, we have demonstrated that as the size of nanoparticles decreases the core level energy shifts to higher value. The magnitude of the BE shift for different nanoparticles is dependent on the size evolution, the constituent elements and the supportive substrates. In this chapter, several metal nanoparticlas on different substrates are synthesized in UHV environment and *in-situ* XPS measurements are performed. The trend of BE shifts of metal nanoparticles is obtained and the relation between the size variation and the BE shift has been discussed.

## 5.2 Ni Nanoparticles.

## 5.2.1 Ni Nanoparticles on $SiO_2$/Si Substrate

### 5.2.1.1 Synthesis of Ni Nanoparticles

$SiO_2$/Si substrate was synthesized by wet chemical method. First, silicon chip was dipped 2% HF solution for half an hour to dissolve the $SiO_2$ layer formed in air. Then, silicon chip was put into mixed solution of $H_2O_2$ and $HNO_3$ with volume ratio of 1:3 for 30 minutes. Finally, it was airproofed in dry oven at 90 $^0$C for half an hour. The thickness of $SiO_2$ on Si chip was measured by the XPS shown in Figure 26. All XPS measurements were performed using VG ESCAlAB 220i-XL instrument. Monochromatic Al Kα (1486.6 eV) was set as the X-ray source. The XPS was calibrated using pure gold, silver, and copper standard samples by setting the $Au4f_{7/2}$, $Ag3d_{5/2}$ and $Cu2p_{3/2}$ peaks at BE of 83.98 ±0.02 eV, 368.26 ±0.02 eV, 932.67 ±0.02 eV, respectively. The pass energy of 20 eV was used for all spectra. In Figure 26, the peak near 99 eV is denoted as Si 2p for pure Si and the peak near 103 eV represents the Si 2p in $SiO_2$. The thickness of $SiO_2$ could calculate following equation below:

$$d = \lambda sin\theta ln\left(\frac{I(SiO_2)}{\beta I(Si)} + 1\right)$$

Where $\lambda$ is the effective attenuation length of photoelectrons. $\theta$ is the take off angle which equals $90^0$ in our experiment. $\beta = I_{SiO_2,\infty}/I_{Si,\infty}$. Adopting λ=2.96 nm and β=0.75,[158, 159] the thickness of $SiO_2$ is calculated as 0.64 nm. Prior to Ni deposition, as prepared $SiO_2$ substrate was cleaned using ultrasonic treatment in acetone solvent, then, annealed at 773 K in the UHV preparation chamber. Ni

nanoparticles were deposited by an Omicron EFM3 e-beam evaporator in the UHV preparation chamber. Commercial Ni rod was purchased with normal purity of 99.999%. Different deposition time was adopted to form Ni nanoparticles with different size. After deposition, it was transferred to the analysis chamber directly without any exposure to air.

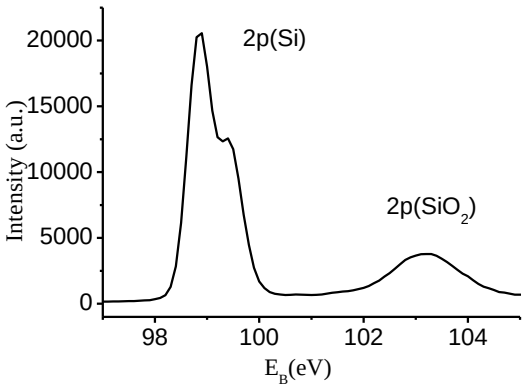


Figure 26 Si 2p core level of $SiO_2$/Si substrate.

### 5.2.1.2 Size Measurement of Ni Nanoparticles on $SiO_2$/Si Substrates

Figure 27 showed a schematic of a metal island (nanoparticle) supported on a flat oxide surface. In the simplified without the consideration of metal surface energy anisotropies, a mechanical equilibrium for the complex can be written by Young's equation:

$$\gamma_{subs} = \gamma_{metal} cos\theta + \gamma_{interface}$$

Where, $\gamma_{sub}$, $\gamma_{metal}$ and $\gamma_{interface}$ are the surface free energy of the oxide substrate, the metal overlayer and metal–oxide interaction, respectively. $\theta$ is the contact angle of metal overlayer on oxide support. Experimentally, the work of adhesion ($W_{ad}$) rather than the interface energy can be measured. $W_{ad}$ is expressed by the following formula:

$$W_{ad} = \gamma_{subs} + \gamma_{metal} - \gamma_{interface}$$

Thus, the mechanical strength at the interfaces is closely related to the metal–oxide interaction. According to equation, interface strongly influences the growth behavior of metal overlayers, determining wetting or non-wetting of the metal, layer growth or island growth of the metal, etc. When $W_{ad}$ is larger than zero, the growth of metal will follows Volmer-Weber mode. Metal Ni deposited on $SiO_2$/Si substrate is island shape because of the small surface free energy of substrate and metal overlayer.

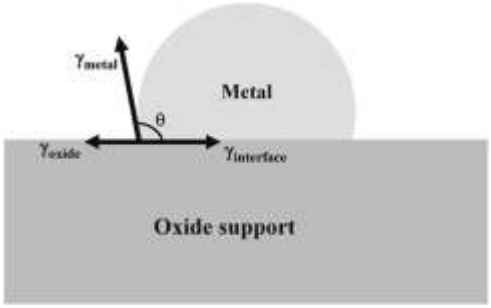


Figure 27 Schematic of Ni nanoparticles on oxide substrate in thermodynamic equilibrium.

To gain an accurate size distribution of Ni nanoparticles on $SiO_2$/Si substrate, TEM measurement is adopted. Figure 28 shows the TEM images of Ni nanoparticles deposited on $SiO_2$/Si substrate for different deposition times and respective size

histogram. The TEM measurement for specimens at two deposition time is given. As shown in Figure 28(a), for 2 minutes deposition, spherical Ni nanoparticles are observed, which morphologies is similar to the results reported for Ni growing on $TiO_2$(100) and (110)[160-162] and teflon substrates[38]. The size distribution of radius is calculated as $1.13 \pm 0.03$ nm as shown in Figure 28(b). In Figure 28(c), as the deposition time prolongs to 30 minutes(min), the Ni nanoparticles still keep the spherical shape with radius size distribution of $3.5 \pm 0.3$ nm, as shown in Figure 28(d). Thus, the growth of Ni nanoparticles on $SiO_2$ substrate follows the Volmer-Weber **(**island**)** mode. In Figure 28(c), the coalescence between bigger Ni nanoparticles appears, although every isolated nanoparticle in coalescent is facile to be differentiated. Some smaller Ni nanoparticles also turn out at this moment, which may be induced by the second nucleation for continuous Ni deposition.

#### 5.2.1.3 XPS Measurement of Ni Nanoparticles on $SiO_2$/Si Substrates

Figure 29(a) shows the Ni $2p_{3/2}$ spectra as a function of deposition time. For convenient observation, all the spectra are normalized with respect to their peak intensity maximum. Comparing the $2p_{3/2}$ spectra of Ni nanoparticles, a positive shift towards the high BE is observed as the deposition time is decreased, which is consistent with the previously reported trends.[163-165] In order to obtain the peak position, we decompose the spectrum using the AVANTAGE commercial software

and Shirley background subtraction is adopted. Figure 29(b) shows the best fit of a typical spectrum that was collected at deposition time of 5 min. It is derived from the decomposition that the $2p_{3/2}$ peak shifts from 854.08 to 853.25 eV as the Ni deposition time increases from 20 seconds to 60 minutes. There is another small peak which is easily assigned to the satellite of Ni $2p_{3/2}$ peak induced by the interaction between the outgoing electron and the valence electron. The distance between Ni $2p_{3/2}$ peak and satellite peak is about 6 eV.

#### 5.2.1.4 Discussion on Size Dependent BE Shift

Increasing evidence supports the expectation that surface modifications become significant as small size.[37, 41, 53] For example, Mironets et al.[41] demonstrated that the mean lattice constant of Co nano-islands deposited on Cu(001) substrate contracts by 6% from the bulk value of 0.251 nm to 0.236 nm when one moves from the center to the edge of the nano-islands. Since lattice strain occurs at surface skin up to a few atomic layers, an additional depression of the potential well takes effect on the BE of the core electrons. For $Cu_{18}$ and $Ni_{18}$ atomic clusters, calculations[37] suggested that the BE for both the initial and the final states undergo positive shifts from zero to 0.7 ~ 0.8 eV when the average strain of the clusters are increased from zero to 6%. An atomic layer-resolved XPS of Ni surface[40] revealed that the surface

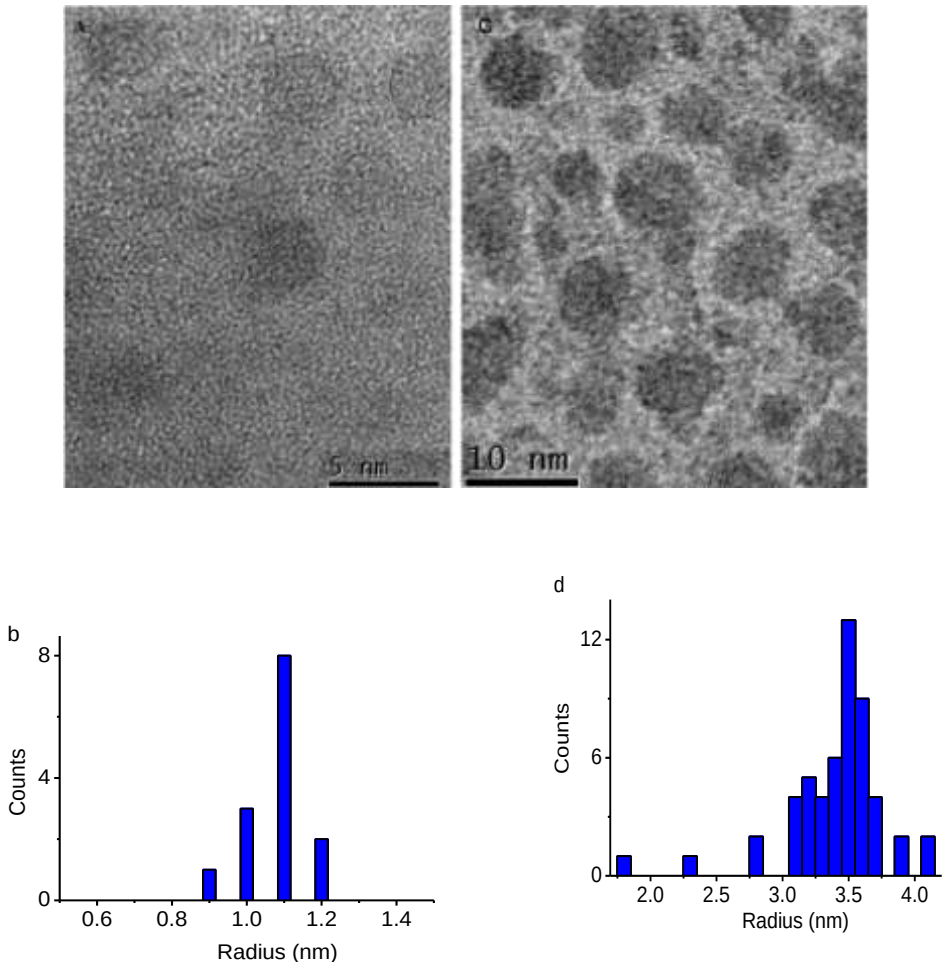


Figure 28 TEM observation of Ni nanoparticles deposited on $SiO_2$ substrate for deposition time of (a) 2 min and (c) 30 min. (b) and (d) are the corresponding nanoparticles size histogram. The circled boundary of nanoparticle in (a) is for viewing convenience.

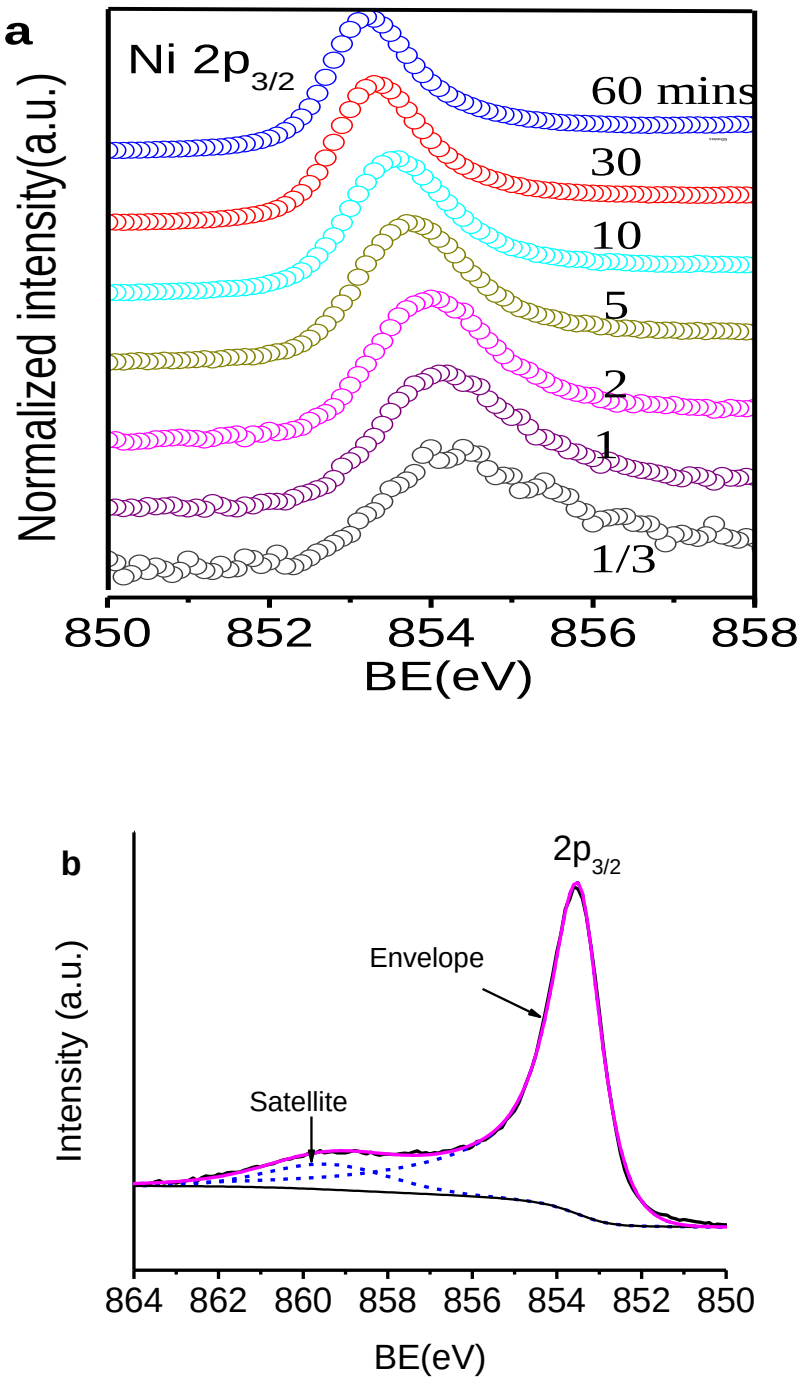


Figure 29 (a) XPS Ni $2p_{3/2}$ profiles at different deposition time (b) peak fitting of $2p_{3/2}$ core level, the Shirley background subtraction is adopted.

core level shift positively and that the outermost layer shift most. All the observations support the deduction from BOLS correlation. Figure 30 compares the BOLS reproduction and the experimental data on size dependent BE shift. Based on the TEM measurement for Ni clusters size and Decomposition of all the available spectra for different sizes, we gain values of the $[E_v(\infty) - E_v(1)]$ and the $E_v(1)$ using the Eqs. and in chapter 2. The Ni $2p_{3/2}$ BE of an isolated atom is 850.51 eV and the bulk BE is 853.21 eV. In the calculation, m =1 and $\tau$=3 are used for the three-dimensional Ni nanoparticles as observed using TEM. The bulk BE value of Ni $2p_{3/2}$ agrees with those reported in the literature[28, 166]. The corresponding bulk shift $[E_v(\infty) - E_v(1)]$ for Ni $2p_{3/2}$ core level is 2.70 eV. The $[E_v(\infty) - E_v(1)]$ and $E_v(1)$ can also be obtained by direct fitting to the experimental data using the established linear dependence of the BE on solid size:[167, 168] $E_v(K) = A + B/K$ . $K$ is the dimensionless form of size. Equating this relation to the BOLS expression given in Eq.35, we could find the correspondence: $\mathrm{A} = E_v(\infty)$and $\mathrm{B} = [E_v(\infty) - E_v(1)] \times \tau \times \Delta_H$. Thus, parameter A represents the bulk BE and the slope B demonstrates the integrated effects of intrinsic bulk BE shift such as the growth mode and the perturbation of Hamiltonian in the surface skin. The bulk shift of $[E_v(\infty) - E_v(1)]$ could be calculated by the values of A and B which is gained following the linear fitting of experimental data. From this fitting as shown in the inset of Figure 30, A and B are determined as 853.26 and 1.71 eV, respectively. The bulk shift is 2.62 eV, close to the value of 2.70 eV obtained from BOLS calculation. Therefore, both

spectral fitting and size fitting give the same value within the error tolerance. It is now clear that the size dependent BE shift for Ni nanoclusters originates from the perturbation in the Hamiltonian by the shorter and stronger bonds between under-coordinated atoms. This conclusion supports Richter et al.[37]and Bagus et al.[169]who suggested that the lattice contraction in Ag nanoclusters plays the dominant role in determining the BE shift.

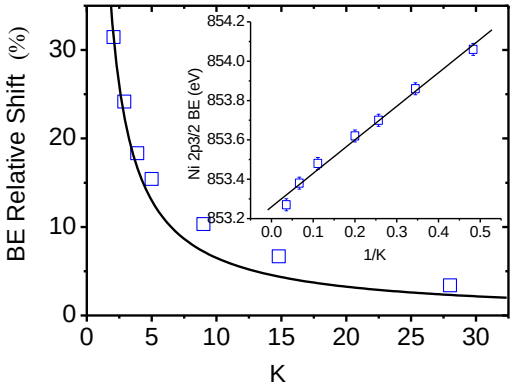


Figure 30 Consistency between the BOLS prediction (solid line) and the measured BE of Ni $2p_{3/2}$ (scattered data) of Ni nanoparticles. Inset is the least mean-root-square fitting of the BE of Ni $2p_{3/2}$ to the inverse of size: $E_v(K) = 853.26\pm0.02 + (1.71\pm0.07)/K$.

### 5.2.1.5 Full-Width-at-Half-Maximum of Ni $2p_{3/2}$

Figure 31(a) illustrates the Full-Width-at-Half-Maximum (FWHM) of Ni 2p3/2 peak for different deposition time. The FWHM of Ni 2p3/2 peak decreases rapidly from 2.0 eV for Ni deposition time of 20 seconds to 1.0 eV for that of 60 minutes which is the same to the value of bulk Ni[150]. This FWHM size trend is within the expectation of quantum trapping and the polarization of the otherwise conducting electrons by the

densely trapped binding electrons.[114] The smaller the particle size, the stronger of the effect of trapping and polarization, and hence the wider of the spectrum will be. To get the detailed comparison, we subtract the spectrum of 5 min by the 60 min one after the normalization of each. As shown in Figure 31(b), the residual peak at lower binding energy indicates that the effect of quantum trapping is more significant for smaller size. No apparent polarization peak at the high binding energy side is observed because of the size effect dominance in nanostructures.

#### 5.2.1.6 Conclusion

Combining the tight-binding theory, BOLS correlation and the XPS measurement, we have determined the $2p_{3/2}$ BE of 850.51 eV for an isolated Ni atom and the bulk shift of 2.70 eV from the measured size dependent spectra. It has been clarified that the size dependent BE shift for Ni nanoclusters originates from the perturbation in the Hamiltonian by the shorter and stronger bonds between under-coordinated atoms. The size dependent FWHM change confirms the BOLS expected quantum trapping states due to atomic under-coordination.

### 5.2.2 Ni Nanoparticles on $SrTiO_3$(100) Substrate

#### 5.2.2.1 Preparation of STO Substrate

$SrTiO_3$ (STO) is a model material of the perovskite-type oxides ($ABO_3$). It has many technological applications, e.g., in sensors, gate dielectrics, and as photocatalysts. In

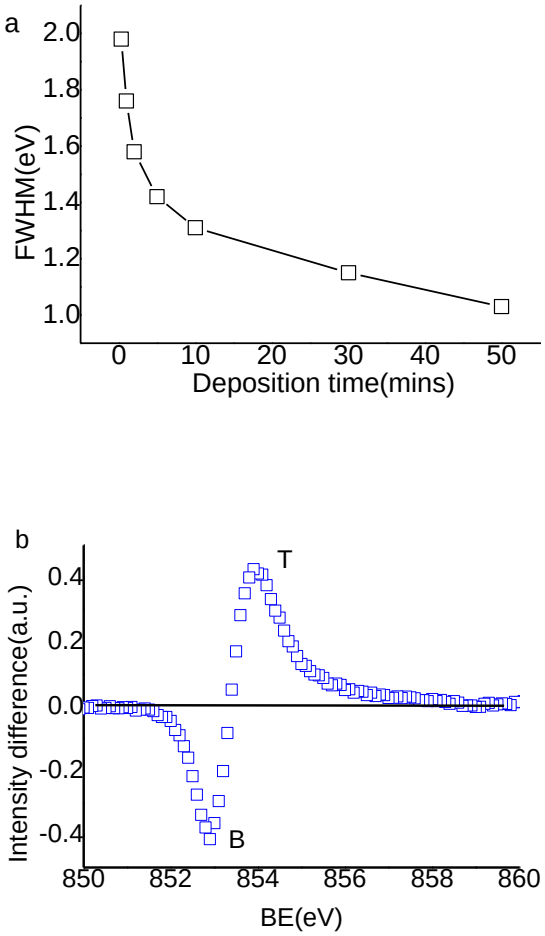


Figure 31 (a)the FWHM variation with deposition times ranging from 20 sec to 60 minutes.(b) The residual spectrum shows the effect of quantum trapping (T).

addition, STO has been widely used as a substrate for epitaxial growth of high-$T_c$ superconductors, metals, and oxides films. The (100), (110), and (111) facets of STO are the most commonly studied surfaces in the experiments. Among them, the (110) and (111) surfaces are polar, while the (100) surface is non-polar. Since a STO crystal consists of a stack of alternating $TiO_2$ and SrO layers, a STO (100) surface may have two distinct terminations: $TiO_2$ termination and SrO termination. It has been found that etching of pre-polished $SrTiO_3$(100) substrates in $NH_4F$-buffered HF (BHF)

solutions selectively removes surface SrO groups as well as calcium impurities leaving the surface terminated with Ti and O.[170, 171] The reproducibility of the surface etching process has been improved through hydroxylation of the topmost SrO layer, which enhances the etching-selectivity of SrO relative to $TiO_2$ in a BHF solution.[172, 173] Atomical flat surfaces with a $TiO_2$-termination can be obtained by the chemical etching followed by heating in $O_2$ and UHV. The surface termination

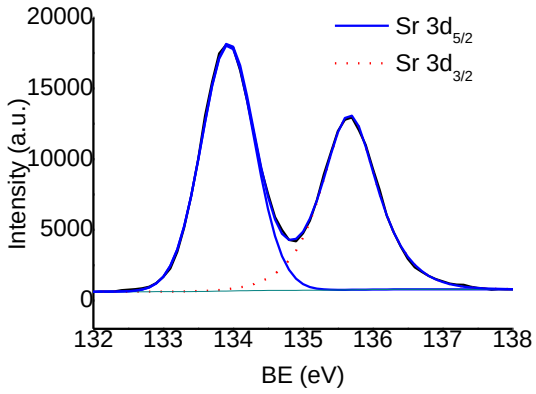


Figure 32 The XPS of Sr 3d BE of clean STO (100) surface.

can be switched to the SrO-termination by depositing a monolayer of SrO on the $TiO_2$-terminated surface.[174] Electron energy loss spectroscopy (EELS) measurements indicate that the electronic structures of the two differently terminated surfaces are different. $TiO_2$-terminated surfaces show intrinsic surface states while SrO terminated surface does not exhibit such states. It has been seen that the photocatalytic activity on the SrO-terminated surface is lower than that on the $TiO_2$-terminated surface.

In our experiment, commercial STO (100) substrate was cleaned firstly by ultrasonic in acetone solution, then, annealed at 773 K in preparation chamber with high vacuum of $1.0\times10^{-9}$ Torr. Ni metal was deposited by an Omicron EFM3 e-beam evaporator using Ni rod with purity of 99.999%. After Ni deposition, the sample was transferred directly into analysis chamber for XPS measurement. Figure 32 shows the XPS of clean STO (100) surface. The Sr $3d_{5/2}$ and $3d_{3/2}$ peaks locate at 133.90 eV and 135.60 eV respectively.

### 5.2.2.2 Results and Discussions

Figure 33 shows the XPS of 2p3/2 and 3p energy bands as a function of Ni coverage. The thickness of the Ni nanoparticles is calculated using the equation as follows:

$$I(t) = I(\infty)[1 - \exp\left(\frac{-t}{\lambda_{Ni} sin\theta}\right)]$$

Where[175]

$$\begin{cases} \lambda_{Ni} = \alpha(\frac{538}{E^2} + 0.41(\alpha E)^{\frac{1}{2}}) \\ \alpha = \frac{A}{\rho N} \times 10^{24} \end{cases}$$

$A$ is the atomic weight of Ni, $\rho = 8.89 \times 10^3\ kg/m^3$ is the bulk density, N is Avogadro's number, $\theta$ is the take-off angle. Following the equation, the thickness of Ni monolayer which is defined as the same packing density of Ni (111) surface $(0.9 \times 10^{14}\ \mathrm{atom/cm^2})$ is 0.22 nm. In the process of Ni deposition, the positions of Sr $3d_{5/2}$ and $3d_{3/2}$ peaks keep same with that of clean STO surface, as well as the O1s

and Ti 2p, which confirms no interaction between the Ni overlayer and STO surface. For viewing convenience, all spectra in Figure 33 are normalized with respect to the highest peak intensity. In Figure 33(a), 0.8 eV positive shift for $2p_{3/2}$ peak is observed as the Ni coverage decreases from 17.2 monolayer(ML) to 0.27 ML. When the thickness is more than 8 ML, the Ni $2p_{3/2}$ BE reaches to the bulk value at 853.19 eV, agreeing with previous observations for Ni growing on different inert substrates.[150, 176, 177] To obtain the accurate peak value, the peak fitting is done after the background subtraction in Shirley mode as shown by insert in Figure 33(a). A weak peak (∼860 eV) around 6 eV higher than the main peak of Ni $2p_{3/2}$ is assigned to the satellite peak. The 3p peak spectra shown in Figure 33(b), are the mixture consisting of $3p_{3/2}$ and $3p_{1/2}$ energy bands because of the weak crystal potential screening splitting. Peak fitting is also conducted as shown in the insert, abiding by the intensity formula of 1:2 for $2p_{1/2}$:$2p_{3/2}$. Compared $2p_{3/2}$ and 3p energy band, similar trend of positive BE shift for two core levels as the function of thickness are observed. however, the magnitude of the BE shift of $3p_{3/2}$ is around 1.3 eV, much greater than that of $2p_{3/2}$ peak (0.8 eV).[178]

In the BOLS convention,[64] coordination number of surface atom in outermost three atomic layers are assumed: $z_1$ = 4, and $z_2$ = 6, $z_3$ = 12, The bond contraction coefficient follows the Eq.21 as: $c_1$ = 0.88, $c_2$ = 0.94, and $c_3$ = 1; $m$ = 1 (for metals) has been optimized in previous findings;[47, 57] parameter $\tau = 1$ is to

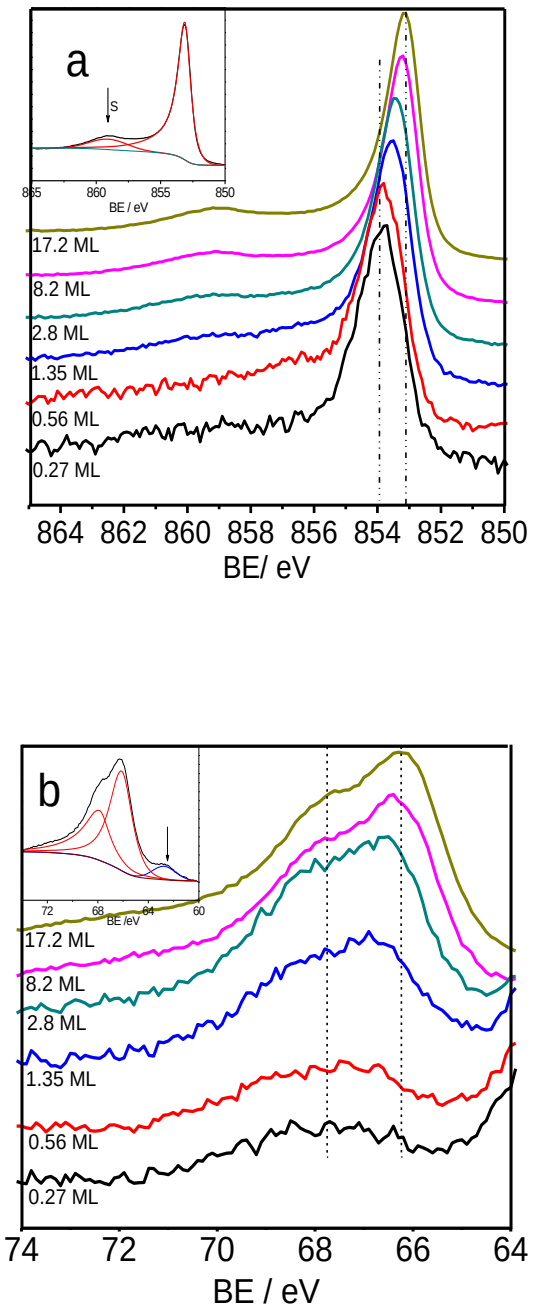


Figure 33 XPS Ni $2p_{3/2}$ (a) and (b) Ni 3p (b) spectra showing the BE shift as a function of Ni coverage deposited onto STO(100) surface. The inserts are the corresponding peak fitting. 'S' represents the satellite peak.

describe the one dimensionality of Ni nanoparticles because the thickness of 'ML' is adopted, while the morphology of Ni deposited on STO(100) surface has been reported in three dimensional island[179, 180] or multi-layer[181, 182](semi-three dimensional island) structure. By combination of accurate peak position and BOLS correlation, the binding energies of an isolated Ni atom are calculated as 850.51 eV for Ni $2p_{3/2}$ and 62.16 eV for Ni $3p_{3/2}$, with corresponding bulk shifts of 2.70 eV and 3.91 eV, respectively. It should be noted that the bulk shift is referred to the position of the isolated Ni atom which is a constant. Figure 34 shows the comparison between of prediction from BOLS correlation and t experimental data. The well coincidence for the two Ni core levels of $2p_{3/2}$ and $3p_{3/2}$ which are predicted to follow same trend demonstrates the effective deduction from BOLS correlation.

The discussion of the BOLS correlation on the BE shift of Ni deposited on STO(100) surface deduces that the bond contraction and strengthening on the surface of Ni nanoclusters is the key factor to take effect on the BE shift , which could be classified to the "initial state" effect. The "final state" effect is negligible. To confirm this conclusion, traditional method of Auger Parameter (AP) is adopted to differentiate the contribution from the "initial state" or "final state" effect in the BE shift of Ni nanoparticles.

AP was proposed firstly by Wagner in 1971 at the first International Conference on Electron Spectroscopy. The original purpose to develop this parameter is to establish the analytical utility of Auger line in XPS. Strong chemical effects were

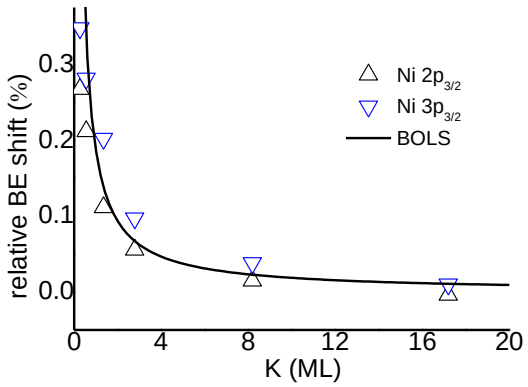


Figure 34 BOLS algorithm reproduction of the relative BE shift of both the $2p_{3/2}$ and the $3p_{3/2}$ derives the values of: $E_{2p_{3/2}}(1)$ = 850.51 eV, $E_{2p_{3/2}}(\infty)$ =2.70 eV; $E_{3p_{3/2}}(1)$ = 62.16 eV, and $E_{3p_{3/2}}(\infty)$ =3.91 eV.

noted on the shapes, intensities and location of Auger line involving valence levels. In fact, in many case, Auger line shift with the chemical states was larger than that observed in that of photoelectron lines. The concept of AP was based on the following ideas:

1. There is a fixed difference between two line (Auger and photoelectron) energies of the same element in the same sample.
2. Work function corrections are also unnecessary and vacuum level data can directly be compared to Fermi level data.

Wagner noted that the difference in two kinetic energies, which is accurately measurable in the presence of statically charging, can be very useful in the characterization of insulators and semiconductor materials. The original AP[183-185] was defined as difference in kinetic energies of prominent and conveniently situated

Auger and photoelectron peaks from same element, recorded in the same spectrum, i.e.

$$\alpha = E_K(C'C''C''') - E_K(C)$$

Where $E_K(C'C''C''')$ is the kinetic energy of the Auger transition involving electrons from $C'$, $C''$ and $C'''$ core levels, and $E_K(C)$ is the kinetic energy of the photoelectron from core level *C*. For rectifying negative value of $\alpha$, a widely modification was accepted as:

$$\alpha' = E_K(C'C''C''') + E_B(C)$$

Consideration upon the Auger transition in the atomic core, if the assumption of equal shifts in BE in all core levels involved in the definition of the Auger parameter is verified, then to a good approximation the AP shifts between two chemical states can be written as:

$$\Delta\alpha' = 2\Delta R^{ea}$$

Where $\Delta R^{ea}$ describes the extra-atomic relaxation or polarization perturbation coming from the neighbor ligand of the core-ionized atom. If the shifts are calculated with respect to the free atom or the free ion we can write $\Delta\alpha' = 2\Delta R^{ea} = 2R^{ea}$ because for free atomic or ionic species there is no extra-atomic relaxation energy. To study related metal nanoparticles supported on certain substrates, the equation was always adopted to identify the "final state" effect. But attention must be paid to two issues: the assumption for AP $\Delta\alpha'$, and the meaning of absolute value $\Delta R^{ea}$. It is still a problem for verify exactly the assumption of "same shift for every core levels". And

for the meaning of absolute value $\Delta R^{ea}$, it is normally used in compound materials, and considers the comparison with bulk state of corresponding elements, in which different kinds of atomic force (valence electron mutual action) exists, for example, Ni and NiO.

To consider the first issue of assumption, Carlson[186] pointed out that AP , as defined by Wagner, is a valuable parameter with which to correlate chemical bonding. However, more studies on the comparative chemical shift of different core electrons in the same atom are need if, as he put it, the interpretation of AP is to be treated with complete confidence. Thus Lang and Williams[187] introduced the generalized AP, $\xi$ as:

$$\xi = E_B(C') - E_K(C'C''C''') - E_B(C'') - E_B(C''')$$

Hohlneicher et al.[188] proposed a similar equation if considering that two holes in the final state are in the same atomic orbital:

$$\beta = E_K(C'C''C'') - 2E_B(C'') - E_B(C')$$

Note that for particular case of $C'' = C'''$ there is a simple relationship between $\beta$ and $\xi$: $\xi = \beta$. Thus, in the condition, the generalized AP could be:

$$\Delta\beta = 2\Delta R(C'')$$

Since no assumption is made in this definition, the accurate value of relaxation energy could be obtained and the role of the "final state" effect in the size dependent BE shift of metal nanoclusters can be understood. Richter[37] and Bagus[169] have used the

generalized AP to calculate the relaxation energy for Ni and Ag nanoclusters. Especially, Bagus[169] has proved that the value obtained using the calculation of $\Delta\beta$ gives better precision than using the $\Delta\alpha'$.

In our work, we get the well description of size dependent BE shift for Ni nanoparticles using BOLS correlation, in which, the Hamilton perturbed by lattice constrain originating from imperfection of atomic CN at surface region dominates the BE shift. We should validate the conclusion by means of $\Delta\beta$ calculation for the "initial final state" effect without any assumption. Since two core levels are involved in the Auger process, it is critical to choose a reasonable BE to calculate the relaxation energy of $\Delta\beta/2$. In general, the Auger peak $E_K(MVV)$ is adopted, of which the valence band is involved. However, the valence band is influenced more easily by the ambient environment. Therefore, the Auger peak of $E_K(L_3M_{23}M_{23})$ for Ni is chosen to avoid the disadvantage of valance band involvement, as denoted by arrow in Figure 35. The data for the thinnest 0.27 ML is abandoned for difficult position confirmation due to weak peak intensity. With the increase of Ni coverage, the kinetic energy of Auger electrons shifts positively to high value. Combined the measurement of $E_K(L_3M_{23}M_{23})$ and adoption of generalize AP $\Delta\beta$, Figure 36 demonstrates the proportional comparison of "initial state" and "final state" effect of $\Delta R^{ea}$ in the total BEs of Ni $3p_{3/2}$ BE as a function of Ni coverage. The relaxation energy is smaller than 0.1 eV, and hence, could be negligible. Thus, the contribution of 'initial state' effect is determinative absolutely compared with the whole BE shift of Ni $3p_{3/2}$ BE. Similar

conclusion could be rational to draw for the $2p_{3/2}$ peak if deeper Auger peak of $E_K(KLL)$ is available. An exclusion of the relaxation energy by the generalized AP is consistent with the expectation of the BOLS theory and Richter's proposal[37] as well, for the $2p_{3/2}$ and $3p_{3/2}$ BEs of Ni.

### 5.2.2.3 Conclusion

The size dependent BEs of Ni nanoparticles deposited on STO(100) surface has been investigated using XPS measurement. The positive BEs of Ni nanoparticles is ascribed to the skin depth quantum trapping which is induced by the surface bond contraction as expectation from BOLS correlation. A calculation of the generalized AP reveals that the contribution of 'initial state" effect is dominant to the entire BEs of Ni nanoparticles and relaxation energy arising from photoelectron emission process could be negligible.

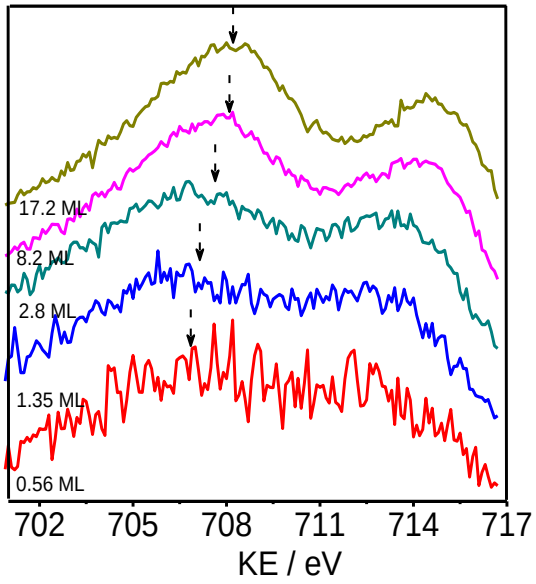


Figure 35 The Auger kinetic energy, $E_K(L_3M_{23}M_{23})$ (denoted as arrowed) as function of Ni coverage deposited onto STO(100) surface.

Table 7 The peak position for energy bands including Auger peak after peak fitting performed. The position with the highest intensity is recorded as VB peak position.

| Thickness(ML) | $2p_{3/2}$ (eV) | $3p_{3/2}$ | VB | $L_3M_{23}M_{23}$ | $L_3M_{45}M_{45}$ |
|---|---|---|---|---|---|
| 0.27 | 853.92 | 67.43 | 1.89 | ~ | 843.37 |
| 0.56 | 853.77 | 67.17 | 1.51 | 709.29 | 843.80 |
| 1.35 | 853.50 | 66.86 | 1.10 | 709.76 | 844.38 |
| 2.8 | 853.35 | 66.45 | 0.91 | 710.35 | 844.58 |
| 8.2 | 853.26 | 66.22 | 0.69 | 710.96 | 844.99 |
| 17.2 | 853.21 | 66.11 | 0.42 | 711.00 | 845.50 |

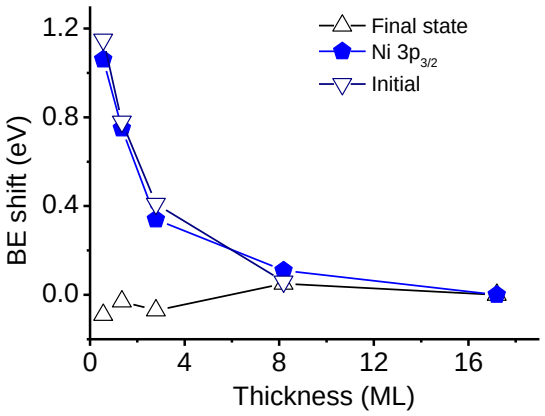


Figure 36 The Ni $3p_{3/2}$ BE shift in comparison to the "final state" effect of relaxation energy and the "initial state" effect.

# 5.3 Pt Nanoparticles on $SiO_2$/Si Substrate

## 5.3.1 Substrate Preparation

The size-induced BE shift is of particular interest as the Pt nanostructures is promising candidates for catalytic oxidation of carbon monoxide and nitric monoxide species. Using XPS measurement, Marcus et al.[177] and Yang et al.[189] have observed a ~0.6 eV positive shift from 71.1 eV for the bulk Pt to 71.7 eV for Pt nanoparticles deposited on carbon nanotubes. Yang et al.[190] found a ~+0.5 eV shift for Pt deposited on HOPG with a thickness of 0.4 monolayer; Bittencourt et al.[191] also reported a positive shift of 0.5 eV for $4f_{7/2}$ peak as the thickness of Pt nanoparticles on the CNT is around 0.2 nm. These observations showed clearly that size of Pt nanoparticles could induce positive BE shift.

In this study, TEM is adopted to measure the size of Pt nanoparticles deposited on $SiO_2$/Si substrate. Traditionally, specimen should be cut and lapped into certain thickness to fulfill the measurement condition of TEM. However, in the preparing process, contaminations and destructions for sample always have to be faced to. To avoid such disadvantage, the $SiO_2$/Si substrate is cut and lapped well for TEM measurement in advance before it is transferred into the preparation chamber for growth. After Pt deposition, it is measured directly using TEM without any cutting or lapping. Figure 37 shows the Si 2p spectrum of $SiO_2$/Si substrate where the $SiO_2$ is formed in ambient air. The peaks at 103 eV and 99 eV correspond the Si 2p state in $SiO_2$ and Si. A new peak locating at 101.20 eV is observed, which is assigned to the 2p state in SiO. The presentence of the SiO layer shows that the surface has not sufficient oxidization. The thickness of $SiO_2$/SiO layer is calculated as 4.2 nm, which is thin enough to avoid charging effect in the XPS measurement.

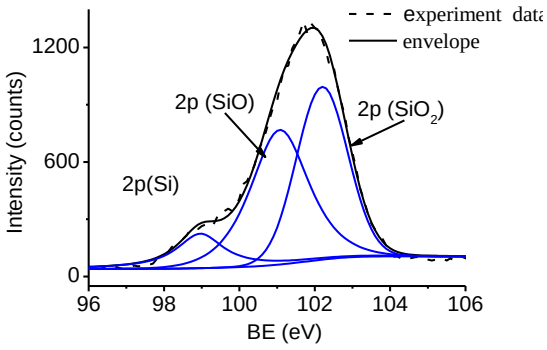


Figure 37 The Si 2p peak of clean $SiO_2$/Si surface. Three components including SiO, Si and $SiO_2$ are observed.

## 5.3.2 Results and Discussions

Figure 38 shows the TEM measurement for the Pt nanoparticles on $SiO_2$/Si substrate under different deposition time from 0.5 hours to 3.5 hours. According to 0.5 hours deposition time shown in Figure 38(a), the Pt nanoparticles have been formed on the substrate, which is very small around 1.0 nm in diameter. When the deposition time is prolonged to 1 hour, the Pt nanoparticles become bigger and the density of nanoparticles is increased. The dispersion of those nanoparticles is uniform, showing an isotropic growth of Pt on this substrate. With increasing the deposition time to 2h, 3h and 3.5 h, the Pt nanoparticles grow continuously and the average diameter of Pt nanoparticles increases to 2.8 nm finally. The size dispersion is worse than that in Figure 38(a) and (b). The detailed size measurements for different time are shown in Table 8. Figure 39 (a) shows the Pt $4f_{7/2}$ BE evolution as the diameter of nanaparticles increases from 1.02 nm to 2.89 nm. Obvious positive BE shift for Pt$4f_{7/2}$ core level is observed. To get accurate information of BE shift, Figure 39(b) demonstrates the peak fitting for the $4f_{7/2}$ peak: the background subtraction is performed in Shirley mode. We provide the comparison between the BOLS correlation prediction and our experimental data based on the accurate size measurement as shown in Table 8. In the BOLS convention,[64] CN of surface atom in three outermost layers is taken: $z_1 = 4$, and $z_2 = 6$, $z_3 = 12$, and consequently $c_1 = 0.88$, $c_2 = 0.94$, and $c_3 = 1$; m = 1 has been

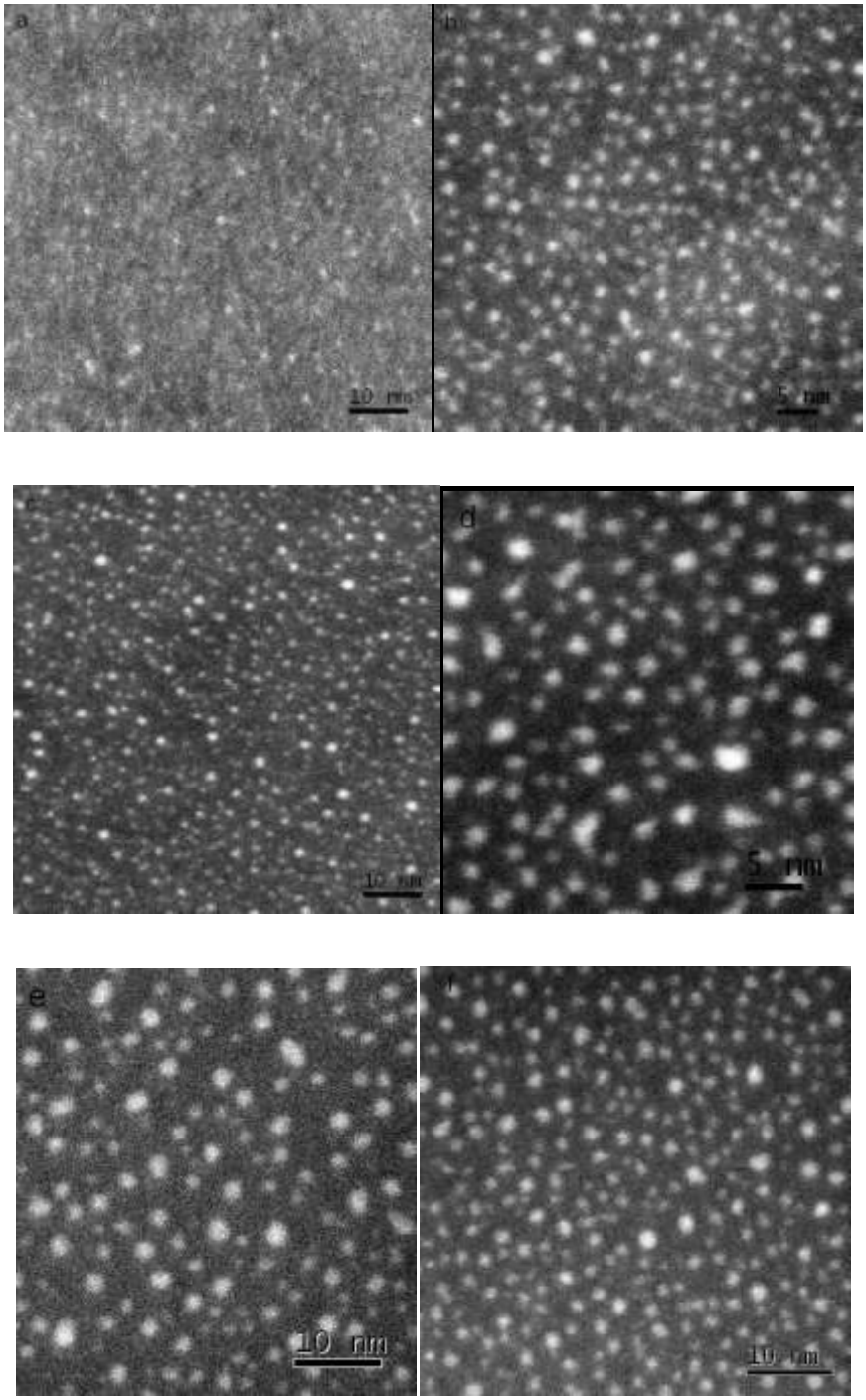


Figure 38 TEM measurement of Pt deposited on $SiO_2$/Si substrate at different deposition time(a)0.5 hour, (b)1hour, (c)1.5 hour, (d)2 hour, (e)3 hour, (f)3.5 hour.

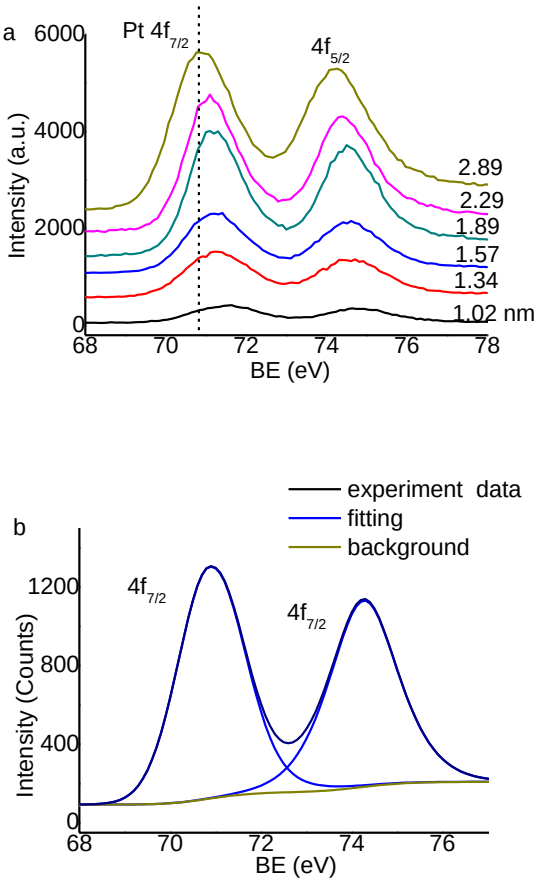


Figure 39 (a) The Pt 4f peak XPS measurement at different deposition time from 0.5hour to 3.5 hour. (b)The peak fitting of Pt 4f core level.

Table 8 The size dispersion of the Pt nanoparticles deposited on $SiO_2$/Si substrate at different deposition time and corresponded BE of Pt$4f_{7/2}$.

| Deposition time (hour) | 0.5 | 1 | 1.5 | 2 | 3 | 3.5 |
|---|---|---|---|---|---|---|
| Diameter(nm) | 1.02 | 1.34 | 1.57 | 1.89 | 2.29 | 2.95 |
| BE of $4f_{7/2}$(eV) | 71.47 | 71.29 | 71.20 | 71.08 | 70.99 | 70.91 |

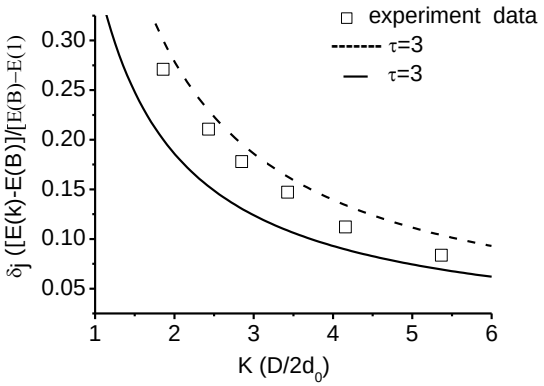


Figure 40 The comparison between the prediction of BOLS on the size dependent BE shift of Pt$4f_{7/2}$ core level and the experimental data. $\tau = 2, 3$ represent the 2D and 3D growth mode of Pt nanoparticles on $SiO_2$/Si substrates.

optimized in previous findings[47, 57] for the pure metal; as the Pt nanoparticles is a island growth mode on $SiO_2$/Si substrate, $\tau$ = 3 is adopted to describe the 3D morphology. In our previous publications,[192] we have reported that the BE of Pt $4f_{7/2}$ BE of an isolated Pt atom is 70.66 eV, and the BE shift $\Delta E(\infty)$ is 2.99 eV. Using those parameters, Figure 40 gives the fitting result for the experimental data by BOLS correlation. It should be noted that ratio of BE shift compared to $\Delta E(\infty)$ is set as the y- axis. In Figure 40, the experimental BE value is always lower than that by BOLS prediction as $\tau$ = 3 is adopted. This shows that the grow mode of Pt nanoparticles does not follow 3D rigidly. Another prediction curve from BOLS correlation with $\tau$ = 2 is given in the Figure 40. The experimental BE valued locates between the two curves of $\tau$ = 3 and $\tau$ = 2, which shows that the growth of Pt nanoparticles follows a mode which is in between 2D and 3D growth. The BOLS correlation could gives a reasonable prediction for the tendency of BE shift of Pt

nanoparticles, confirming that the CN imperfection in the surface region of Pt nanoparticles is the key reason for the size dependent BE shift.

### 5.3.3 Conclusion

Pt nanoparticles have been synthesized on the $SiO_2$/Si substrate and XPS measurement has been performed. A positive BE shift is observed as the diameter of Pt nanoparticles decreases from 2.9 nm to 1.0 nm. The origin for the size dependent BE shift is discussed based on the BOLS correlation. The atomic CN imperfection at the surface region of Pt nanoparticles is the key factor according to the BE shift. From BOLS correlation, it has been found that the growth mode of Pt nanoparticles follows a quasi-3D growth mode rather than rigid 3D growth.

## 5.4 Cu Nanoparticles on STO Substrates

### 5.4.1 Substrate Preparation

Commercial STO substrates has been cleaned by acetone and diluted water before it is transferred to the preparation chamber for the copper growth. The copper nanoparticles were deposited by the e-beam evaporator in a high vacuum circumstance using the copper rod with the purity of 99.999%. As cleaned STO substrates are annealed to 773K to clean the adsorbed gas and recover the surface, which causes the color of STO substrate turn to the dark gray. Figure 41 shows the

spectra comparison of Sr 3d peak from both (100) and (111) substrates. There is no obvious difference between two 3d peaks.

## 5.4.2 Results and Discussions

Cu nanoparticles are deposited on STO(100) substrate with growth time from 2 minutes to 62 minutes and on STO(111) substrate with that from 30 seconds to 67 minutes. As shown in Figure 42a, for Cu deposited on (100) surface, the obvious BE

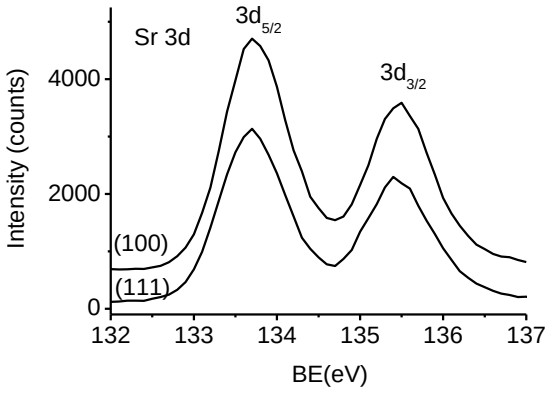


Figure 41 The comparison of Sr 3d core level from STO(100) surface and (111) surface.

shift of Cu $2p_{3/2}$ peak is observed. With the deposition time increases from 2 minutes to 62 minutes, the BE of Cu $2p_{3/2}$ decreases from 933.41 eV to 933.01 eV. For Cu deposited on STO(111) substrate as shown in Figure 42b, with the deposition time increases from 30 seconds to 67 minutes, the bigger magnitude of BE shift varies from 933.69 eV to 933.0 eV. The BEs of Cu $2p_{3/2}$ peak on both substrates after 60 mins deposition attain to 933 eV which has been confirmed as the value of Cu bulk state.

Figure 43 gives the valence band(VB) evolution for Cu deposited on STO(100) and (111) substrates with different growth time. For two clean substrates, two obvious peaks are observed around 6.5 eV and 4.5 eV. As the copper is deposited on with 30 seconds of deposition time, a weak new peak shows at end of lower BE at 4.5 eV, corresponding to the new VB of Cu nanoparticles. With increasing the deposition time, the main peak of VB shifts to the BE of 2 eV, accompanying the peak intensity enhancement. Meanwhile, the peak representing the VB of clean STO substrates disappear gradually since the increased thickness of Cu nanoparticles. In Figure 43, the interaction between the overlayer copper nanoparticles and the two substrates could not be differentiated in the VB spectrum because of the overlapping between the VB of two constituents.

The thickness of the copper film has been calculated using the equation as follows:

$$I(t) = I(\infty)[1 - \exp\left(\frac{-t}{\lambda_{Cu} sin\theta}\right)]$$

Where the $\lambda_{Cu}$ is the inelastic mean free path of Cu electron in copper crystal.[193] $\theta$ is the take-off angle. $I(t)$ and $I(\infty)$ represents the Cu $2p_{3/2}$ peak intensity of nanoparticles and bulk, respectively. The thickness of Cu film is in units of equivalent monolayer where one monolayer is defined as the same package of Cu(111) surface.( $0.9 \times 10^{14} \frac{\text{atom}}{\text{cm}^2}$ ), around 0.23 nm. In the experiment, the copper nanoparticles formed on both substrates shows a obvious BE shift as the variation of deposition time as shown in Table 9, coinciding with amounts of reports[180,

194-197]. However, the origin for the BE shift as the size variation is still under argument. BOLS correlation proposed that the local quantum trapping induced by the local surface modification with spontaneous bond contraction induces the perturbation to the Hamiltonian of entire specimen, which eventually results in the BE shift of nanosolids. To verify this deduction, we do the comparison between the

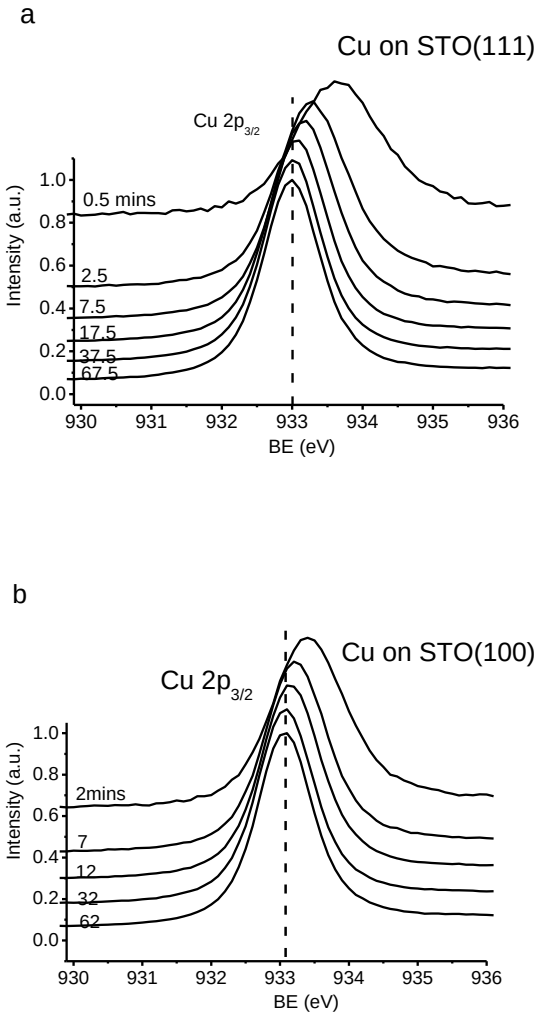


Figure 42 The BE evolution of Cu $2p_{3/2}$ peak on (a) STO(100), (b) STO(111) surfaces with different deposition time presented in figure.

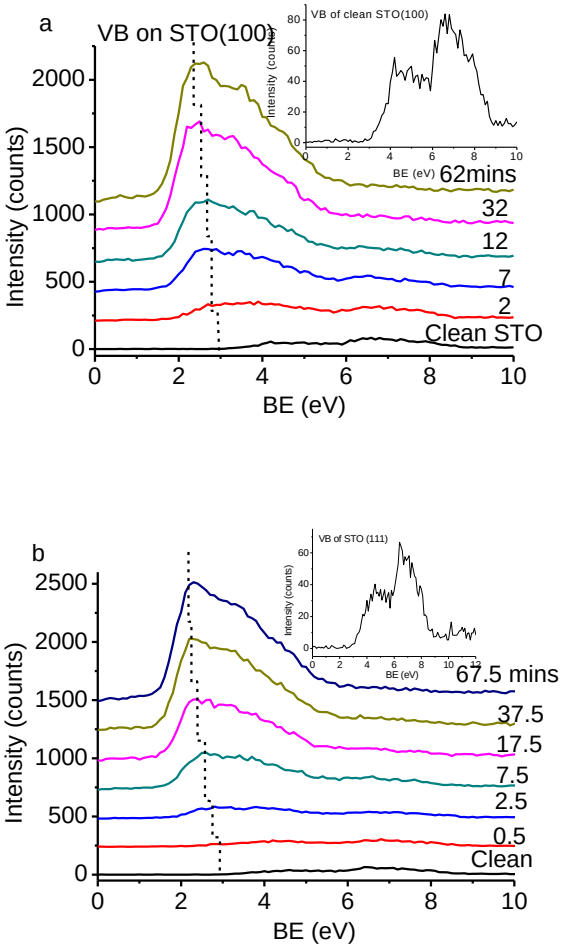


Figure 43 The valence band evolution of Cu nanoparticles on (a) STO(100), (b) STO(111) surfaces. The insert is the valence band of clean STO(100) and (111) surface.

Table 9 The BE shift of $2p_{3/2}$ for Cu on STO(100) and (111) substrates with different film thickness.

| Cu /STO(100) | | Cu /STO(111) | |
|---|---|---|---|
| Thickness/ML | BE of Cu $2p_{3/2}$/eV | Thickness/ML | BE of Cu $2p_{3/2}$/eV |
| 0.50 | 933.69 | 0.83 | 933.41 |
| 1.19 | 933.25 | 2.10 | 933.17 |
| 1.51 | 933.16 | 2.57 | 933.11 |
| 3.00 | 933.07 | 4.50 | 933.04 |
| 4.95 | 933.02 | 8.42 | 933.01 |
| 7.53 | 933.01 | | |

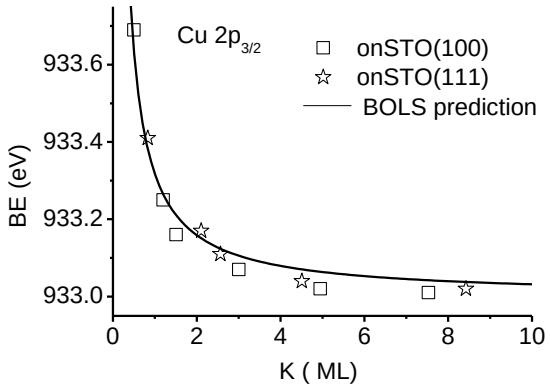


Figure 44 The BOLS prediction on the Cu nanoparticles deposited on STO(100) and (111) surface.

BOLS prediction and the experiment results. In the BOLS convention,[64] coordination number of surface atom in three outermost layers is taken: $z_1 = 4$, and $z_2 = 6$, $z_3 = 12$, thus bond contraction follows as: $c_1 = 0.88$, $c_2 = 0.94$, and $c_3 = 1$; $m = 1$ (for metals) has been optimized in previous findings[47, 57]; parameter $\tau = 1$ describes the one dimensionality of Cu nanoparticles because the thickness of 'ML' is

adopted, while the morphology of Cu deposited on STO(100) surface has been reported in three dimensional island[179, 180] or multi-layer[181, 182](semi three dimensional island) structure. Using the different thickness and Eq.35 in BOLS correlation, the BE shift of $2p_{3/2}$ between an isolated Cu atom ($E_v(1)$) and the bulk counterpart has been gained as 1.7 eV, coinciding with our previous report.[178] The BE of $2p_{3/2}$ for an isolated Cu atom is 931.3 eV. Figure 44 shows the comparison between the experimental data and the BOLS prediction for Cu $2p_{3/2}$ size dependent(thickness) BE shift. The BOLS prediction gives a reasonable description for the BE shift, confirming the proposal that the local quantum trapping induced by the under-coordinated surface of nanosolids is the origin for the energy shift.

### 5.4.3 Conclusion

The BE of Cu nanoparticles deposited on STO(100) and (111) surface has been investigated by XPS measurement. Using the BOLS correlation, the BE of an isolated Cu atom and the intrinsic bulk shift have been gained as 931.3 eV and 1.7 eV, respectively. The well coincidence between BOLS prediction and experimental result confirmed that the local quantum trapping in the surface region of Cu nanoparticles induced by the surface band contraction and bond energy enhancement shifts the position of every energy band including VB and core levels.

## 5.5 Conclusion

In this chapter, The BE shift of metal nanoparticles has been investigated by the in-situ XPS measurement. According to the Ni nanoparticles on $SiO_2$/Si substrates, TEM measurement is performed to gain the accurate size distribution. It found that Ni nanoparticles follows island growth mode and a worse size distribution presents at long deposition time. An obvious positive BE shift of Ni nanoparticles is observed as the size decreased from 6.9 nm to 0.5 nm in radius. The similar positive BE shift is also observed for Cu nanoparticles deposited on the STO(100) and (111) substrates. Pt nanoparticles deposited on $SiO_2$/Si substrates is investigated by TEM and XPS measurements. The Pt $4f_{7/2}$ peak energy shifts from 70.91 eV to 71.47 eV as the radius decreases from 2.95 nm to 1.02 nm. BOLS correlation ascribes the size dependent BE shift of Ni, Cu and Pt nanoparticles to the modification of atomic CN. It has deduced that the bond between the shorter and stronger bond between under-coordinated atoms in the surface region of metal nanoparticles induces the local crystal potential well to be deepened. The modification in the local crystal potential will provides a perturbation to the Hamiltonian of entire nanoparticles, finally cause the BE shift toward high absolute value. The well coincidence between the theoretical prediction and the experimental data confirms the conclusion of BOLS correlation that the local quantum trapping is the key factor taking effect on the size dependent BE shift of metal nanoparticles.

# Chapter 6 Impurities and Interfaces: Catalyst and Diffusion Barrier

## 6.1 Introduction

Atomic impurities, interfaces of superlattices, twin grains, and embedded nanostructures can be prototyped by an atom with fully or partially coordinated heterogeneous neighbors. Many processes take place surrounding such atoms: the alloy formation associated with valence charge intermixing; compound formation with valence electron localization, repopulation, and polarization; structure distortion due to lattice mismatching, etc. Joining two materials may result in a new value of melting point ($T_m$), or the cohesive energy per discrete atom, being different from that of either of the constituents standing alone.[57, 198] The strength of junction interface is frequent much stronger (mechanical strength is proportional to the sum of bond energy per unit volume[74]) than either component alone, which forms the basis of superhard multilayers or stiffer nanocomposites.[199, 200] Strain and chemical energy arising from the interface bond strain and bond nature alteration,[73] are often used to describe the interface energy.[198, 201] Interface produces locally large perturbations to the Hamiltonian, BE density, and atomic cohesive energy, which determine the mechanical, thermal, electronic, optic, magnetic, dielectric, catalytic and chemical properties which are completely different from those of the constituent bulk

metals.[202-204] It has been asserted that ”no strain, no gain” for the FePd epitaxial interface,[205] for instance.

The study of surface or interface alloying is motivated by their use in many industrial applications such as catalysis, sensors, anticorrosion, friction reduction, and electronic devices. Varying composition or thermal annealing upon continuous deposition of dissimilar metals[116, 206] has provided an effective method to modify interatomic strain and to redistribute charges around the bonding atoms.[207, 208] Although the physics and chemistry of materials at the interfaces have been extensively investigated, the laws governing the energetic behavior of electrons and the property change of materials at the interface have not yet established. This work aims to show that the charge and energy quantum trapping (QT) is necessary for the CuPd bimetallic interface.

## 6.2 The Principle of Interface Quantum Entrapment

Figure 45a illustrates the proposed interface QT mechanism. In the interface region, there is a gradient of chemical composition due to the diffusion of the constituent atoms. $E_0$ is the vacuum level; $V_{atom}(r)$ is the potential of intra-atomic trapping. Including the many-body interaction, $V_{cry}(r, B)$ represents the periodic interatomic potential experienced by electrons in the constituent bulk (B). Moving cross the interface region from one to the other constituent, the $V_{cry}(r, B)$ evolves into $V_{cry}(r, I)$

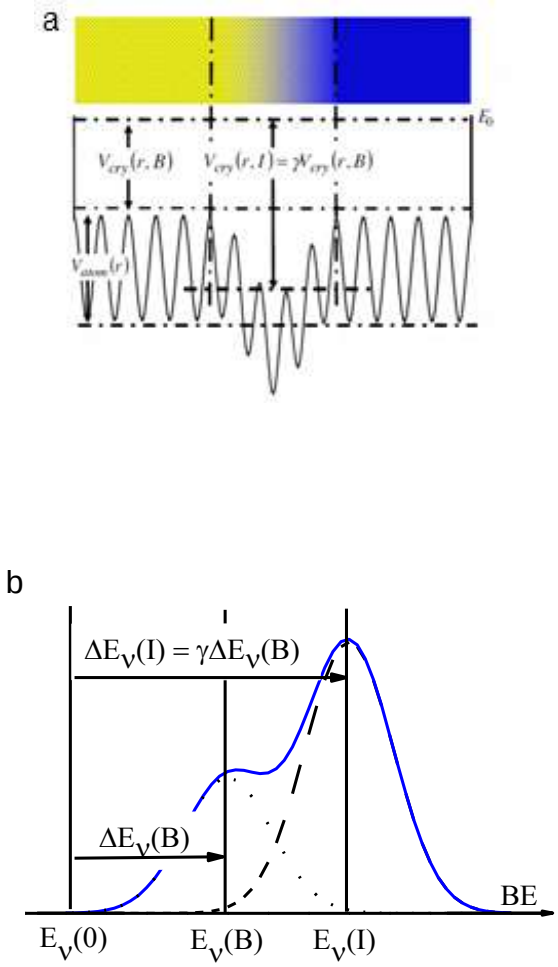


Figure 45 Schematic illustration of (a) the QT model and (b) the QT-induced core-level shift, $\Delta E_v(I)$ and $\Delta E_v$ (B) from the energy level of an isolated atom, $E_v(1)$, $V_{atom}(r)$ is the intraatomic potential. $V_{cry}(r, B)$ and $V_{cry}(r, I)$ are interatomic potentials in the bulk and the interface region, respectively. $\gamma$ is the enhance parameter. $\gamma > 1$ represents the compact and $\gamma < 1$ represents the dissociated interface. Annealing will increases the $\Delta E_v(I)$ intensity, rendering that of the $\Delta E_v(B)$, upon alloy formation.

at the middle of the interface (I) because of valence charge intermixing or bond nature alteration. The coefficient $\gamma$ shown in Figure 45a represents the interface bond-energy ratio to that of the constituent bulk. The $V_{cry}(r, I)$ may be deeper ($\gamma > 1$) or shallower ($\gamma < 1$) than the corresponding $V_{cry}(r, B)$ for a specific constituent. If dipole is produced in the interface region,[72] $\gamma < 1$; otherwise, $\gamma > 1$. In the present study, we will focus on the case of $\gamma > 1$.

According to the tight-binding theory[128] and the BOLS correlation, in the interface region, both the atomic CN z and the Bloch wave function are changed insignificantly, the BE shift is thus uniquely determined by the perturbed potential well depth or the bond energy,

$$\frac{\Delta E_v(I)}{\Delta E_v(B)} = \gamma = 1 + \Delta_H$$

or

$$\frac{\Delta E_v(I) - \Delta E_v(B)}{\Delta E_v(B)} = \Delta_H = \gamma - 1$$

Based on this expression, we can determine the interface bond strength based on the XPS decomposition of the $\Delta E_v(B)$ and the $\Delta E_v(I) - \Delta E_v(B)$, as illustrated in Figure 45b. It is expected that the intensities for the peaks $\mathrm{E_v(I)}$ and $\mathrm{E_v(B)}$ evolve upon annealing; the intensity of $E_v(I)$ peak will increase rendering that of $\Delta E_v(I)$ as the total number of electrons in the particular band conserves. The intensity evolution reflects the extent of alloy formation.

# 6.3 Results and Discussions

In order to verify the proposed mechanism of interface QT, Cu(2 nm)/Pd(10 nm) thin films were firstly deposited onto Si wafer using a physical–vapor–deposition system.[116] XPS spectra were collected then as a function of isochronal annealing (1 min) at increasingly high temperature up to 940 K (with XPS spectra being recorded on cooling to 300 K). Each spectrum was decomposed into two components,

$E_v(I)$ and $E_v(B)$, as summarized in Table 10. At room temperature, no significant fingerprints of alloy formation (peak I) were observed but with the increase of annealing temperature, additional peaks emerge at energies of 1.62 eV below the Cu $2p_{3/2}$ and 1.57 eV below that of Pd $3d_{5/2}$. As the annealing temperature keeps on increasing, intensities of the $E_v(I)$ peak increase rendering that of $E_v(B)$.

Figure 46 shows the typical Cu $2p_{3/2}$ and Pd $3d_{5/2}$ spectra collected after 540K and 940 K annealing. The intensity reversions of the $E_v(I)$ and the $E_v(B)$ at 540K and 940 K indicate the completeness of interface alloying. In addition, low-energy electron and photoelectron diffraction studies[209, 210] revealed that the Cu-Pd interlayer distance contracts up to 7 ± 2.5%. The interface alloy is formed through atomic interdiffusion[211] with an estimated activation energy of 0.88 eV.[212, 213] A theoretical reproduction[64] of the measured size dependence of Cu $2p_{3/2}$[162] and Pd $3d_{5/2}$ surface [114] BE shift has derived that the $\Delta E_v(B)$ for Cu $2p_{3/2}$ and Pd $3d_{5/2}$ are 1.70 and 4.36 eV. These data allows us to estimate the interface potential-well depth for the Pd 3d and Cu 2p electrons with the resolved $\Delta E_v(I)$-$\Delta E_v(B)$ as given in Table 10. Calculation results in Table 11 indicate that the γ values for Pd and Cu are 1.36 and 1.95, respectively. The corresponding BE shift are 5.93 eV and 3.32 eV in comparison to the bulk shift of 4.36 eV and 1.70 eV for the Pd 3d and the Cu 2p levels in the interface region. Apparently, such a huge energy shift due to alloy formation is beyond the description of the well-received "initial-final" states or the

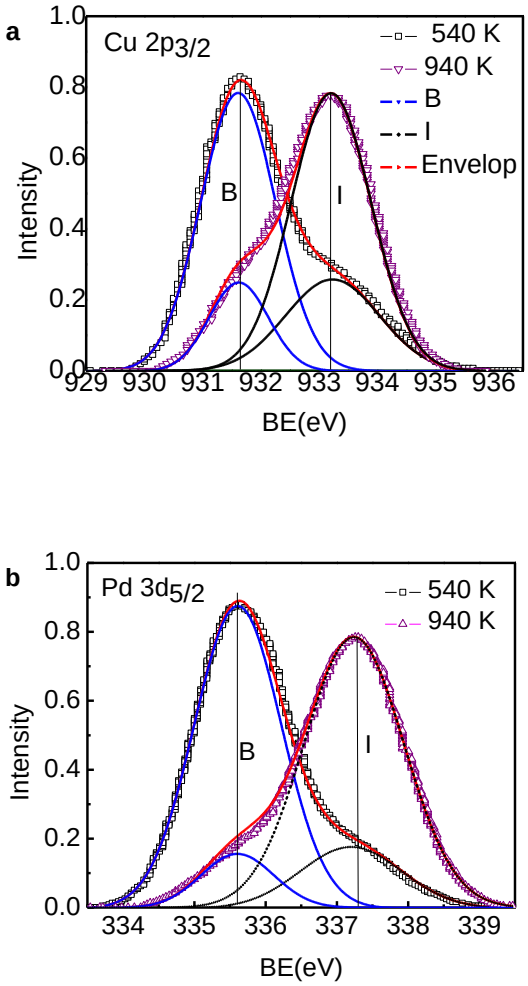


Figure 46 Thermally-driven spectral evolution of (a) Cu $2p_{3/2}$ and (b) Pd $3d_{5/2}$ BE upon annealing at 540 K and 940 K and their decompositions.

"hole screening" mechanism[214] that comes into play throughout the measurement and hardly sheds the alloying effect.

The interface QT mechanism agrees with the proposal of a wedge-shaped potential well for the monolayer structure sandwiched between the $SrTiO_3$ and the $LaTiO_3$ superlattices in calculations.[215] The QT was suggested to arise from the Coulomb potential of a two-dimensional charged La sheet, which in turn confines the

electrons in the Airy-function-localized states. Here we suggest that the interface QT arises from the bond strain[209, 210] and valence charge intermixing. As a consequence of the QT, energy levels of atoms in the interface region will go deeper or shift positively, accordingly.

On the other hand, the interfacial atomic cohesive energy, $E_{C,I} = \gamma z E_b$, will increases as the cohesive energy per bond increases from the bulk value of $E_b$ to $E_I = \gamma E_b$ and the z changes insignificantly.[57] The $E_{C,I}$ determines the $T_m$ uniquely. Therefore, the interface QT can be further verified by the observed size dependence of overheating of embedded nanostructures. A theoretical analysis[75] of the size-induced overheating for Ag/Ni, and Pb/Al and Pb/Zn core-shell nanostructures has led to a $\gamma$ =1.8 for the Ag and Pb cores, indicating that an interfacial bond is 80% stronger than a bond in the bulk of the core material, which is in line with the current derivation of $\gamma > 1$ for the CuPd interface.

# 6.4 Conclusion

We have thus demonstrated that the interface charge and energy QT is essential for the Cu-Pd interface and that the trap depth is, respectively, 1.36 and 1.95 times that of the bulk Pd and Cu. The QT arises from the interface bond order distortion and valence charge intermixing that perturbs the Hamiltonian, the atomic cohesive energy, and hence the related properties. This approach not only provides a feasible way of interface bond strength determination but also a consistent insight into the energetic

behavior of electrons in the interface region. This straight forward yet simple method can be used to extract information regarding the local energy and charge of other interfaces or bimetallic alloys.

Table 10 XPS measured intensity (I) evolution of Pd $3d_{5/2}$ and Cu $2p_{3/2}$ BE (BE) at the Cu(2nm)-Pd(10 nm) interface as a function of annealing temperature, T.

| T(K) | Pd $3d_{5/2}$(eV) | | | Cu $2p_{3/2}$ (eV) | | |
|---|---|---|---|---|---|---|
| | Bulk | Interface | $I_B/I_I$ | Bulk | Interface | $I_B/I_I$ |
| 340 | 335.67 | 337.10 | 15.30 | 931.65 | 933.20 | 11.50 |
| 540 | 335.66 | 337.17 | 5.06 | 931.57 | 933.21 | 2.93 |
| 573 | 335.63 | 337.19 | 4.78 | 931.62 | 933.30 | 3.23 |
| 673 | 335.58 | 337.22 | 1.56 | 931.60 | 933.30 | 1.40 |
| 940 | 335.58 | 337.26 | 0.18 | 931.65 | 933.19 | 0.282 |
| mean | 335.62 | 337.19 | - | 931.61 | 933.23 | - |

Table 11 Summary of the relative depths $\gamma$ and the interface energy shift $\Delta E(I)$ for the Pd $3d_{5/2}$ and Cu $2p_{3/2}$ BEs.

| E-level (eV) | $\Delta E_v(B)$ | $E_v(1)$ | $\Delta E_v(I)-\Delta E_v(B)$ | $\gamma$ | $\Delta E_v(I)$ |
|---|---|---|---|---|---|
| Pd $3d_{5/2}$[114] | 4.36 | 330.34 | 1.57 | 1.36 | 5.93 |
| Cu $2p_{3/2}$ [64, 162] | 1.70 | 931.00 | 1.62 | 1.95 | 3.32 |

# Chapter 7 Conclusions and Recommendation

## 7.1 Achievement

The behavior of bond and electrons in under-coordinated system has been investigated mainly using the XPS measurement. The size, surface layer and orientation, terrace edge, adatoms and vacancies dependent BE shift have been found in our experiments. BOLS correlation ascribes the BE shift to the Hamiltonian perturbation and the as inspired electron and energy polarization. In BOLS correlation, it has been confirmed that with the coordination number decreasing the remaining bond contracts spontaneous and single bond energy is enhanced. The bond modification enables local crystal potential to be deepened and narrowed, which induce a local quantum trapping for the electrons within the region. As a result, the Hamiltonian of entire sample is influenced by the local quantum entrapment. In the process of electronic structure modification, a new effect is created. The narrowed local potential will polarized other electrons which locate in the upper bands to a new orbital, forming a extra state of polarization. The combination and the competition between the Polarization state and quantum entrapment result in BE shift in aforementioned under-coordinated systems and affect their performance in the catalytic, electro-affinity, work function, band gap, etc. A new method of APSD has been proposed to promote the traditional XPS measurement by zooming in the bond and electrons within the atomic patches surrounding the under-coordinated and

hetero-coordinated atoms in single crystal surface, terrace edge, adatoms and vacancies.

The consistency between theoretical predication from BOLS correlation and our experimental measurements promote our understanding on the nature of atoms and bonds in under-coordinated system. Theoretical analysis has enabled the determination of the length and strength of the representative bond and the energy levels of an isolated atom and the bulk shift of the BE, the local BE density, atomic cohesive energy within the atomic patches of the following specimens.

i. The surface atomic layers and orientations induce obvious BE shift compared with that of bulk interior. The spectra of surface atomic layer of single crystals including W(*bcc*), Pd and Rh(*fcc*), Ru, Be, and Re (*hcp*) have been decomposed. Based on the decomposition and BOLS correlation, the BE of isolated atoms and bulk shift of corresponding substances were gained, which provided a constant reference for the energetic level evolution in other reactions and conditions. A minor difference in BE value of the same surface layers in a identical sample has been observed, which shows a surface orientation dependent BE shift.

ii. The new states on terrace edge, adatoms and vacancies have been observed using APSD treatment after accurate XPS measurement. Local quantum trapping state and polarization state always exists in those

under-coordinated system. The combination and the competition between local quantum trapping state and polarization state determine the trend of BE shift of entire sample, as well its performance.

iii. Size dependent BE shift has been observed in Ni, Cu and Pt nanoparticles deposited on different substrates. Similar trend of BE shift has been ascribed to the coordination environment in those metal nanoparticles.

Experimental and theoretical analysis confirm the perturbation to the Hamiltonian arising from the skin-depth local strain and potential well quantum trapping which are induced by the shorter and stronger bonds between ill-coordinated atoms, and associated charge and energy polarization which are induced by the localized quantum entrapment.

## 7.2 Limitations

The electronic energy level of under-coordinated system in this work were measured mainly by *in-situ* XPS, however, the experimental conditions maybe affects the data precision. For example, since the X-ray is a beamline with high energy which excites the electrons and secondary electrons, an unexpected local heat in the measurement maybe takes effect on the sample surface and modified the electronic structure and crystal enthalpy. The cooling system should be adopted on the sample to delay or dilute the as-induced modifications. Furthermore, the state of facilities will also affect the data analysis.

## 7.3 Recommendations

### 7.3.1 The Combination of STM and XPS Measurement.

STM/S is a very useful tool to examine the local electronic configuration near several eV below or above Fermi energy. It had a good resolution of 0.1nm in lateral length and 0.01nm in depth. With the resolution, individual atoms within materials are routinely imaged and manipulated. It also provides the detailed local density of state and the atomic bonding information. However, the detected volume of STM is mainly localized on the outermost surface layer, the information underneath the surface layer and the interaction between the surface layer and the inner atomic layers could not be given by STM alone. Thus, the combination of STM and XPS in one system is necessary to study the holographic information of the under-coordinated system which are very brittle in the sample transferring and are easily contaminated.

### 7.3.2 Performance of Under-coordinated System

The BOLS correlation provides an effective way to understand the behavior of bond and electrons in under-coordinated system. Actually, not only the electronic behavior varies in the system, but also other properties such as magnetic, thermal dynamics and mechanics. Thus, the new performance of the under-coordinated system especially the defects vacancy would be of great interest.

# List of Publications

1. **Nie, Y.G.**, Xi Zhang, Shouzhi Ma, Yan Wang, Jisheng Pan, Chang Q Sun, "Undercoordination-induced quantum entrapment and polarization making tungsten terrace-edge atoms potentially donor-type catalyst". *Physical Chemistry Chemical Physics*, DOI: 10.1039/c1cp21421g.

2. **Nie, Y.G**., Jisheng Pan, Weitao Zheng, Ji Zhou, Chang Q Sun, " Atomic scale purification of Re surface kink states with and without oxygen chemisorption". *The Journal of Physical Chemistry C*, 115, 7450

3. **Nie, Y.G.;** Pan, J.; Zhang, Z.; Chai, J.; Wang, S.; Yang, C. S.; Li, D.; Sun, C. Q., Size dependent 2p3/2 binding-energy shift of Ni nanoclusters on SiO2 support: Skin-depth local strain and quantum trapping. *Applied Surface Science* 2010, 256 (14), 4667-4671.

4. **Nie, Y.G.;** Wang, Y.; Sun, Y.; Pan, J. S.; Mehta, B. R.; Khanuja, M.; Shivaprasad, S. M.; Sun, C. Q., CuPd interface charge and energy quantum entrapment: A tight-binding and XPS investigation. *Applied Surface Science* 2010, 257 (3), 727-730.

5. **Nie, Y.G.**, Xi Zhang, Jisheng Pan, Weitao Zheng, Chang Q Sun, " Sub-nanoscale purification of the Graphitic Dirac-Fermi Polarons Using Photoelectron Residual Spectroscopy" (Under communicated)

6. Wang, Y.; **Nie, Y.G.**; Wang, L. L.; Sun, C. Q., Atomic-Layer- and Crystal-Orientation-Resolved 3d(5/2) BE Shift of Ru(0001) and Ru(1010) Surfaces. *Journal of Physical Chemistry C* 2010, 114 (2), 1226-1230.

7. Wang, Y.; **Nie, Y.G.**; Pan, J. S.; Pan, L. K.; Sun, Z.; Wang, L. L.; Sun, C. Q., Orientation-resolved 3d(5/2) BE shift of Rh and Pd surfaces: anisotropy of the skin-depth lattice strain and quantum trapping. *Physical Chemistry Chemical Physics* 2010, 12 (9), 2177-2182.

8. Wang, Y.; **Nie, Y.G.**; Pan, J. S.; Pan, L.; Sun, Z.; Sun, C. Q., Layer and orientation resolved bond relaxation and quantum entrapment of charge and energy at Be surfaces. *Physical Chemistry Chemical Physics* 2010, 12, 12753-12759.

9. Wang, Y.; **Nie, Y.G.**; Pan, L. K.; Sun, Z.; Sun, C. Q., Potential barrier generation at the BeW interface blocking thermonuclear radiation. *Applied Surface Science* 2011, 257 (8), 3603-3606.

10.Chen, H. Y.; **Nie, Y.G.**; Wang, L. J.; Zhang, J. H.; Dong, F. X.; Dai, Q. Q.; Lu, H. L.; Gao, S. Y.; Li, D. M.; Kan, S. H.; Zou, G. T., A general method for fabricating nanorods. *Nanotechnology* 2006, 17 (13), 3144-3148.

11.Sun, C. Q.; Sun, Y.; **Ni, Y.G.**; Zhang, X.; Pan, J. S.; Wang, X. H.; Zhou, J.; Li, L. T.; Zheng, W. T.; Yu, S. S.; Pan, L. K.; Sun, Z., Coulomb Repulsion at the Nanometer-Sized Contact: A Force Driving Superhydrophobicity, Superfluidity, Superlubricity, and Supersolidity. *Journal of Physical Chemistry C* 2009, 113 (46), 20009-20019.

12. Sun, C. Q.; Sun, Y.; **Nie, Y.G.**; Wang, Y.; Pan, J. S.; Ouyang, G.; Pan, L. K.; Sun, Z., Coordination-Resolved C-C Bond Length and the C 1s BE of Carbon Allotropes and the Effective Atomic Coordination of the Few-Layer Graphene. *Journal of Physical Chemistry C* 2009, 113 (37), 16464-16467.

13. Sun, C. Q.; Wang, Y.; **Nie, Y.G.**; Sun, Y.; Pan, J.; Pan, L.; Sun, Z., Adatoms-Induced Local Bond Contraction, Quantum Trap Depression, and Charge Polarization at Pt and Rh Surfaces. The *Journal of Physical Chemistry C* 2009, 113 (52), 21889-21894.

14. Sun, C. Q.; Wang, Y.; **Nie, Y.G.**; Mehta, B. R.; Khanuja, M.; Shivaprasad, S. M.; Sun, Y.; Pan, J. S.; Pan, L. K.; Sun, Z., Interface quantum trap depression and charge polarization in the CuPd and AgPd bimetallic alloy catalysts. *Physical Chemistry Chemical Physics* 2010, 12 (13), 3131-3135.

# References


1. Wang, D.W., Y.L. Chang, Q. Wang, J. Cao, D.B. Farmer, R.G. Gordon, and H.J. Dai, *Surface chemistry and electrical properties of germanium nanowires.* Journal of the American Chemical Society, 2004, **126**, 11602.
2. Long, C.G., J.D. Gilbertson, G. Vijayaraghavan, K.J. Stevenson, C.J. Pursell, and B.D. Chandler, *Kinetic evaluation of highly active supported gold catalysts prepared from monolayer-protected clusters: An experimental Michaelis-Menten approach for determining the oxygen binding constant during CO oxidation catalysis.* Journal of the American Chemical Society, 2008, **130**, 10103.
3. Lee, S.W., S. Chen, J. Suntivich, K. Sasaki, R.R. Adzic, and Y. Shao-Horn, *Role of Surface Steps of Pt Nanoparticles on the Electrochemical Activity for Oxygen Reduction.* The Journal of Physical Chemistry Letters, 2010, **1**, 1316.
4. Wei, Q.S., K. Tajima, Y.J. Tong, S. Ye, and K. Hashimoto, *Surface-Segregated Monolayers: A New Type of Ordered Monolayer for Surface Modification of Organic Semiconductors.* Journal of the American Chemical Society, 2009, **131**, 17597.
5. Koch, N., A. Gerlach, S. Duhm, H. Glowatzki, G. Heimel, A. Vollmer, Y. Sakamoto, T. Suzuki, J. Zegenhagen, J.P. Rabe, and F. Schreiber, *Adsorption-induced intramolecular dipole: Correlating molecular conformation and interface electronic structure.* Journal of the American Chemical Society, 2008, **130**, 7300.
6. Kravchuk, T., L. Vattuone, L. Burkholder, W.T. Tysoe, and M. Rocca, *Ethylene decomposition at undercoordinated sites on Cu(410).* Journal of the American Chemical Society, 2008, **130**, 12552.
7. Seitz, O., A. Vilan, H. Cohen, C. Chan, J. Hwang, A. Kahn, and D. Cahen, *Effect of doping on electronic transport through molecular monolayer junctions.* Journal of the American Chemical Society, 2007, **129**, 7494.
8. Blackstock, J.J., C.L. Donley, W.F. Stickle, D.A.A. Ohlberg, J.J. Yang, D.R. Stewart, and R.S. Williams, *Oxide and carbide formation at titanium/organic monolayer interfaces.* Journal of the American Chemical Society, 2008, **130**, 4041.
9. He, T., H.J. Ding, N. Peor, M. Lu, D.A. Corley, B. Chen, Y. Ofir, Y.L. Gao, S. Yitzchaik, and J.M. Tour, *Silicon/molecule interfacial electronic modifications.* Journal of the American Chemical Society, 2008, **130**, 1699.
10. Paneru, M., C. Priest, R. Sedev, and J. Ralston, *Static and Dynamic Electrowetting of an Ionic Liquid in a Solid/Liquid/Liquid System.* Journal of the American Chemical Society, 2010, **132**, 8301.
11. Ricci, D.A., T. Miller, and T.C. Chiang, *Controlling the Thermal Stability of Thin Films by Interfacial Engineering.* Physical Review Letters 2005, **95**, 266101.
12. Girit, C.O., J.C. Meyer, R. Erni, M.D. Rossell, C. Kisielowski, L. Yang, C.H. Park, M.F. Crommie, M.L. Cohen, S.G. Louie, and A. Zettl, *Graphene at the Edge: Stability and Dynamics.* Science, 2009, **323**, 1705.

13. Fister, T.T., D.D. Fong, J.A. Eastman, H. Iddir, P. Zapol, P.H. Fuoss, M. Balasubramanian, R.A. Gordon, K.R. Balasubramaniam, and P.A. Salvador, *Total-Reflection Inelastic X-Ray Scattering from a 10-nm Thick La0.6Sr0.4CoO3 Thin Film.* Physical Review Letters, 2011, **106**, 037401.
14. Hebboul, S. *X-raying the skin*. 2011; Available from: http://physics.aps.org/synopsis-for/10.1103/PhysRevLett.106.037401?referer=rss.
15. Boyen, H.G., A. Ethirajan, auml, G. stle, F. Weigl, P. Ziemann, G. Schmid, M.G. Garnier, uuml, M. ttner, and P. Oelhafen, *Alloy Formation of Supported Gold Nanoparticles at Their Transition from Clusters to Solids: Does Size Matter?* Physical Review Letters 2005, **94**, 016804.
16. Sun, C.Q., L.K. Pan, H.L. Bai, Z.Q. Li, P. Wu, and E.Y. Jiang, *Effects of surface passivation and interfacial reaction on the size-dependent 2p-level shift of supported copper nanosolids.* Acta Materialia, 2003, **51**, 4631.
17. Barbieri, R., A. de Siervo, M.F. Carazzolle, R. Landers, and G.G. Kleiman, *XPS and XAES study of Ag-Pd and Cu-Ni alloys: spectra, shifts and electronic structure information.* Journal of Electron Spectroscopy and Related Phenomena, 2004, **135**, 113.
18. Polyak, Y. and Z. Bastl, *XPS study of early stages of Al/Au interface formation.* Surface and Interface Analysis, 2009, **41**, 830.
19. Zhao, Z.J., F. Liu, L.M. Qiu, L.Z. Zhao, and S.K. Yan, *Core level binding energy shifts caused by size effect of nanoparticles.* Acta Physico-Chimica Sinica, 2008, **24**, 1685.
20. Spanjaard, D., C. Guillot, M.-C. Desjonquères, G. Tréglia, and J. Lecante, *Surface core level spectroscopy of transition metals: A new tool for the determination of their surface structure.* Surface Science Reports, 1985, **5**, 1.
21. Weststrate, C.J., E. Lundgren, J.N. Andersen, E.D.L. Rienks, A.C. Gluhoi, J.W. Bakker, I.M.N. Groot, and B.E. Nieuwenhuys, *CO adsorption on Au(310) and Au(321): 6-Fold coordinated gold atoms.* Surface Science, 2009, **603**, 2152.
22. Shikin, A.M., A. Varykhalov, G.V. Prudnikova, V.K. Adamchuk, W. Gudat, and O. Rader, *Photoemission from Stepped W(110): Initial or Final State Effect?* Physical Review Letters 2004, **93**, 146802.
23. Niimi, Y., H. Kambara, and H. Fukuyama, *Localized Distributions of Quasi-Two-Dimensional Electronic States near Defects Artificially Created at Graphite Surfaces in Magnetic Fields.* Physical Review Letters, 2009, **102**, 026803.
24. Hunt, M.R.C., *Surface and bulk components in angle-resolved core-level photoemission spectroscopy of graphite.* Physical Review B 2008, **78**, 153408.
25. Navas, E., K. Starke, C. Laubschat, E. Weschke, and G. Kaindl, *Surface core-level shift of 4f states for Tb(0001).* Physical Review B 1993, **48**, 14753.
26. Borgohain, K., J.B. Singh, M.V. Rama Rao, T. Shripathi, and S. Mahamuni, *Quantum size effects in CuO nanoparticles.* Physical Review B 2000, **61**, 11093.
27. Schmeißr, D., O. Böhme, A. Yfantis, T. Heller, D.R. Batchelor, I. Lundstrom, and A.L. Spetz, *Dipole Moment of Nanoparticles at Interfaces.* Physical Review Letters, 1999, **83**, 380.

28. Wertheim, G.K. and S.B. DiCenzo, *Cluster growth and core-electron binding energies in supported metal clusters.* Physical Review B, 1988, **37**, 844.
29. Wertheim, G.K., S.B. DiCenzo, and S.E. Youngquist, *Unit Charge on Supported Gold Clusters in Photoemission Final State.* Physical Review Letters, 1983, **51**, 2310.
30. Williams, A.R. and N.D. Lang, *Core-Level Binding-Energy Shifts in Metals.* Physical Review Letters, 1978, **40**, 954.
31. Kittel, C., *Introduction to Solid State Physics New York: John Wiley & Sons, 1996*
32. Wang, Y., L.L. Wang, and C.Q. Sun, *The $2p_{3/2}$ binding energy shift of Fe surface and Fe nanoparticles.* Chemical Physics Letters, 2009, **480**, 243.
33. Pauling, L., *Atomic Radii and Interatomic Distances in Metals.* Journal of the American Chemical Society, 1947, **69**, 542.
34. Goldschmidt, V.M., *Crystal structure and chemical correlation.* Berichte Der Deutschen Chemischen Gesellschaft, 1927, **60**, 1263.
35. Shpyrko, O.G., A.Y. Grigoriev, C. Steimer, P.S. Pershan, B. Lin, M. Meron, T. Graber, J. Gerbhardt, B. Ocko, and M. Deutsch, *Anomalous layering at the liquid Sn surface.* Physical Review B 2004, **70**, 224206.
36. Feibelman, P.J., *Relaxation of hcp(0001) surfaces: A chemical view.* Physical Review B 1996, **53**, 13740.
37. Richter, B., H. Kuhlenbeck, H.J. Freund, and P.S. Bagus, *Cluster core-level binding-energy shifts: The role of lattice strain.* Physical Review Letters, 2004, **93**, 026805.
38. Biswas, A., Z. Marton, J. Kanzow, J. Kruse, V. Zaporojtchenko, F. Faupel, and T. Strunskus, *Controlled Generation of Ni Nanoparticles in the Capping Layers of Teflon AF by Vapor-Phase Tandem Evaporation.* Nano Letters, 2002, **3**, 69.
39. Lamber, R., S. Wetjen, and N.I. Jaeger, *Size dependence of the lattice parameter of small palladium particles.* Physical Review B 1995, **51**, 10968.
40. Matsui, F., T. Matsushita, Y. Kato, M. Hashimoto, K. Inaji, F.Z. Guo, and H. Daimon, *Atomic-Layer Resolved Magnetic and Electronic Structure Analysis of Ni Thin Film on a Cu(001) Surface by Diffraction Spectroscopy.* Physical Review Letters, 2008, **100**, 207201.
41. Mironets, O., H.L. Meyerheim, C. Tusche, V.S. Stepanyuk, E. Soyka, P. Zschack, H. Hong, N. Jeutter, R. Felici, and J. Kirschner, *Direct evidence for mesoscopic relaxations in cobalt nanoislands on Cu(001).* Physical Review Letters, 2008, **100**, 096103.
42. Qi, W.H., B.Y. Huang, and M.P. Wang, *Structure of Unsupported Small Palladium Nanoparticles.* Nanoscale Research Letters, 2009, **4**, 269.
43. Zhang, K.Z., M.M.B. Holl, and F.R. McFeely, *Extra-atomic relaxation and core-level binding energy shifts at silicon/silicon oxide interfaces: Effects of cluster size on physical models.* Journal of Physical Chemistry B, 1998, **102**, 3930.
44. Comaschi, T., A. Balerna, and S. Mobilio, *Temperature dependence of the structural parameters of gold nanoparticles investigated with EXAFS.* Physical Review B 2008, **77**, 075432.

45. Nepijko, S.A., M. Klimenkov, M. Adelt, H. Kuhlenbeck, R. Schlögl, and H.J. Freund, *Structural Investigation of Palladium Clusters on γ-AlO3(111)/NiAl(110) with Transmission Electron Microscopy.* Langmuir, 1999, **15**, 5309.
46. Wang, Y., Y.G. Nie, L.L. Wang, and C.Q. Sun, *Atomic-Layer- and Crystal-Orientation-Resolved 3d(5/2) Binding Energy Shift of Ru(0001) and Ru(1010) Surfaces.* Journal of Physical Chemistry C, 2010, **114**, 1226.
47. Wang, Y., Y.G. Nie, J.S. Pan, L.K. Pan, Z. Sun, L.L. Wang, and C.Q. Sun, *Orientation-resolved 3d(5/2) binding energy shift of Rh and Pd surfaces: anisotropy of the skin-depth lattice strain and quantum trapping.* Physical Chemistry Chemical Physics 2010, **12**, 2177.
48. Wang, Y., Y.G. Nie, J.S. Pan, L. Pan, Z. Sun, and C.Q. Sun, *Layer and orientation resolved bond relaxation and quantum entrapment of charge and energy at Be surfaces.* Physical Chemistry Chemical Physics 2010, **12**, 12753.
49. Nie, Y., Y. Wang, Y. Sun, J.S. Pan, B.R. Mehta, M. Khanuja, S.M. Shivaprasad, and C.Q. Sun, *CuPd interface charge and energy quantum entrapment: A tight-binding and XPS investigation.* Applied Surface Science 2010, **257**, 727.
50. Nie, Y., J. Pan, Z. Zhang, J. Chai, S. Wang, C.S. Yang, D. Li, and C.Q. Sun, *Size dependent 2p3/2 binding-energy shift of Ni nanoclusters on SiO2 support: Skin-depth local strain and quantum trapping.* Applied Surface Science 2010, **256**, 4667.
51. Gu, M.X., Y.C. Zhou, L.K. Pan, Z. Sun, S.Z. Wang, and C.Q. Sun, *Temperature dependence of the elastic and vibronic behavior of Si, Ge, and diamond crystals.* Journal of Applied Physics, 2007, **102**,
52. Sun, C.Q., C.M. Li, H.L. Bai, and E.Y. Jiang, *Melting point oscillation of a solid over the whole range of sizes.* Nanotechnology, 2005, **16**, 1290.
53. Huang, W.J., R. Sun, J. Tao, L.D. Menard, R.G. Nuzzo, and J.M. Zuo, *Coordination-dependent surface atomic contraction in nanocrystals revealed by coherent diffraction.* Nature Materials, 2008, **7**, 308.
54. Chan, A.S.Y., G.K. Wertheim, H. Wang, M.D. Ulrich, J.E. Rowe, and T.E. Madey, *Surface atom core-level shifts of clean and oxygen-covered Re(1231).* Physical Review B 2005, **72**, 035442.
55. Jaskólka, S., T. Radon, E.V. Chulkov, and O.S. Koroleva, *Photofield emission spectroscopy of the (111) and (100) tantalum band structure and surface density of states.* Vacuum, **46**, 449.
56. Kim, B., J. Chen, J.L. Erskine, W.N. Mei, and C.M. Wei, *Surface and bulk photoelectron diffraction from W(110) 4f core levels.* Physical Review B 1993, **48**, 4735.
57. Sun, C.Q., *Size dependence of nanostructures: Impact of bond order deficiency.* Progress in Solid State Chemistry, 2007, **35**, 1.
58. Andersen, J.N., D. Hennig, E. Lundgren, M. Methfessel, R. Nyholm, and M. Scheffler, *Surface core-level shifts of some 4d-metal single-crystal surfaces: Experiments and ab initio calculations.* Physical Review B 1994, **50**, 17525.
59. Baraldi, A., L. Bianchettin, E. Vesselli, S. de Gironcoli, S. Lizzit, L. Petaccia, G. Zampieri, G. Comelli, and R. Rosei, *Highly under-coordinated atoms at Rh surfaces: interplay of*

*strain and coordination effects on core level shift.* New Journal of Physics, 2007, **9, 143**, 12.

60. Aldén, M., H.L. Skriver, and B. Johansson, *Ab initio surface core-level shifts and surface segregation energies.* Physical Review Letters 1993, **71**, 2449.
61. Bartynski, R.A., D. Heskett, K. Garrison, G. Watson, D.M. Zehner, W.N. Mei, S.Y. Tong, and X. Pan, *The first interlayer spacing of Ta(100) determined by photoelectron diffraction.* Journal of Vacuum Science & Technology A: Vacuum, Surfaces, and Films, 1989, **7**, 1931.
62. Fang, B.S., W.S. Lo, T.S. Chien, T.C. Leung, C.Y. Lue, C.T. Chan, and K.M. Ho, *Surface band structures on Nb(001).* Physical Review B, 1994, **50**, 11093.
63. Balamurugan, B. and T. Maruyama, *Inhomogeneous effect of particle size on core-level and valence-band electrons: Size-dependent electronic structure of Cu3N nanoparticles.* Applied Physics Letters, 2006, **89**, 033112.
64. Sun, C.Q., *Surface and nanosolid core-level shift: Impact of atomic coordination-number imperfection.* Physical Review B 2004, **69**, 045105.
65. Wertheim, G.K. and P.H. Citrin, *Surface-atom core-level shifts of W(111).* Physical Review B 1988, **38**, 7820.
66. Riffe, D.M., B. Kim, J.L. Erskine, and N.D. Shinn, *Surface core-level shifts and atomic coordination at a stepped W(110) surface.* Physical Review B 1994, **50**, 14481.
67. Purcell, K.G., J. Jupille, G.P. Derby, and D.A. King, *Identification of underlayer components in the surface core-level spectra of W(111).* Physical Review B 1987, **36**, 1288.
68. Zhou, X. and J.L. Erskine, *Surface core-level shifts at vicinal tungsten surfaces.* Physical Review B 2009, **79**, 155422.
69. Chauveau, D., P. Roubin, C. Guillot, J. Lecante, G. Tréglia, M.C. Desjonquères, and D. Spanjaard, *Surface core level spectroscopy of the stepped surface.* Solid State Communications 1984, **52**, 635.
70. Purcell, K.G., J. Jupille, and D.A. King, *Coordination number and surface core-level shift spectroscopy: Stepped tungsten surfaces.* Surface Science, 1989, **208**, 245.
71. Jupille, J., K.G. Purcell, and D.A. King, *W{100} clean surface phase transition studied by core-level-shift spectroscopy: Order-order or order-disorder transition.* Physical Review B 1989, **39**, 6871.
72. Sun, C.Q., Y. Wang, Y.G. Nie, B.R. Mehta, M. Khanuja, S.M. Shivaprasad, Y. Sun, J.S. Pan, L.K. Pan, and Z. Sun, *Interface quantum trap depression and charge polarization in the CuPd and AgPd bimetallic alloy catalysts.* Phys Chem Chem Phys, 2010, **12**, 3131
73. Sun, C.Q., *Thermo-mechanical behavior of low-dimensional systems: The local bond average approach.* Progress in Materials Science, 2009, **54**, 179.
74. Liu, X.J., J.W. Li, Z.F. Zhou, L.W. Yang, Z.S. Ma, G.F. Xie, Y. Pan, and C.Q. Sun, *Size-induced elastic stiffening of ZnO nanostructures: Skin-depth energy pinning.* Applied Physics Letters, 2009, **94**,

75. Sun, C.Q., Y. Shi, C.M. Li, S. Li, and T.C.A. Yeung, *Size-induced undercooling and overheating in phase transitions in bare and embedded clusters.* Physical Review B, 2006, **73**, 075408.
76. Glans, P.A., L.I. Johansson, T. Balasubramanian, and R.J. Blake, *Assignment of the surface core-level shifts to the surface layers of Be(10(1)over-bar0).* Physical Review B, 2004, **70**, 033408.
77. Johansson, L.I. and H.I.P. Johansson, *unusual behavior of surface shifted core levels on Be(0001) and Be(10-10).* Nuclear Instruments & Methods in Physics Research Section B, 1995, **97**, 430.
78. Johansson, L.I., H.I.P. Johansson, E. Lundgren, J.N. Andersen, and R. Nyholm, *surface core level shift of Be(11-20).* Surface Science, 1994, **321**, L219.
79. Johansson, L.I., H.I.P. Johansson, J.N. Andersen, E. Lundgren, and R. Nyholm, *3 surface shifted core levels on Be(0001).* Physical Review Letters, 1993, **71**, 2453.
80. Lizzit, S., K. Pohl, A. Baraldi, G. Comelli, V. Fritzsche, E.W. Plummer, R. Stumpf, and P. Hofmann, *Physics of the Be(10(1)over-bar0) surface core level spectrum.* Physical Review Letters, 1998, **81**, 3271.
81. Tang, S.J., H.T. Jeng, C.S. Hsue, Ismail, P.T. Sprunger, and E.W. Plummer, *Surface state influence on the surface lattice structure in Be(10(1)over-bar0).* Physical Review B, 2008, **77**, 6.
82. Johansson, L.I., *anomalous surface core level shifts on Be metal* Surface Review and Letters, 1995, **2**, 225.
83. Johansson, H.I.P., L.I. Johansson, E. Lundgren, J.N. Andersen, and R. Nyholm, *core level shifts on Be(10-10).* Physical Review B, 1994, **49**, 17460.
84. Hofmann, P., R. Stumpf, V.M. Silkin, E.V. Chulkov, and E.W. Plummer, *The electronic structure of Be(10(1)over-bar-0).* Surface Science, 1996, **355**, L278.
85. Johansson, L.I., P.A. Glans, and T. Balasubramanian, *Fourth-layer surface core-level shift on Be(0001).* Physical Review B, 1998, **58**, 3621.
86. Hjortstam, O., J. Trygg, J.M. Wills, B. Johansson, and O. Eriksson. *Giant surface layer relaxation for be (10(1)over-bar-0)*. in *2nd International Symposium on Metallic Multilayers (MML 95)*. 1995. Cambridge, England: Elsevier Science Bv.
87. Hjortstam, O., J. Trygg, J.M. Wills, B. Johansson, and O. Eriksson, *Surface layer relaxation for Be(10(1)over-bar0): Theory.* Surface Science, 1996, **355**, 214.
88. Speranza, G. and L. Minati, *The surface and bulk core line's in crystalline and disordered polycrystalline graphite.* Surface Science, 2006, **600**, 4438.
89. Lizzit, S., A. Baraldi, A. Groso, K. Reuter, M.V. Ganduglia-Pirovano, C. Stampl, M. Scheffler, M. Stichler, C. Keller, W. Wurth, and D. Menzel, *Surface core-level shifts of clean and oxygen-covered Ru(0001).* Physical Review B, 2001, **63**, 205419.
90. Baraldi, A., S. Lizzit, G. Comelli, and G. Paolucci, *Oxygen adsorption and ordering on Ru(10(1)over-bar-0).* Physical Review B, 2001, **63**, 115410.
91. Baraldi, A., S. Lizzit, and G. Paolucci, *Identification of atomic adsorption site by means of high-resolution photoemission surface core-level shift: oxygen on Ru(1010).* Surface Science, 2000, **457**, L354.

92. Baraldi, A., S. Lizzit, G. Comelli, A. Goldoni, P. Hofmann, and G. Paolucci, *Core-level subsurface shifted component in a 4d transition metal: Ru(10(1)over-bar-0).* Physical Review B, 2000, **61**, 4534.
93. Chen, M.S. and D.W. Goodman, *The structure of catalytically active gold on titania.* Science, 2004, **306**, 252.
94. Dahl, S., A. Logadottir, R.C. Egeberg, J.H. Larsen, I. Chorkendorff, E. Tornqvist, and J.K. Norskov, *Role of steps in N-2 activation on Ru(0001).* Physical Review Letters, 1999, **83**, 1814.
95. Hammer, B., *Bond Activation at Monatomic Steps: NO Dissociation at Corrugated Ru(0001).* Physical Review Letters, 1999, **83**, 3681.
96. Zambelli, T., J. Wintterlin, J. Trost, and G. Ertl, *Identification of the "Active Sites" of a Surface-Catalyzed Reaction.* Science, 1996, **273**, 1688.
97. Kratzer, P., E. Pehlke, M. Scheffler, M.B. Raschke, and U. Hofer, *Highly site-specific H-2 adsorption on vicinal Si(001) surfaces.* Physical Review Letters, 1998, **81**, 5596.
98. Tong, W.P., N.R. Tao, Z.B. Wang, J. Lu, and K. Lu, *Nitriding iron at lower temperatures.* Science, 2003, **299**, 686.
99. Fratesi, G. and S. de Gironcoli, *Analysis of methane-to-methanol conversion on clean and defective Rh surfaces.* Journal of Chemical Physics, 2006, **125**, 044701.
100. Kokalj, A., N. Bonini, C. Sbraccia, S. de Gironcoli, and S. Baroni, *Engineering the reactivity of metal catalysts: A model study of methane dehydrogenation on Rh(111).* Journal of the American Chemical Society, 2004, **126**, 16732.
101. Abbet, S., A. Sanchez, U. Heiz, W.D. Schneider, A.M. Ferrari, G. Pacchioni, and N. Rosch, *Acetylene cyclotrimerization on supported size-selected $Pd_n$ clusters (1 <= n <= 30): one atom is enough!* Journal of the American Chemical Society, 2000, **122**, 3453.
102. Abbet, S., U. Heiz, H. Hakkinen, and U. Landman, *CO oxidation on a single Pd atom supported on magnesia.* Physical Review Letters, 2001, **86**, 5950.
103. Zhang, C.J. and P. Hu, *The possibility of single C--H bond activation in CH[sub 4] on a MoO[sub 3]-supported Pt catalyst: A density functional theory study.* Journal of chemical physics, 2002, **116**, 4281.
104. Jakob, P., M. Gsell, and D. Menzel, *Interactions of adsorbates with locally strained substrate lattices.* The Journal of chemical physics, 2001, **114**, 10075.
105. Gsell, M., P. Jakob, and D. Menzel, *Effect of Substrate Strain on Adsorption.* Science, 1998, **280**, 717.
106. Wintterlin, J., T. Zambelli, J. Trost, J. Greeley, and M. Mavrikakis, *Atomic-Scale Evidence for an Enhanced Catalytic Reactivity of Stretched Surfaces13.* Angewandte Chemie International Edition, 2003, **42**, 2850.
107. Roduner, E., *Size matters: why nanomaterials are different.* Chemical Society Reviews 2006, **35**, 583.
108. Bianchettin, L., A. Baraldi, S. de Gironcoli, E. Vesselli, S. Lizzit, L. Petaccia, G. Comelli, and R. Rosei, *Core level shifts of undercoordinated Pt atoms.* Journal of Chemical Physics, 2008, **128** 114706.

109. Mårtensson, N., H.B. Saalfeld, H. Kuhlenbeck, and M. Neumann, *structural dependence of the 5D-metal surface energies as deduced from surface core level shift measurements.* Physical Review B 1989, **39**, 8181.
110. Ducros, R. and J. Fusy, *Core level binding energy shifts of rhenium surface atoms for a clean and oxygenated surface.* Journal of Electron Spectroscopy and Related Phenomena 1987, **42**, 305.
111. Chan, A.S.Y., W. Chen, H. Wang, J.E. Rowe, and T.E. Madey, *Methanol Reactions over Oxygen-Modified Re Surfaces: Influence of Surface Structure and Oxidation.* Journal of Physical Chemistry B, 2004, **108**, 14643.
112. Wang, H., A.S.Y. Chan, W. Chen, P. Kaghazchi, T. Jacob, and T.E. Madey, *Facet Stability in Oxygen-Induced Nanofaceting of Re(12$\bar{3}$1).* Acs Nano, 2007, **1**, 449.
113. Sun, C.Q., *Oxidation electronics: bond-band-barrier correlation and its applications.* Progress in Materials Science, 2003, **48**, 521.
114. Sun, C.Q., Y. Wang, Y.G. Nie, Y. Sun, J.S. Pan, L.K. Pan, and Z. Sun, *Adatoms-Induced Local Bond Contraction, Quantum Trap Depression, and Charge Polarization at Pt and Rh Surfaces.* Journal of Physical Chemistry C, 2009, **113**, 21889.
115. Cox, A.J., J.G. Louderback, S.E. Apsel, and L.A. Bloomfield, *Magnetic in 4d-transition metal-clusters.* Physical Review B, 1994, **49**, 12295.
116. Khanuja, M., B.R. Mehta, and S.M. Shivaprasad, *Geometric and electronic changes during interface alloy formation in Cu/Pd bimetal layers.* Thin Solid Films, 516, 2008, 5435.
117. Niimi, Y., H. Kambara, and H. Fukuyama, *Localized Distributions of Quasi-Two-Dimensional Electronic States near Defects Artificially Created at Graphite Surfaces in Magnetic Fields.* Physical Review Letters, 2009, **102**, 026803.
118. Enoki, T., Y. Kobayashi, and K.I. Fukui, *Electronic structures of graphene edges and nanographene.* International Reviews in Physical Chemistry, 2007, **26**, 609.
119. Ugeda, M.M., I. Brihuega, F. Guinea, and J.M. Gómez-Rodríguez, *Missing Atom as a Source of Carbon Magnetism.* Physical Review Letters 2010, **104**, 096804.
120. Matsui, T., H. Kambara, Y. Niimi, K. Tagami, M. Tsukada, and H. Fukuyama, *STS Observations of Landau Levels at Graphite Surfaces.* Physical Review Letters, 2005, **94**, 226403.
121. Li, G. and E.Y. Andrei, *Observation of Landau levels of Dirac fermions in graphite.* Nature Physics, 2007, **3**, 623.
122. Kondo, T., Y. Honma, J. Oh, T. Machida, and J. Nakamura, *Edge states propagating from a defect of graphite: Scanning tunneling spectroscopy measurements.* Physical Review B, 2010, **82**, 153414.
123. Michon, A., S. Vezian, A. Ouerghi, M. Zielinski, T. Chassagne, and M. Portail, *Direct growth of few-layer graphene on 6H-SiC and 3C-SiC/Si via propane chemical vapor deposition.* Applied Physics Letters 2010, **97**, 171909.
124. Cheng, Y.C. and U. Schwingenschlogl, *A route to strong p-doping of epitaxial graphene on SiC.* Applied Physics Letters 2010, **97**, 193304.

125. Novoselov, K.S., A.K. Geim, S.V. Morozov, D. Jiang, M.I. Katsnelson, I.V. Grigorieva, S.V. Dubonos, and A.A. Firsov, *Two-dimensional gas of massless Dirac fermions in graphene.* Nature, 2005, **438**, 197.
126. Vozmediano, M.A.H., M.P. Lopez-Sancho, T. Stauber, and F. Guinea, *Local defects and ferromagnetism in graphene layers.* Physical Review B, 2005, **72**, 155121.
127. Nomura, K. and A.H. MacDonald, *Quantum transport of massless dirac fermions.* Physical Review Letters, 2007, **98**, 076602.
128. Omar, M.A., *Elementary Solid State Physics: Principles and Applications*1993, New York: Addison-Wesley.
129. Kohiki, S., *Photoemission from small Pd clusters on Al2O3 and SiO2 substrates.* Applied Surface Science, **25**, 81.
130. van Buuren, T., L.N. Dinh, L.L. Chase, W.J. Siekhaus, and L.J. Terminello, *Changes in the Electronic Properties of Si Nanocrystals as a Function of Particle Size.* Physical Review Letters, 1998, **80**, 3803.
131. Goldstein, A.N., C.M. Echer, and A.P. Alivisatos, *MELTING IN SEMICONDUCTOR NANOCRYSTALS.* Science, 1992, **256**, 1425.
132. Christenson, H.K., *Confinement effects on freezing and melting.* Journal of Physics-Condensed Matter, 2001, **13**, R95.
133. Yavuz, C.T., J.T. Mayo, W.W. Yu, A. Prakash, J.C. Falkner, S. Yean, L.L. Cong, H.J. Shipley, A. Kan, M. Tomson, D. Natelson, and V.L. Colvin, *Low-field magnetic separation of monodisperse Fe3O4 nanocrystals.* Science, 2006, **314**, 964.
134. Gruene, P., D.M. Rayner, B. Redlich, A.F.G. van der Meer, J.T. Lyon, G. Meijer, and A. Fielicke, *Structures of neutral Au-7, Au-19, and Au-20 clusters in the gas phase.* Science, 2008, **321**, 674.
135. Nosova, L.V., M.V. Stenin, Y.N. Nogin, and Y.A. Ryndin, *EXAFS and XPS studies of the influence of metal particle size, nature of support and H2 and CO adsorption on the structure and electronic properties of palladium.* Applied Surface Science, 1992, **55**, 43.
136. Vajda, S., M.J. Pellin, J.P. Greeley, C.L. Marshall, L.A. Curtiss, G.A. Ballentine, J.W. Elam, S. Catillon-Mucherie, P.C. Redfern, F. Mehmood, and P. Zapol, *Subnanometre platinum clusters as highly active and selective catalysts for the oxidative dehydrogenation of propane.* Nature Materials, 2009, **8**, 213.
137. Bonnemann, H., G. Khelashvili, S. Behrens, A. Hinsch, K. Skupien, and E. Dinjus, *Role of the platinum nanoclusters in the iodide/triiodide redox system of dye solar cells.* Journal of Cluster Science, 2007, **18**, 141.
138. Kodambaka, S., J. Tersoff, M.C. Reuter, and F.M. Ross, *Germanium nanowire growth below the eutectic temperature.* Science, 2007, **316**, 729.
139. C. Das, B. and A.J. Pal, *To change transport gap of semiconducting nanoparticles without disturbing the optical one: Core-shell approach.* Applied Physics Letters, 2009, **94**, 082106.
140. Park, C.-H., F. Giustino, C.D. Spataru, M.L. Cohen, and S.G. Louie, *First-Principles Study of Electron Linewidths in Graphene.* Physical Review Letters, 2009, **102**, 076803.

141. Streitz, F.H., R.C. Cammarata, and K. Sieradzki, *surface stress effects on elastic properties .1. thin metal films* Physical Review B, 1994, **49**, 10699.
142. Streitz, F.H., R.C. Cammarata, and K. Sieradzki, *surface stress effect on elastic properties.2. metallic multilayers.* Physical Review B, 1994, **49**, 10707.
143. Cammarata, R.C. and K. Sieradzki, *Effects of surface stress on the elastic moduli of thin films and superlattices.* Physical Review Letters, 1989, **62**, 2005.
144. Muller, P. and A. Saul, *Elastic effects on surface physics.* Surface Science Reports, 2004, **54**, 157.
145. Dingreville, R., J.M. Qu, and M. Cherkaoui, *Surface free energy and its effect on the elastic behavior of nano-sized particles, wires and films.* Journal of the Mechanics and Physics of Solids, 2005, **53**, 1827.
146. Sander, D., *Surface stress: implications and measurements.* Current Opinion in Solid State & Materials Science, 2003, **7**, 51.
147. Weinert, M., J.W. Davenport, and R.E. Watson, *Final-state screening of core holes in metals.* Physical Review B, 1986, **34**, 2971.
148. Pabisiak, T. and A. Kiejna, *First-principles study of Au nanostructures on rutile TiO2 ( 110 ).* Physical Review B, 2009, **79**, 085411.
149. Vijayakrishnan, V., A. Chainani, D.D. Sarma, and C.N.R. Rao, *metal insulator transitions in metal clusters- a high energy spectroscopy study of Pd and Ag clusters.* Journal of Physical Chemistry, 1992, **96**, 8679.
150. Tao, J.G., J.S. Pan, C.H.A. Huan, Z. Zhang, J.W. Chai, and S.J. Wang, *Origin of XPS binding energy shifts in Ni clusters and atoms on rutile TiO2 surfaces.* Surface Science, 2008, **602**, 2769.
151. Negreiros, F.R., E.A. Soares, A. de Siervo, R. Paniago, V.E. de Carvalho, and R. Landers, *Theoretical study of the heteroepitaxial growth of Pd on Cu(111), Pd on Ni(111), Ni on Pd(111), and Cu on Pd(111) using a semiempirical method.* Physical Review B 2010, **81**,
152. Karim, A., A.N. Al-Rawi, A. Kara, T.S. Rahman, O. Trushin, and T. Ala-Nissila, *Diffusion of small two-dimensional Cu islands on Cu(111) studied with a kinetic Monte Carlo method.* Physical Review B 2006, **73**, 165411.
153. Foiles, S.M., M.I. Baskes, and M.S. Daw, *Embedded-atom-method functions for the fcc metals Cu, Ag, Au, Ni, Pd, Pt, and their alloys.* Physical Review B 1986, **33**, 7983.
154. Wu, Y.T., E. Garfunkel, and T.E. Madey, *Initial stages of Cu growth on ordered Al2O3 ultrathin films.* Journal of Vacuum Science & Technology a-Vacuum Surfaces and Films, 1996, **14**, 1662.
155. Bork, J., J. Onsgaard, and L. Diekhoner, *Growth and structure of Ag on bilayer Co nanoislands on Cu(111).* Journal of Physics-Condensed Matter, 2010, **22**,
156. Rout, S.K., S. Panigrahi, and J. Bera, *Study on electrical properties of Ni-doped SrTiO3 ceramics using impedance spectroscopy.* Bulletin of Materials Science, 2005, **28**, 275.
157. Zhou, G.W., *Metal-oxide interfaces at the nanoscale.* Applied Physics Letters, 2009, **94**,
158. Seah, M.P. and S.J. Spencer, *Ultrathin SiO2 on Si IV. Intensity measurement in XPS and deduced thickness linearity.* Surface and Interface Analysis, 2003, **35**, 515.

159. Lu, Z.H., J.P. McCaffrey, B. Brar, G.D. Wilk, R.M. Wallace, L.C. Feldman, and S.P. Tay, *SiO2 film thickness metrology by x-ray photoelectron spectroscopy.* Applied Physics Letters 1997, **71**, 2764.
160. Rao, F.Y., M.Y. Kim, A.J. Freeman, S.P. Tang, and M. Anthony, *Structural and electronic properties of transition-metal/BaTiO3(001) interfaces.* Physical Review B, 1997, **55**, 13953.
161. Rao, C.N.R., G.U. Kulkarni, P.J. Thomas, and P.P. Edwards, *Size-dependent chemistry: Properties of nanocrystals.* Chemistry-a European Journal, 2002, **8**, 29.
162. Yang, D.Q. and E. Sacher, *Initial- and final-state effects on metal cluster/substrate interactions, as determined by XPS: copper clusters on Dow Cyclotene and highly oriented pyrolytic graphite.* Applied Surface Science, 2002, **195**, 187.
163. Onishi, H., T. Aruga, C. Egawa, and Y. Iwasawa, *photoelectron spectroscopic study of clean and coadsorbed Ni/TiO2(110) interface.* Surface Science, 1990, **233**, 261.
164. Godehusen, K., T. Richter, P. Zimmermann, and M. Martins, *2p Photoionization of Atomic Ni: A Comparison with Ni Metal and NiO Photoionization.* Physical Review Letters, 2002, **88**, 217601.
165. Sun, Y., J.S. Pan, J.G. Tao, Y.G. Nie, C.H.A. Huan, Z. Zhang, J.W. Chai, D. Li, S.J. Wang, and C.Q. Sun, *Size Dependence of the 2p(3/2) and 3d(5/2) Binding Energy Shift of Ni Nanostructures: Skin-Depth Charge and Energy Trapping.* Journal of Physical Chemistry C, 2009, **113**, 10939.
166. Howard, A., D.N.S. Clark, C.E.J. Mitchell, R.G. Egdell, and V.R. Dhanak, *Initial and final state effects in photoemission from Au nanoclusters on TiO2(110).* Surface Science, 2002, **518**, 210.
167. Kim, S., M.C. Kim, S.-H. Choi, K.J. Kim, H.N. Hwang, and C.C. Hwang, *Size dependence of Si 2p core-level shift at Si nanocrystal/SiO[sub 2] interfaces.* Applied Physics Letters, 2007, **91**, 103113.
168. Balamurugan, B. and T. Maruyama, *Evidence of an enhanced interband absorption in Au nanoparticles: Size-dependent electronic structure and optical properties.* Applied Physics Letters, 2005, **87**, 143105.
169. Bagus, P.S., A. Wieckowski, and H. Freund, *Initial and final state contributions to binding-energy shifts due to lattice strain: Validation of Auger parameter analyses.* Chemical Physics Letters, 2006, **420**, 42.
170. Kawasaki, M., K. Takahashi, T. Maeda, R. Tsuchiya, M. Shinohara, O. Ishiyama, T. Yonezawa, M. Yoshimoto, and H. Koinuma, *atomic control of the SrTiO3 crystal surface.* Science, 1994, **266**, 1540.
171. Polli, A.D., T. Wagner, and M. Ruhle, *Effect of Ca impurities and wet chemical etching on the surface morphology of SrTiO3 substrates.* Surface Science, 1999, **429**, 237.
172. Fu, Q. and T. Wagner, *Thermal stability of Cr clusters on SrTiO3(100).* Surface Science, 2002, **505**, 39.
173. Koster, G., B.L. Kropman, G. Rijnders, D.H.A. Blank, and H. Rogalla, *Quasi-ideal strontium titanate crystal surfaces through formation of strontium hydroxide.* Applied Physics Letters 1998, **73**, 2920.

174. Polli, A.D., T. Wagner, T. Gemming, and M. Ruhle, *Growth of platinum on TiO2- and SrO-terminated SrTiO3(100).* Surface Science, 2000, **448**, 279.
175. Seah, M.P. and W.A. Dench, *Quantitative electron spectroscopy of surfaces: A standard data base for electron inelastic mean free paths in solids.* Surface and Interface Analysis, 1979, **1**, 2.
176. Asakawa, T., K. Tanaka, and I. Toyoshima, *Interaction of nickel with silicon oxide or silica formed on silicon(111) and carbon monoxide adsorption inhibition in nickel/silicon oxide/n-silicon(111) studied by XPS and AES.* Langmuir, 1988, **4**, 521.
177. Marcus, P. and C. Hinnen, *XPS study of the early stages of deposition of Ni, Cu and Pt on HOPG.* Surface Science, 1997, **392**, 134.
178. Sun, C.Q., L.K. Pan, T.P. Chen, X.W. Sun, S. Li, and C.M. Li, *Distinguishing the effect of crystal-field screening from the effect of valence recharging on the 2P(3/2) and 3d(5/2) level energies of nanostructured copper.* Applied Surface Science 2006, **252**, 2101.
179. van Benthem, K., C. Scheu, W. Sigle, and M. Ruhle, *Electronic structure investigations of Ni and Cr films on (100)SrTiO3 substrates using electron energy-loss spectroscopy.* Zeitschrift Fur Metallkunde, 2002, **93**, 362.
180. Wagner, T., A.D. Polli, G. Richter, and H. Stanzick, *Epitaxial growth of metals on (100) SrTiO3: The influence of lattice mismatch and reactivity.* Zeitschrift Fur Metallkunde, 2001, **92**, 701.
181. Vlachos, D., M. Kamaratos, S.D. Foulias, C. Argirusis, and G. Borchardt, *Adsorption of oxygen on a nickel covered SrTiO3(100) surface studied by means of Auger electron spectroscopy and work function measurements.* Journal of Physics-Condensed Matter, 2005, **17**, 635.
182. Vlachos, D., M. Kamaratos, S.D. Foulias, C. Argirusis, and G. Borchardt, *Ni ultrathin film development on SrTiO3(100) surface.* Surface Science, 2004, **550**, 213.
183. Wagner, C.D., *Auger lines in x-ray photoelectron spectrometry.* Analytical Chemistry, 1972, **44**, 967.
184. Wagner, C.D., *Chemical shifts of Auger lines, and the Auger parameter.* Faraday Discussions of the Chemical Society 1975, **60**, 291.
185. Wagner, C.D. and J.A. Taylor, *Contributions to screening in the solid state by electron systems of remote atoms: Effects to photoelectron and Auger transitions.* Journal of Electron Spectroscopy and Related Phenomena, 1982, **28**, 211.
186. Carlson, T.A., Faraday Discussions of the Chemical Society, 1975, **60**, 311.
187. Lang, N.D. and A.R. Williams, *theory of Auger relaxation energies in metals.* Physical Review B, 1979, **20**, 1369.
188. Hohlneicher, G., H. Pulm, and H.-J. Freund, *On the separation of initial and final state effects in photoelectron spectroscopy using an extension of the auger-parameter concept.* Journal of Electron Spectroscopy and Related Phenomena, 1985, **37**, 209.
189. Yang, D.Q. and E. Sacher, *Strongly enhanced interaction between evaporated Pt nanoparticles and functionalized multiwalled carbon nanotubes via plasma surface modifications: Effects of physical and chemical defects.* Journal of Physical Chemistry C, 2008, **112**, 4075.

190. Yang, D.Q. and E. Sacher, *Platinum nanoparticle interaction with chemically modified highly oriented pyrolytic graphite surfaces.* Chemistry of Materials 2006, **18**, 1811.
191. Bittencourt, C., M. Hecq, A. Felten, J.J. Pireaux, J. Ghijsen, M.P. Felicissimo, P. Rudolf, W. Drube, X. Ke, and G. Van Tendeloo, *Platinum-carbon nanotube interaction.* Chemical Physics Letters 2008, **462**, 260.
192. Sun, Y., Y. Wang, J.S. Pan, L.L. Wang, and C.Q. Sun, *Elucidating the 4f Binding Energy of an Isolated Pt Atom and Its Bulk Shift from the Measured Surface- and Size-Induced Pt 4f Core Level Shift.* Journal of Physical Chemistry C, 2009, **113**, 14696.
193. Tanuma, S., C.J. Powell, and D.R. Penn, *Calculations of electron inelastic mean free paths. VIII. Data for 15 elemental solids over the 50-2000 eV range.* Surface and Interface Analysis, 2005, **37**, 1.
194. Asthagiri, A., C. Niederberger, A.J. Francis, L.M. Porter, P.A. Salvador, and D.S. Sholl, *Thin Pt films on the polar SrTiO3(111) surface: an experimental and theoretical study.* Surface Science, 2003, **537**, 134.
195. Conard, T., A.C. Rousseau, L.M. Yu, J. Ghijsen, R. Sporken, R. Caudano, and R.L. Johnson, *Electron spectroscopy study of the Cu/SrTiO3(100) interface.* Surface Science, 1996, **359**, 82.
196. Francis, A.J., Y. Cao, and P.A. Salvador, *Epitaxial growth of Cu(100) and Pt(100) thin films on perovskite substrates.* Thin Solid Films 2006, **496**, 317.
197. Wagner, T., G. Richter, and M. Ruhle, *Epitaxy of Pd thin films on (100) SrTiO3: A three-step growth process.* Journal of Applied Physics 2001, **89**, 2606.
198. Jiang, Q. and H.M. Lu, *Size dependent interface energy and its applications.* Surface Science Reports, 2008, **63**, 427.
199. Veprek, S. and A.S. Argon, *Towards the understanding of mechanical properties of super- and ultrahard nanocomposites.* Journal of Vacuum Science & Technology B, 2002, **20**, 650.
200. Ci, L., J. Suhr, V. Pushparaj, X. Zhang, and P.M. Ajayan, *Continuous carbon nanotube reinforced composites.* Nano Letters, 2008, **8**, 2762.
201. Ouyang, G., X. Tan, C.X. Wang, and G.W. Yang, *Physical and chemical origin of size-dependent spontaneous interfacial alloying of core-shell nanostructures.* Chemical Physics Letters, 2006, **420**, 65.
202. Chen, J.G., C.A. Menning, and M.B. Zellner, *Monolayer bimetallic surfaces: Experimental and theoretical studies of trends in electronic and chemical properties.* Surface Science Reports, 2008, **63**, 201.
203. Rodriguez, J.A. and D.W. Goodman, *The nature of the metal metal bond in bimetallic surfaces.* Science, 1992, **257**, 897.
204. Kamakoti, P., B.D. Morreale, M.V. Ciocco, B.H. Howard, R.P. Killmeyer, A.V. Cugini, and D.S. Sholl, *Prediction of hydrogen flux through sulfur-tolerant binary alloy membranes.* Science, 2005, **307**, 569.
205. Buschbeck, J., I. Opahle, M. Richter, U.K. Rößler, P. Klaer, M. Kallmayer, H.J. Elmers, G. Jakob, L. Schultz, and S. Fähler, *Full Tunability of Strain along the fcc-bcc Bain Path in Epitaxial Films and Consequences for Magnetic Properties.* Physical Review Letters, 2009, **103**, 216101.

206. Liu, G., T.P. St Clair, and D.W. Goodman, *An XPS study of the interaction of ultrathin Cu films with Pd(111).* Journal of Physical Chemistry B, 1999, **103**, 8578.
207. Zhang, D.H. and W. Shi, *Dark current and infrared absorption of p-doped InGaAs/AlGaAs strained quantum wells.* Applied Physics Letters, 1998, **73**, 1095.
208. Dang, Y.X., W.J. Fan, S.T. Ng, S.F. Yoon, and D.H. Zhang, *Study of interdiffusion in GaInNAs/GaAs quantum well structure emitting at 1.3 mu m by eight-band k center dot p method.* Journal of Applied Physics, 2005, **97**, 103718
209. de Siervo, A., E.A. Soares, R. Landers, and G.G. Kleiman, *Photoelectron diffraction studies of Cu on Pd(111) random surface alloys.* Physical Review B, 2005, **71**, 115417.
210. de Siervo, A., R. Paniago, E.A. Soares, H.D. Pfannes, R. Landers, and G.G. Kleiman, *Growth study of Cu/Pd(111) by RHEED and XPS.* Surface Science, 2005, **575**, 217.
211. Reilly, J.P., C.J. Barnes, N.J. Price, R.A. Bennett, S. Poulston, P. Stone, and M. Bowker, *The growth mechanism, thermal stability, and reactivity of palladium mono- and multilayers on Cu(110).* Journal of Physical Chemistry B, 1999, **103**, 6521.
212. Grant, M.L., B.S. Swartzentruber, N.C. Bartelt, and J.B. Hannon, *Diffusion kinetics in the Pd/Cu(001) surface alloy.* Physical Review Letters, 2001, **86**, 4588.
213. Eremeev, S.V., G.G. Rusina, and E.V. Chulkov, *Diffusion properties of Cu(001)-c(2x2)-Pd surface alloys.* Surface Science, 2007, **601**, 3640.
214. Ganduglia-Pirovano, M.V., J. Kudrnovsk, and M. Scheffler, *Adlayer Core-Level Shifts of Random Metal Overlayers on Transition-Metal Substrates.* Physical Review Letters, 1997, **78**, 1807.
215. Popovic, Z.S. and S. Satpathy, *Wedge-shaped potential and Airy-function electron localization in oxide superlattices.* Physical Review Letters, 2005, **94**,